DEVELOPMENT OF SINGLE MOLECULE-SENSITIVE, IMAGING PROBES TARGETING NATIVE RNA

A Thesis
Presented to
The Academic Faculty

by

Aaron William Lifland

In Partial Fulfillment
of the Requirements for the Degree
Doctor of Philosophy in the
Department of Biomedical Engineering

Georgia Institute of Technology
August, 2012

DEVELOPMENT OF SINGLE MOLECULE-SENSITIVE, IMAGING PROBES TARGETING NATIVE RNA

Approved by:

Dr. Philip J. Santangelo, Advisor
Department of Biomedical Engineering
Georgia Institute of Technology

Dr. Gary J. Bassell
Department of Cell Biology
Emory University

Dr. Ravi Bellamkonda
Department of Biomedical Engineering
Georgia Institute of Technology

Dr. James E. Crowe, Jr.
Department of Microbiology and Immunology
Vanderbilt University

Dr. Joseph M. Le Doux
Department of Biomedical Engineering
Georgia Institute of Technology

Date Approved: May 22, 2012

ACKNOWLEDGEMENTS

I would like to thank my parents, Mark and Andrea, my sister, Melissa, and my wife Joyce for their guidance and unconditional support. Without them this work would not be possible. I am grateful to have many teachers and advisors who have encouraged my love of science and engineering along the way, especially Paul Bruns, Melissa Micou, Ruben Savizky, Vladimir Brezina, and Cahir McDevitt. I'd like to thank my advisor, Philip Santangelo for giving me the opportunity to perform this research, for his many ideas along the way, for his encouragement, and his support. Finally, I'd like to thank the members of the Santangelo lab, Chiara, Eric, Jeenah, and Jonathan and past members, Joana and Paul for their friendship, advice and support.

TABLE OF CONTENTS

LIST OF TABLES

LIST OF FIGURES

SUMMARY

The localization, trafficking and regulation of messenger ribonucleic acids (RNA) and viral RNA play crucial roles in cellular homeostasis and disease pathogenesis. In recent years biochemical and molecular biology methods used to study RNA function have made several important advances in the areas of RNA interference, expression of transgenes, and the sequencing of transcriptomes. In contrast, current technologies for imaging RNA in live cells remain in limited use.

Previous studies of RNA localization and dynamics have relied primarily on the expression of a reporter RNA and a fluorescent protein fusion that binds to aptamer sequences in the expressed RNA. While these plasmid based systems offer methodological flexibility, there remains a need to develop methods to image native, non-engineered RNA as plasmid derived RNAs may not have the same regulatory elements (3'UTR and introns) or copy number as the native RNA. Additionally, viral pathogenesis is often sensitive to the size and sequence of their genomic RNA and may not be suitable for study using engineered systems.

The goal of this research is to develop and validate a new method for imaging native, non-engineered RNA with single molecule-sensitivity. These probes will have four important properties. They will be modular, will be compatible with fixation and immunostaining, will bind quickly and specifically to targets, and will not interfere with RNA function. We propose to build upon the technique of delivering exogenous, linear probes that bind to their target by Watson-Crick base pairing. The probes will be multiply labeled and tetramerized to increase their brightness. To validate the probes, targeting and

utility will be demonstrated in two model systems: β-actin mRNA to show targeting of an endogenous target and the genomic RNA of human respiratory syncytial virus to show targeting of a viral RNA target.

CHAPTER 1

INTRODUCTION

Introduction

Experimental methods capable of imaging RNA in living cells have been in existence for a little over a decade. Yet, compared with the live imaging of proteins in cells, live cell RNA tracking has been utilized by far fewer researchers and has had less of an impact in the literature. This may be due to several factors, however, we believe that one of the main obstacles to the wide spread use of live cell RNA imaging is the wide variety of methods used. This is in contrast to the nearly ubiquitous use of fluorescent protein fusions used to label proteins. In this chapter the current methods for labeling RNA in living cell will be reviewed including plasmid based techniques and those based upon exogenous oligonucleotide probes. Details on the practical considerations involved in using probe based methods such as delivery, structure, chemistry and sensitivity will be discussed along with recommendations for researchers new to the field and suggestions for the refinement of probe based techniques.

RNA imaging background

The intricate system of control of ribonucleic acids in mammalian cells is a central component of homeostasis (Moore 2005). Messenger ribonucleic acids (mRNA) are dynamic molecules and the ability to follow their dynamics is crucial to understanding the biology of the cell. Throughout their lives, RNAs are edited, transported into physically distinct cellular compartments, differentially localized within

compartments, and interact with a slew of trans-acting cellular proteins and miRNAs (Moore 2005). Recent studies, which quantified levels of mRNA and protein in yeast, have shown the importance of these posttranscriptional controls in the control of the steady state level of protein in a cell (Gandhi, Zenklusen et al. 2011). In developmental biology, mRNA localization has been demonstrated in the symmetry breaking in early cell divisions. In particular the asymmetric localization of four maternal mRNAs, gurken, bicoid, oskar, and nanos, in the Drosophila melanogaster oocyte has been found to be essential for development and the generation of embryonic body axes (Gaspar 2011). The asymmetric localization of these mRNAs has been found to occur primarily on microtubules and is the result of differential transport to the oocyte anterior or posterior poles. Recently, the spatial regulation of mRNA by processing bodies (p-bodies) stress granules (SG) and RNA exosome, has garnered incresead attention (Buchan and Parker 2009). RNA p-bodies contain proteins involved in mRNA repression and degradation including; the mRNA decapping machinery, as well as key effectors of microRNA (miRNA)-mediated RNA interference (RNAi), such as Argonaute-2 (Ago2), miRNAs, and their cognate mRNAs (Kedersha, Stoecklin et al. 2005; Anderson and Kedersha 2006; Kedersha and Anderson 2007; Anderson and Kedersha 2008; Kedersha, Tisdale et al. 2008; Anderson and Kedersha 2009; Anderson and Kedersha 2009). The RNA exosome is a multisubunit 3′–5′ exoribonuclease complex that participates in degradation and processing of cellular RNA (Tomecki, Drazkowska et al. 2010; Tomecki and Dziembowski 2010) and has been shown to localize near the nucleus during stress (Lin, Duffy et al. 2007). SGs are one of the most studied RNA granules and are thought to be sites of triage, where RNA and RNPs are shuttled to be translationally repressed or before

degredation. SGs contain components of a noncanonical, translationally silent 48S preinitiation complex that includes the small ribosomal subunit, and early initiation factors eIF4E, eIF3, eIF4A, eIFG, and PABP. SGs also contain mRNAs and a set of mRNA binding proteins that regulate mRNA translation and decay, as well as proteins that regulate various aspects of mRNA metabolism. During viral pathogenesis of RNA viruses, viral genomic RNA and mRNA must be released into the cell, localize to sites of translation, and assemble at the site of viral budding.

While in vitro methods, such as quantitative reverse transcription polymerase chain reaction (qRT-PCR) and gene chips, have proven to be a reliable way to determine the copy number of RNA in the cell both for a single gene of interest using qRT-PCR and for most of the transcriptome using gene chips, these methods do not provide any data as to the spatial location of the RNA, the proteins associated with the RNA, or for the temporal changes in the level of RNA in a single cell over time (Schwanhausser, Busse et al. 2011). Molecular imaging holds the promise of elucidating several elements of RNA biology. Fluorescence *in situ* hybridization (FISH) has long been a standard technique for imaging RNA in fixed samples and has been extended into a quantitative technique using modern microcopy equipment (Sundell and Singer 1991). FISH, however, requires the use of fixed samples and cannot be used to track RNA in a cell over time leading to a static picture of a dynamic process. The importance of studying the temporal dynamics of RNA localization was recently highlighted when it was shown that RNA incorporation in stress granules is a transient process (Mollet, Cougot et al. 2008).

Live-cell RNA imaging methods

To date there are two approaches that dominate the field of live cell RNA imaging. The first is the method of expressing both the RNA of interest and the imaging reporter through the use of a plasmid based system. The second method is the targeting of RNA, either endogenous or plasmid derived, using an exogenous reporter delivered into the cell using microinjection, endocytosis, reversible membrane permiabilization, or cell penetrating peptides. This review will summarize the methods of previous RNA imaging studies, discuss the issues associated with RNA imaging in general, and will consider the issues involved specifically with the exogenous probe method.

Fluorescent Protein Based Methods

The state of the art in live cell RNA imaging is the expression of both the RNA of interest and fluorescent proteins that bind to expressed sequence. In this system one plasmid expresses an RNA sequence of interest that approximates the native RNA followed by repeats of a sequence that is recognized by an RNA binding protein (RBP). The second plasmid expresses the RBP as a fusion with a fluorescent protein. The basic idea is that the expressed RBP fluorescent protein fusions bind to the multiple binding sites in the expressed RNA raising the signal from the RNA above that of the background signal from unbound RBP fluorescent protein fusions. Several specific systems have been developed that utilize this basic method. The first, and currently most popular method, is the MS2 system (Bertrand, Chartrand et al. 1998). First described by Bertrand et al. 1998, this system utilizes a target RNA containing repeated stem loops following the coding sequence and a MS2 RBP fused to green fluorescent protein (MS2-GFP). This system has since been extended to achieve singe molecule sensitivity by the addition of 24 MS2 binding sites in the RNA (Fusco, Accornero et al. 2003; Shav-Tal, Darzacq et al. 2004).

Since each MS2 stem-loops bind two MS2-GFP proteins a maximum of 48 MS2-GFP proteins on each RNA is possible. In practice, Fusco et al. determined that approximately 30 bound proteins were necessary to detect single RNAs. Recently it was noted that the addition of 24MS2 binding sites prevented the nuclear export of RNA in certain circumstances necessitating the use of fewer sites (Yamagishi, Ishihama et al. 2009). The second system that uses this basic method is the λ_N binding protein system (Daigle and Ellenberg 2007; Lange, Katayama et al. 2008). This system also uses a target RNA with repeated stem loop binding domains, however the sequence is a 15-nucleotide hairpin (termed boxB) that is a target for a 22 amino acid peptide λ_{N22}. In this system, four repeats of boxB follow the coding sequence in the target RNA. This four-sequence repeat is targeted by a fusion protein that contains four consecutive repeats of the RBP λ_{N22} and three consecutive repeats of EGFP. This is slightly different than the MS2 system as the binding of multiple GFPs to the MS2 stem-loop is achieved independently while in the λ_{N22} system, there is essentially one binding site to which the fusion may bind. The third system is modified from the basic strategy in that it is not necessary to express the target RNA (Ozawa, Natori et al. 2007; Yamada, Yoshimura et al. 2011). In this system two pumilio homology domain (PUM-HD) RBPs are expresses as fusions to one half of a split fluorescent protein. The idea is that the RBP fusions target adjacent 8nt sequences in the RNA of interest so that when they both bind, the split fluorescent protein is reconstituted and become fluorescent. To target endogenous RNA the RBP must be mutated in vitro to bind with high affinity and specificity for two adjacent sequences. The main advantages to this system are that it allows for the imaging of endogenous RNA and it reduces the background fluorescence since unbound fusion proteins do not fluoresce.

Of these three systems, only the MS2 system, through the use of 24 binding domains, has been shown to be capable of single molecule sensitivity. In theory, both of the other systems could achieve single molecule sensitivity if a total of approximately 30 RBP-GFP molecules were bound to the RNA. However, while this is relatively easy to do in the λ_{N22} system by adding more 4xboxB repeats to the plasmid, in the pumillio system, one would have to mutate the PUM-HD protein so that over 30 sets of unique, adjacent 8-nucleotide sequences could be specifically targeted, which would be a huge technical challenge.

Plasmid derived RBP fusions offer tremendous flexibility in live cell RNA imaging, but there are some limitations to their use. Their primary limitation is that they have required the use of cell types that are readily transfected (Grunwald and Singer 2010). Since some cell types including many primary isolates do not lend themselves to efficient transfection, this limits researches to cell lines which might not be robust model systems. A second limitation is that plasmid derived mRNAs do not have the same structure as endogenous mRNAs as they are typically constructed without the correct number of introns or 3'-UTR sequence. Introns are essential to proper exon junction complex formation, which in turn can controls the localization of the mRNA (Hachet and Ephrussi 2004). The 3'-UTR has been shown to regulate the translational efficiency, decay, and stability or RNA. Plasmid derived mRNAs are also overexpressed, which may change the stoichiometry of the underlying gene expression. RBP-GFP systems also have limitations in the study of viral RNA, since the addition of bases to the genome of viruses can effect replication efficiency, assembly and viral egress.

Antisense RNA probe methods

An alternative to using an RBP-GFP system is to use exogenous probes that bind to RNA through Watson-Crick base pairing (Politz, Taneja et al. 1995). In this technique small ~20-base oligonucleotides with covalently bound organic fluorophores, termed RNA probes, hybridize in a sequence dependent manner to sites on an RNA of interest, which is often referred to as target. The theory behind this strategy is that because RNAs typically have single stranded sections amenable to complementary hybridization, if the RNA probes can be delivered into the cell, the hybridization events can occur and the target RNA can be tracked using microscopy. These exogenous probes can be introduced into the cell without the need for transfection of target RNA or RBP-GFP plasmids thereby allowing for the imaging of endogenous gene expression in a variety of cell types. However, there are a number of experimental considerations when using an exogenous RNA probe including probe structure, affinity (chemistry), sensitivity, and delivery.

Probe structure

Two physical structures of RNA probes have been used thus far in intracellular RNA imaging, linear probes and stem-loop probes. Linear probes are short (~20 base) oligonucleotides with no defined secondary structure. Stem-loop probes are similar to linear probes, except that they have complementary base sequences on their 5' and 3' ends that cause the probes to fold into a stem-loop secondary structure (Tyagi and Kramer 1996; Sokol, Zhang et al. 1998). Typically a fluorophore will be placed on the 5' end and a quencher on the 3' end of stem-loop probes. This configuration has been termed Molecular Beacon (MB) and was first described for use and characterized in vitro (Tyagi and Kramer 1996). The MB configuration brings the fluorophore and quencher

into close proximity when the probe is not bound to its target sequence thus decreasing the fluorescence from unbound probe. When bound to target, the fluorophore and quencher are physically separated which allows for the emission of signal from the fluorophore. Since molecular beacons could act as fluorescent switches it was hypothesized that they would yield a high signal to background in living cells when compared to linear probes (Molenaar, Marras et al. 2001). This was thought to be important in live cell RNA imaging because unbound probes are not washed away as in FISH and can contribute to background signal. In the case of linear probes, which can fluoresce whether or not they are bound to target, a sufficient SBR for imaging is achieved through the binding of multiple probes per target RNA and the accumulation of RNA into granules.

Probe structure can also have an effect on the specificity of probe binding. MBs were hypothesized to bind more specifically to a given target sequence than linear probes as evidenced from PCR data (Tsourkas, Behlke et al. 2003; Santangelo, Nix et al. 2004; Santangelo, Nitin et al. 2005; Santangelo, Nitin et al. 2006; Santangelo and Bao 2007). In order to improve specificity various methods utilizing fluorescence (Forster) resonance energy transfer (FRET) have been used with linear probes and molecular beacons. One method that uses autoligation probes, which are two linear probes that become covalently linked once bound to a target, has been used to study RNA in both imaging and flow cytometry applications (Silverman and Kool 2005; Abe and Kool 2006). In these FRET studies probes are designed to bind to two adjacent target sequences. Donor and acceptor fluorophores are placed on the appropriate end of the probe in order to bring them into close proximity when both are bound to the target. While they do appear to increase

signal specificity, the low signal obtained from RNA imaging FRET experiments keeps them from becoming a widely used technique.

Despite the promise of increased SBR and increased specificity using MBs over linear probes, in practice the results obtained from the two structures are similar. Both probes structures have been used to image RNA in living cells and it remains to be determined which structure will be generally advantageous (Molenaar, Marras et al. 2001).

Probe Affinity

The affinity of a probe to its target is another consideration in probe design. Changing the nucleic acids used to make the probes can change probe affinity independently of probe structure. Many different nucleic acid chemistries, other than RNA and DNA, have been developed for various purposes including Locked Nucleic Acids (LNA), Peptide nucleic acids (PNA), 2'-O-Methyl RNA, and phosphorothioate DNA (Egholm, Buchardt et al. 1993; Giles, Spiller et al. 1998; Molenaar, Marras et al. 2001; Kurreck, Wyszko et al. 2002; Vester and Wengel 2004; Wang, Yang et al. 2005). All four of these synthetic nucleic acid chemistries confer a degree of nuclease resistance to the oligonucleotide and change the melting temperature of the probe/target hybrid. The affinity of a probe for its RNA target, from highest to lowest, is as follows: LNA, PNA, 2'-O-Mehtyl RNA, RNA, DNA, and phosphorothioate DNA. The high melting temperatures of the higher affinity nucleic acids were thought to be unsuitable for use in live cells, which must be maintained at 37ºC. However, melting temperature studies are performed in solutions that contain higher free ion concentrations than intracellular

experiments (Santangelo 2010). This difference may limit the applicability of melting temperatures obtained in vitro to experiments involving intracellular hybridization. In fact antisense literature shows examples of specific binding using high affinity nucleic acid chemistries.

Peptide (polyamide) nucleic acids (PNA) are modified nucleic acids in which the deoxyribose phosphate backbone is replaced with a polyamide backbone (Nielsen, Egholm et al. 1991). The resulting molecule forms stable hybrids with both DNA and RNA and is nuclease resistant. Demidov et al. showed that PNA is also resistant to proteases in human serum, Eschericia coli, proteinase K, porcine intestinal mucosa peptidase, and mammalian cytoplasmic and nuclear extracts (Demidov, Cherny et al. 1994). PNA has been shown to follow the Watson-Crick base-pairing rules, which expedites their use as sequence specific RNA probes. Fluorescent PNA probes have been used to visualize the dynamics of telomeres in living cells and radiolabeled PNA probes have been used *in vivo* to measure gene expression in a Huntington's disease animal model (Lee, Boado et al. 2002) as well as MYC mRNA expression in a human breast cancer xenograft animal model (Tian, Aruva et al. 2005).

Locked nucleic acids (LNA) are oligonucleotide analogs that have a 2′-oxygen and the 4′-carbon atom linked with a methylene unit. Though they have not been used for live cell imaging applications, they have similar advantages as PNA and have been used in antisense knockdown and for detecting RNA using in situ hybridization (Thomsen, Nielsen et al. 2005). When compared to DNA FISH probes, LNA FISH probes had lower background and showed higher thermal stability.

Phosphorothioate DNA probes were the first modified oligonucleotides used to image RNA in living cells (Politz, Taneja et al. 1995; Politz, Browne et al. 1998). Phosphorothioate DNA was used for its superior nuclease resistance necessitated by the method of delivery, however, it was determined that the fluorophore modification to standard phosphodiester oligodeoxynucleotides (fl-DNA) conferred enough nuclease resistance for the authors to use standard fl-DNA in subsequent studies. In these ground-breaking studies the dynamics and localization of poly(A)+ RNA and beta-actin mRNA were analyzed (Politz, Tuft et al. 1999). The initial paper described delivery to both cytoplasmic and nuclear fluorescence signal and subsequent papers focused on the transport of poly(A)+ RNA in the nucleus.

Despite the importance of probe structure and affinity, few studies have directly compared live cell RNA imaging data obtained using different probes. Molenaar et al. performed the most detailed study comparing 2'-O-Methyl RNA and DNA linear probes to 2'-O-Methyl RNA and DNA MBs (Molenaar, Marras et al. 2001). They concluded that 2'-O-Methyl RNA linear probes gave the highest SBRs and were therefore the preferred probe chemistry and structure. The higher SBR using 2'-O-methyl RNA was later reaffirmed for the targeting of poly(A) tails of mRNA (Molenaar, Abdulle et al. 2004). In the 2004 study, 2'-O-Methyl RNA (U)22 probes were used to target poly(A)+ RNA in the cell nucleus and the results were compared to those obtained using poly(dT) DNA probes and to 2'-O-Methyl RNA probes that targeted RNA not present in the cells (A cytomegalovirus RNA). It was found that poly(dT) DNA probes and untargeted 2'-O-Me RNA probes diffused in the nucleus at rates 50 to 60 times that of poly(U) 2'OMe probes indicating that most of the signal form poly(dT) DNA probes arises from unbound

probes. In both of these studies they were only able to image nuclear RNA due to the use of microinjection probe delivery. Santangelo and Bao commented that higher SBRs were observed using MBs with 2'-O-Methyl hybridization domains over MBs containing DNA hybridization domains when targeting the RNA genome of human Respiratory Syncytial Virus in the cytoplasm but did not include linear structured probes in their comparison (Santangelo and Bao 2007).

Probe Sensitivity

Probe sensitivity depends on the binding efficiency of the probe and the reporter molecules used. Binding of the probe to the target is a function of the transport of the probe to the site of target, the concentration of probe, and the affinity of the probe for its target. These considerations are typically limited by the choice nucleic acid chemistry (see discussion above) and the delivery method (discussed in the following section) and will not be addressed here. Independent from the probe binding, however, is the choice of reporter molecule attached to the probe. Typical reporter molecules are the organic fluorescent dyes FITC, TAMRA, Cy3, Texas Red, and Cy5. These dyes, however, have low quantum efficiencies, low extinction coefficients, exhibit blinking and photobleach rapidly all of which contribute to limiting the sensitivity of these dyes in live cell experiments. In order to improve the sensitivity of RNA probes, newer high quantum efficiency and photostable fluorophores should be used. These include Cy3B and Atto 647N. To date only molecular beacons have been used as single molecule sensitive probes and in order to achieve this, 96 binding sites had to be incorporated into plasmid expression vectors (Vargas, Raj et al. 2005).

Intracellular Probe Delivery

One of the most challenging aspects of using RNA imaging probes is the delivery of the probes into the cell. The goal of any delivery strategy is to deliver a controllable amount of probe into the correct cellular compartment while maintaining the function of the probe and without disturbing the homeostasis of the cell. Methods used to deliver RNA probes include passive uptake, microinjection, cationic transfection, reversible membrane permiabilization, cell penetrating peptides, and electroporation. Passive pinocytosis was adapted from antisense studies and was the first method of delivering RNA probes into cells (Politz, Taneja et al. 1995). Delivery of Fluorescently labeled poly(A) phosphorothioate DNA was achieved by adding probe at 0.1-2uM concentrations to the growth media of cells for 2-4 hours. Probes were shown to have a punctuate pattern in the perinuclear region in addition to diffuse staining throughout the cell. In about one third of the cells nuclear fluorescence was brighter than cytoplasmic fluorescence. The punctuate signal was thought to be the result of probes that were endocytosed and trapped in vesicles. The diffuse staining was thought to be the result of probe that had escaped endocytotic vesicles and probe that was taken in by fluid phase pinocytosis. Nuclease resistant phosphorothioate DNA probes were used to prevent the breakdown of probes in the nuclease rich environment of lysosomes and endosomes.

RNA probes may also be introduced into the cell using microinjection. Microinjection delivery forces the probe into the cell by piercing the plasma membrane or nuclear membrane with a fine glass needle filled with the probe solution. Pressure is then applied to the solution forcing it into the cell. Microinjection has been used with both linear probes and MBs and, regardless of probe structure, RNA probes tend to accumulate in the nucleus of cells within 30 minutes of injection (Molenaar, Marras et al.

2001; Tyagi and Alsmadi 2004). Tyagi et al., using temperature and wheat germ agglutinin studies, attributed the accumulation of MBs in the nucleus to active transport. This accumulation has made it difficult to study RNA in the cytoplasm using RNA probes alone (Tyagi and Alsmadi 2004). To overcome this limitation, several methods have been developed to increase the concentration of probe in the cytoplasm. Streptavidin, dextran, and tRNA have been all complexed either covalently or non-covalently to the RNA probe to increase the molecular weight of the probe and physically block it from entering the nucleus via the nuclear pore complex (Mhlanga, Vargas et al. 2005). Adding these molecules to the probes allowed the researchers to study cytoplasmic RNA. Microinjection is limited in that it requires trained personnel to perform the injection and takes a significant amount of time to inject large numbers of cells, limiting its use in high throughput assays. Molenaar et al. also noted that a significant amount of background fluorescence was detected with microinjected MBs once they entered the nucleus indicating a nonspecific opening of the structure (Molenaar, Marras et al. 2001).

Another method of delivering RNA probes into the cell is reversible membrane permeabilization. Pore forming toxins, such as Streptolysin-O (SLO), have been used to deliver proteins, carbohydrates and nucleic acids into the cytoplasm of many different cell types (Barry, Gesek et al. 1993; Bhakdi, Weller et al. 1993; Giles, Ruddell et al. 1995; Paillasson, Van De Corput et al. 1997; Giles, Spiller et al. 1998; Spiller, Giles et al. 1998; Walev, Bhakdi et al. 2001; Abe and Kool 2006). A member of the thio-activated cholesterol-binding cytolysins, SLO monomers insert into the cell membrane in cholesterol rich areas and subsequently oligomerize into rings forming pores up to 30nm

in diameter containing approximately 50 monomers (Sekiya, Danbara et al. 1996). The size of the pores formed allows for transport of ions, small molecules and macromolecules across the membrane of virtually every animal cell. Initially studied for its cytotoxic effects, non-lethal SLO membrane permeabilization and reversible membrane permiabilization protocols have been developed and optimized for a variety of cell types. Typically, SLO solutions are reduced using TCEP or DTT for about 1 hour. The SLO and RNA probes are then added to serum free media which is placed on a cell monolayer for about 10 minutes after which the media is replaced with normal growth media. SLO delivery has been generally shown to be independent of the endocytic pathway. Specifically, RNA probes labeled with FITC have been shown to be efficiently delivered through the cytoplasm and into the nucleus under reversible membrane permeabilization conditions(Paillasson, Van De Corput et al. 1997). MBs targeting viral RNA and endogenous mRNA have also been shown to be delivered into the cytoplasm.

Cell permeable peptides are short, basic polypeptides that can be conjugated to a variety of macromolecules and induce them to translocate across the cell membrane (Rinne, Albarran et al. 2007; Ter-Avetisyan, Tunnemann et al. 2009; Margus, Padari et al. 2012). CPP based delivery is similar to that of pore-forming toxins, in that they result in ~100% delivery efficiency. However, CPPs have a distinct advantage as they can be used *in vivo* while most other methods cannot. Whether or not CPP use the endocytic pathway is a matter of debate, however, it seems to be a cargo dependent pathway. Cargo larger than ~30kD appears to enter the cell through endocytosis while cargo under 30kD enters the cell through an uncharacterized non-endocytic modality (Rinne, Albarran et al.

2007; Ter-Avetisyan, Tunnemann et al. 2009). CPP delivery of MB yields similar results to SLO delivery (Nitin, Santangelo et al. 2004; Nitin, LaConte et al. 2009).

Imaging modalities

No matter which method of tagging the RNA is employed, the choice of imaging modalities is both crucial to the overall method and the selection of an imaging method, through seemingly easy, is non-trivial. Two microscopic imaging methods dominate the field of biomedical imaging, epifluorescent widefield microscopy, either with or without deconvolution, and fluorescent confocal imaging. Ideally, the strategy used to fluorescently label RNAs will be compatible with both modalities. There are two reasons for this. First, in order to be widely adopted, a method should be as broadly applicable as possible. Second, biological samples are not always amenable to one particular imaging modality. To better understand the why one modality would be preferred over another; one must analyze the advantages and disadvantages of each system. The advantage to a widefield, deconvolution microscopes are:

1. Sensitivity, owing to the low noise of cooled CCD detectors and broad band emission, excitation filters
2. Speed, owing to the entire field capture
3. Cost, as widefield microscopes are ~1/5 the cost of line scanning confocal
4. Low photobleaching, owing to the lower power excitation sources.

When combined with, three-dimensional (3D) deconvolution, also known as image restoration, widefield microscopy can render a 3D image stack without the out-of-focus

florescence signal typically found in epifluorescent images (Biggs 2010). There are also several disadvantages to this imaging modality as well:

1. Limited dynamic range, since all pixels must be below the saturation value of the A/D converter.
2. A full 3D image stack must be captured for deconvolution
3. Slow, since the deconvolution algorithm is computationally intensive
4. Morphologically specific, since deconvolution algorithms work best on localized, non-diffuse signal and ideally on punctae.

Confocal microscopes can complement widefield microscopy and overcome some of the limitations imposed by them. The advantages to using confocal based imaging techniques are:

1. Removal of out of focus light without post-processing
2. Ability to saturate image segments, allowing for the imaging of lower intensity signal
3. Ability to image a single optical section without out-of-focus light

The disadvantages to confocal imaging are:

1. Slow data acquisition, line scanning confocals can take up to 20 min to aquire an image stack
2. Photobleaching, high intensity laser illumination can irreversibly damage fluorophores
3. Limited sensitivity, due to the noise (shot and gain)

4. Expensive equipment, costing > four times the amount of equivalent widefield microscopes

Taking these characteristics into consideration, the imaging modality utilized in the proceeding chapters was chosen to take advantage of the strength of each modality. For instance, when imaging discrete granules, as is the case in the beta-actin mRNA studies, widefield deconvolution was used. However, in the case of viral RNA and filament imaging, widefield, deconvolution microscopy was insufficient to capture the full dynamic range of the biological sample, and thus confocal microscopy was used to demonstrate the subcellular localization of viral RNA and colocalization with nucleocapsid proteins and host factors.

Analysis methods

While tagging RNA with a label molecule and imaging the RNA inside live and fixed cells is crucial to the study of spatial RNA biology, it is not sufficient as part of a complete method to study specific biological problems. The final aspect of designing a molecular imaging strategy is to develop analysis methods to be used to turn raw imaging data into usable information to test hypothesis. Analysis methods can be broken down into many categories, but for the current work they will be broken into two general methods, RNA alone and co-analysis with other factors. In the RNA alone methods there are fixed cell analyses which include RNA localization, intensity of signal, and morphology, and there are live cell analyses, which include single particle tracking and whole cell analyses (Kislauskis and Singer 1992; Singer 1992; Saxton 1994; Saxton 1995; Saxton 1997; Saxton and Jacobson 1997; Babcock, Chen et al. 2004; Condeelis

and Singer 2005; Saxton 2007; Saxton 2008; Park, Buxbaum et al. 2010). In the colocalization methods there are whole cell automatic colocalization techniques, which include Manders' and Pearson's overlap coefficients and there are subcellular methods such as granule colocalization and intensity line plots. Each of these methods have strengths and weaknesses, and any techniques that will be used to comprehensively study the spatial biology of RNA should ideally be amenable to analysis by any of them

In RNA only methods three important, fixed cell techniques have been utilized. RNA localization was one of the first described. In this analysis method, the special position of RNA is mapped either quantitatively with respect to a point of origin or its position is categorized into distinct cellular compartments. The cellular compartment method is amenable to situations where distinct locations, such as membrane bound structures, cytoskeletal structures, or large protein aggregates, can be classified. The point of origin localization method is suitable for situations where distinct cellular compartments do not exist or have not yet been described.

For the analysis of RNA dynamics in live cells two general approaches may be taken to, following single RNAs through their motions and following the paths of all the RNAs within the cell. These may be thought of, respectively, as the equivalent of Lagrangian and Eulerian analyses in fluid mechanics. Following single RNAs, usually termed single particle tracking, can shed light on several important aspect of molecular dynamics, including diffusion coefficient and transport velocity which give information on the molecular environment and motor driven transport, respectively. Single particle tracking can also give information about time dependent phenomena, such as hindered or corralled motion, and temporal changes in environments, such as when particles change

from one mode of transport to another. Single particle tracking has been used for several decades to study the motion of receptor proteins in the plasma membrane but has only recently been used in the field of RNA dynamics. The crucial aspect to the techniques is the ability to image single particles (either aggregates that move together or single molecules). For this reason, the use of single particle tracking coincided with the first methods for single molecule labeling of RNA. Previous studies using single particle tracking have shown RNAs undergo diffusion, hindered diffusion, motor driven transport, although, the results of individual studies come to disparate conclusions both quantitatively and qualitatively.

Prior to the advent of single molecule RNA labeling techniques, other methods needed to be used for analyzing the motion of RNAs. Principally, fluorescence recovery after photobleaching (FRAP) has been used to determine the transport characteristics of tagged RNAs. Used in both probe and fusion-protein based methods FRAP can be used to determine if the tag is attached to the RNA and to measure the diffusion coefficient and mobile vs. immobile fraction of RNA. In Mili et al, FRAP was used to determine that RNAs were not sequestered and stored into stress granules but rather transiently resided within them. FRAP has also been used to study the differential mobility of RNAs in the nucleus versus the cytoplasm. FRAP has generally been useful in the analysis of free diffusing particles such as small organic molecules and small proteins. However, due to its averaging nature, exact measurements of velocity and diffusion coefficients are difficult to obtain and transport mode switching is impossible to separate from other phenomena, such as hindered or enhanced diffusion.

The analysis of RNAs can lead to insights into their environment and function, however, more detailed information about their function can be gleaned primarily through the interaction of RNA with trans-acting factors and host proteins. The primary method of colocalization is whole cell, automatic colocalization methods. These methods have the advantage of limiting user bias as they calculate measures of colocalization over whole cells or population of cells. They have limitations when two species are present in disparate quantities, they have different morphologies, or are both diffusely localized as to fill the cellular compartment. Other methods include granule level colocalization, where granules are identified based upon one marker, and the colocalization with a second molecular marker is analyzed by thresholding methods. Lastly, the coincidence of signal in specific cellular locations can be qualitatively assessed using intensity value line plots where the intensity of each signal is visualized along a line selected from the 2D image. This method can show colocalization in cellular compartments not seen throughout the entire cell.

Discussion

Many probe-based methods have been developed for tracking RNA in living cells with few general guidelines available for researchers to select *a priori* the best protocols for their needs. The following suggestions should help researchers new to RNA tracking focus their experiments. The first consideration in a live cell RNA imaging study is to determine the method of delivery is best for their experiment. The authors suggest that researchers new to RNA tracking try SLO delivery first using previously described protocols. SLO delivery allows for high throughput screens as probe is delivered to the entire monolayer in less than half an hour with some protocols. The amount of plasma

membrane cholesterol can vary between cell types, so optimization of protocols may be necessary for efficient delivery to different cell lines or primary isolates. SLO delivery also delivers probe into both the cytoplasm and nucleus without the need to conjugate RNA probes to larger molecules such as streptavidin, tRNA or dextran. Changing the concentration of probe incubated during permeabilization can modulate the amount of delivered probe much in the same way that Politz et al. changed the amount of probe delivered by endocytosis. Microinjection is an excellent alternative, but it requires specialized equipment, and technicians must be trained in its use before it can be fully implemented. Microinjection also precludes high throughput screens as probe delivery proceeds one cell at a time.

The second consideration for live cell RNA tracking is the choice of probe, both in choice of nucleic acid chemistry, structure and sequence. Choice of sequence has not been addressed in much of the literature for specific RNAs of interest, and the authors suggest using sequences that have proven effective in the siRNA or antisense literature. The goals of imaging and gene knockdown are distinct; they both require sites that are available for base pairing. Complications may arise if the RNA changes structure as in stress granules or P-bodies. In general it is advantageous to compare live cell RNA imaging results with those obtained from FISH studies using the same probe. The studies that have compared higher affinity 2'-O-Methyl RNA probes to DNA probes have all found the higher affinity probes to provide superior signal-to-background ratios. We therefore recommend probes be constructed mostly with 2'-OMe RNA and amine-modified thymidines for conjugating fluorophores. We also recommend researchers use

linear structured probes first as they are more economical and have been shown to have higher affinity for their targets when compared to MBs.

Conclusion

There has been considerable development in live cell RNA imaging technology in the past decade; however, there are still some developments that need to be made in order to bring this technology into the labs of non-specialists. First RNA probes must be developed that are single molecule sensitive when used with endogenous RNA. RNAs that don't aggregate and are in low copy number are not able to be tracked without highly sensitive probes. Moreover, it is unknown how the large molecular weight additions and overexpression of RNA in the plasmid based systems affects the fundamental biology. Second, the ability to use RNA imaging probes for both fluorescence and electron microscopy would allow researchers to confirm the localization of RNA into compartments too small to be resolved under light microscopy such as viral particles. Third, RNA probes must be made compatible with probes for imaging proteins. The fate and function of RNA is determined by the binding proteins bound to it in a ribonucleoprotein complex and the ability to image protein and RNA simultaneously would be of great advantage when following an RNA from transcription to degradation.

References

Abe, H. and E. T. Kool (2006). "Flow cytometric detection of specific RNAs in native human cells with quenched autoligating FRET probes." Proc Natl Acad Sci U S A **103**(2): 263-268.

Anderson, P. and N. Kedersha (2006). "RNA granules." J Cell Biol **172**(6): 803-808.

Anderson, P. and N. Kedersha (2008). "Stress granules: the Tao of RNA triage." Trends Biochem Sci **33**(3): 141-150.

Anderson, P. and N. Kedersha (2009). "RNA granules: post-transcriptional and epigenetic modulators of gene expression." Nat Rev Mol Cell Biol **10**(6): 430-436.

Anderson, P. and N. Kedersha (2009). "Stress granules." Curr Biol **19**(10): R397-398.

Babcock, H. P., C. Chen, et al. (2004). "Using single-particle tracking to study nuclear trafficking of viral genes." Biophys J **87**(4): 2749-2758.

Barry, E. L., F. A. Gesek, et al. (1993). "Introduction of antisense oligonucleotides into cells by permeabilization with streptolysin O." Biotechniques **15**(6): 1016-1018, 1020.

Bertrand, E., P. Chartrand, et al. (1998). "Localization of ASH1 mRNA particles in living yeast." Mol Cell **2**(4): 437-445.

Bhakdi, S., U. Weller, et al. (1993). "A guide to the use of pore-forming toxins for controlled permeabilization of cell membranes." Med Microbiol Immunol **182**(4): 167-175.

Biggs, D. S. (2010). "3D deconvolution microscopy." Curr Protoc Cytom **Chapter 12**: Unit 12 19 11-20.

Buchan, J. R. and R. Parker (2009). "Eukaryotic stress granules: the ins and outs of translation." Mol Cell **36**(6): 932-941.

Condeelis, J. and R. H. Singer (2005). "How and why does beta-actin mRNA target?" Biol Cell **97**(1): 97-110.

Daigle, N. and J. Ellenberg (2007). "LambdaN-GFP: an RNA reporter system for live-cell imaging." Nat Methods **4**(8): 633-636.

Demidov, V. V., D. I. Cherny, et al. (1994). "Electron microscopy mapping of oligopurine tracts in duplex DNA by peptide nucleic acid targeting." Nucleic Acids Res **22**(24): 5218-5222.

Egholm, M., O. Buchardt, et al. (1993). "PNA hybridizes to complementary oligonucleotides obeying the Watson-Crick hydrogen-bonding rules." Nature **365**(6446): 566-568.

Fusco, D., N. Accornero, et al. (2003). "Single mRNA molecules demonstrate probabilistic movement in living mammalian cells." Curr Biol **13**(2): 161-167.

Gandhi, S. J., D. Zenklusen, et al. (2011). "Transcription of functionally related constitutive genes is not coordinated." Nat Struct Mol Biol **18**(1): 27-34.

Gaspar, I. (2011). "Microtubule-based motor-mediated mRNA localization in Drosophila oocytes and embryos." Biochem Soc Trans **39**(5): 1197-1201.

Giles, R. V., C. J. Ruddell, et al. (1995). "Single base discrimination for ribonuclease H-dependent antisense effects within intact human leukaemia cells." Nucleic Acids Res **23**(6): 954-961.

Giles, R. V., D. G. Spiller, et al. (1998). "Selecting optimal oligonucleotide composition for maximal antisense effect following streptolysin O-mediated delivery into human leukaemia cells." Nucleic Acids Res **26**(7): 1567-1575.
Grunwald, D. and R. H. Singer (2010). "In vivo imaging of labelled endogenous beta-actin mRNA during nucleocytoplasmic transport." Nature **467**(7315): 604-607.
Hachet, O. and A. Ephrussi (2004). "Splicing of oskar RNA in the nucleus is coupled to its cytoplasmic localization." Nature **428**(6986): 959-963.
Kedersha, N. and P. Anderson (2007). "Mammalian stress granules and processing bodies." Methods Enzymol **431**: 61-81.
Kedersha, N., G. Stoecklin, et al. (2005). "Stress granules and processing bodies are dynamically linked sites of mRNP remodeling." J Cell Biol **169**(6): 871-884.
Kedersha, N., S. Tisdale, et al. (2008). "Real-time and quantitative imaging of mammalian stress granules and processing bodies." Methods Enzymol **448**: 521-552.
Kislauskis, E. H. and R. H. Singer (1992). "Determinants of mRNA localization." Curr Opin Cell Biol **4**(6): 975-978.
Kurreck, J., E. Wyszko, et al. (2002). "Design of antisense oligonucleotides stabilized by locked nucleic acids." Nucleic Acids Res **30**(9): 1911-1918.
Lange, S., Y. Katayama, et al. (2008). "Simultaneous transport of different localized mRNA species revealed by live-cell imaging." Traffic **9**(8): 1256-1267.
Lee, H. J., R. J. Boado, et al. (2002). "Imaging gene expression in the brain in vivo in a transgenic mouse model of Huntington's disease with an antisense radiopharmaceutical and drug-targeting technology." J Nucl Med **43**(7): 948-956.
Lin, W. J., A. Duffy, et al. (2007). "Localization of AU-rich element-containing mRNA in cytoplasmic granules containing exosome subunits." J Biol Chem **282**(27): 19958-19968.
Margus, H., K. Padari, et al. (2012). "Cell-penetrating Peptides as Versatile Vehicles for Oligonucleotide Delivery." Mol Ther.
Mhlanga, M. M., D. Y. Vargas, et al. (2005). "tRNA-linked molecular beacons for imaging mRNAs in the cytoplasm of living cells." Nucleic Acids Res **33**(6): 1902-1912.
Molenaar, C., A. Abdulle, et al. (2004). "Poly(A)+ RNAs roam the cell nucleus and pass through speckle domains in transcriptionally active and inactive cells." J Cell Biol **165**(2): 191-202.
Molenaar, C., S. A. Marras, et al. (2001). "Linear 2' O-Methyl RNA probes for the visualization of RNA in living cells." Nucleic Acids Res **29**(17): E89-89.
Mollet, S., N. Cougot, et al. (2008). "Translationally repressed mRNA transiently cycles through stress granules during stress." Mol Biol Cell **19**(10): 4469-4479.
Moore, M. J. (2005). "From birth to death: the complex lives of eukaryotic mRNAs." Science **309**(5740): 1514-1518.
Nielsen, P. E., M. Egholm, et al. (1991). "Sequence-selective recognition of DNA by strand displacement with a thymine-substituted polyamide." Science **254**(5037): 1497-1500.
Nitin, N., L. LaConte, et al. (2009). "Tat peptide is capable of importing large nanoparticles across nuclear membrane in digitonin permeabilized cells." Ann Biomed Eng **37**(10): 2018-2027.

Nitin, N., P. J. Santangelo, et al. (2004). "Peptide-linked molecular beacons for efficient delivery and rapid mRNA detection in living cells." Nucleic Acids Res **32**(6): e58.
Ozawa, T., Y. Natori, et al. (2007). "Imaging dynamics of endogenous mitochondrial RNA in single living cells." Nat Methods **4**(5): 413-419.
Paillasson, S., M. Van De Corput, et al. (1997). "In situ hybridization in living cells: detection of RNA molecules." Exp Cell Res **231**(1): 226-233.
Park, H. Y., A. R. Buxbaum, et al. (2010). "Single mRNA tracking in live cells." Methods Enzymol **472**: 387-406.
Politz, J. C., E. S. Browne, et al. (1998). "Intranuclear diffusion and hybridization state of oligonucleotides measured by fluorescence correlation spectroscopy in living cells." Proc Natl Acad Sci U S A **95**(11): 6043-6048.
Politz, J. C., K. L. Taneja, et al. (1995). "Characterization of hybridization between synthetic oligodeoxynucleotides and RNA in living cells." Nucleic Acids Res **23**(24): 4946-4953.
Politz, J. C., R. A. Tuft, et al. (1999). "Movement of nuclear poly(A) RNA throughout the interchromatin space in living cells." Curr Biol **9**(6): 285-291.
Rinne, J., B. Albarran, et al. (2007). "Internalization of novel non-viral vector TAT-streptavidin into human cells." BMC Biotechnol **7**: 1.
Santangelo, P., N. Nitin, et al. (2006). "Live-cell characterization and analysis of a clinical isolate of bovine respiratory syncytial virus, using molecular beacons." J Virol **80**(2): 682-688.
Santangelo, P. J. (2010). "Molecular beacons and related probes for intracellular RNA imaging." Wiley Interdisciplinary Reviews: Nanomedicine and Nanobiotechnology **2**(1): 11-19.
Santangelo, P. J. and G. Bao (2007). "Dynamics of filamentous viral RNPs prior to egress." Nucleic Acids Res **35**(11): 3602-3611.
Santangelo, P. J., N. Nitin, et al. (2005). "Direct visualization of mRNA colocalization with mitochondria in living cells using molecular beacons." J Biomed Opt **10**(4): 44025.
Santangelo, P. J., B. Nix, et al. (2004). "Dual FRET molecular beacons for mRNA detection in living cells." Nucleic Acids Res **32**(6): e57.
Saxton, M. J. (1994). "Single-particle tracking: models of directed transport." Biophys J **67**(5): 2110-2119.
Saxton, M. J. (1995). "Single-particle tracking: effects of corrals." Biophys J **69**(2): 389-398.
Saxton, M. J. (1997). "Single-particle tracking: the distribution of diffusion coefficients." Biophys J **72**(4): 1744-1753.
Saxton, M. J. (2007). "A biological interpretation of transient anomalous subdiffusion. I. Qualitative model." Biophys J **92**(4): 1178-1191.
Saxton, M. J. (2008). "Single-particle tracking: connecting the dots." Nat Methods **5**(8): 671-672.
Saxton, M. J. and K. Jacobson (1997). "Single-particle tracking: applications to membrane dynamics." Annu Rev Biophys Biomol Struct **26**: 373-399.
Schwanhausser, B., D. Busse, et al. (2011). "Global quantification of mammalian gene expression control." Nature **473**(7347): 337-342.

Sekiya, K., H. Danbara, et al. (1996). "Electron microscopic evaluation of a two-step theory of pore formation by streptolysin O." J Bacteriol **178**(23): 6998-7002.
Shav-Tal, Y., X. Darzacq, et al. (2004). "Dynamics of single mRNPs in nuclei of living cells." Science **304**(5678): 1797-1800.
Silverman, A. P. and E. T. Kool (2005). "Quenched autoligation probes allow discrimination of live bacterial species by single nucleotide differences in rRNA." Nucleic Acids Res **33**(15): 4978-4986.
Singer, R. H. (1992). "The cytoskeleton and mRNA localization." Current Opinion in Cell Biology **4**: 15-19.
Sokol, D. L., X. Zhang, et al. (1998). "Real time detection of DNA.RNA hybridization in living cells." Proc Natl Acad Sci U S A **95**(20): 11538-11543.
Spiller, D. G., R. V. Giles, et al. (1998). "Improving the intracellular delivery and molecular efficacy of antisense oligonucleotides in chronic myeloid leukemia cells: a comparison of streptolysin-O permeabilization, electroporation, and lipophilic conjugation." Blood **91**(12): 4738-4746.
Sundell, C. L. and R. H. Singer (1991). "Requirement of microfilaments in sorting of actin mRNAs." Science **253**: 1275-1277.
Ter-Avetisyan, G., G. Tunnemann, et al. (2009). "Cell entry of arginine-rich peptides is independent of endocytosis." J Biol Chem **284**(6): 3370-3378.
Thomsen, R., P. S. Nielsen, et al. (2005). "Dramatically improved RNA in situ hybridization signals using LNA-modified probes." RNA **11**(11): 1745-1748.
Tian, X., M. R. Aruva, et al. (2005). "Noninvasive molecular imaging of MYC mRNA expression in human breast cancer xenografts with a [99mTc]peptide-peptide nucleic acid-peptide chimera." Bioconjug Chem **16**(1): 70-79.
Tomecki, R., K. Drazkowska, et al. (2010). "Mechanisms of RNA degradation by the eukaryotic exosome." Chembiochem **11**(7): 938-945.
Tomecki, R. and A. Dziembowski (2010). "Novel endoribonucleases as central players in various pathways of eukaryotic RNA metabolism." RNA **16**(9): 1692-1724.
Tsourkas, A., M. A. Behlke, et al. (2003). "Hybridization of 2'-O-methyl and 2'-deoxy molecular beacons to RNA and DNA targets." Nucleic Acids Res **31**(6): 5168-5174.
Tyagi, S. and O. Alsmadi (2004). "Imaging native beta-actin mRNA in motile fibroblasts." Biophys J **87**(6): 4153-4162.
Tyagi, S. and F. R. Kramer (1996). "Molecular beacons: probes that fluoresce upon hybridization." Nat Biotechnol **14**(3): 303-308.
Vargas, D. Y., A. Raj, et al. (2005). "Mechanism of mRNA transport in the nucleus." Proc Natl Acad Sci U S A **102**(47): 17008-17013.
Vester, B. and J. Wengel (2004). "LNA (locked nucleic acid): high-affinity targeting of complementary RNA and DNA." Biochemistry **43**(42): 13233-13241.
Walev, I., S. C. Bhakdi, et al. (2001). "Delivery of proteins into living cells by reversible membrane permeabilization with streptolysin-O." Proc Natl Acad Sci U S A **98**(6): 3185-3190.
Wang, L., C. J. Yang, et al. (2005). "Locked nucleic acid molecular beacons." J Am Chem Soc **127**(45): 15664-15665.
Yamada, T., H. Yoshimura, et al. (2011). "Visualization of non-engineered single mRNAs in living cells using genetically encoded fluorescent probes." Anal Chem.

Yamagishi, M., Y. Ishihama, et al. (2009). "Single-molecule imaging of beta-actin mRNAs in the cytoplasm of a living cell." Exp Cell Res **315**(7): 1142-1147.

CHAPTER 2

PROBE DESIGN AND TARGETING STRATEGY

Background

There are currently few methods used to image RNA at the single molecule level. Current techniques involve the use of a vast excess of probes or plasmid-derived RNA to image RNA with single-molecule sensitivity. Either both the RNA and probe are expressed from a plasmid, requiring binding of up to 48 MS2-GFP(Fusco, Accornero et al. 2003; Shav-Tal, Darzacq et al. 2004) molecules, or just the RNA is expressed from a plasmid, requiring binding sites for 96 molecular beacon probes(Vargas, Raj et al. 2005) to achieve single-molecule sensitivity. As plasmid-derived RNA restricts usage to cell types that can be efficiently transfected and is susceptible to artifacts caused by over expression, imaging native RNA is preferred, but requires a more sensitive probe to achieve single-molecule sensitivity with a limited number of bound probes.

The probes we designed to image native, non-engineered RNA in the cellular environment were based on the premise of small, complimentary oligonucleotide ligand that, once delivered to the right cellular compartment, would recognize and bind to its target through Watson-Crick base pairing (Politz, Taneja et al. 1995; Politz, Browne et al. 1998). This design strategy allows for the specific labeling of RNA without the need for inserting aptamer tags and allows for probe designing based on the sequence of the target, which is, in most cases, already known. The oligonucleotide probe strategy was selected over alternative methods as it is the most likely strategy to allow for the targeting of endogenous, non-engineered RNA in live cells. The only other method that allows for the

targeting of endogenous, non-engineered RNA is the Pumillio fusion protein method. This method, however, is not ideal as the protein engineering cannot be performed *a priori*, the fluorophores used for detection must be fluorescent proteins (typically spit, fluorescent proteins) which limits sensitivity, and requires cell lines that can be transfected with multiple plasmids (Ozawa, Natori et al. 2007).

A linear, non-hairpin probe was chosen over molecular beacon designs for several reasons. First, linear probes allowed for more fluorophores per oligonucleotide ligand. This was important for adding as many fluorophores as possible to the overall probe. Second, linear probes are approximately half the cost of molecular beacons. Third, linear probes have faster binding kinetics than molecular beacons (Molenaar, Marras et al. 2001). Fourth, linear probes, which can be internally labeled with fluorophores, had fewer complications with non-specific interactions with cellular components (Rhee and Bao 2010).

This study was the first to develop a method for single-molecule sensitive labeling of non-engineered RNA in living cells. Other methods had been developed either for single-molecule sensitive labeling plasmid derived mRNA in living cells or native mRNA in fixed cells; however, to confirm the data obtained through engineered mRNA and to extend live-cell tracking of RNA to molecules that cannot function physiologically as engineered RNA, a new approach needed be developed. Furthermore, this approach allows for adjustments in several crucial areas of probe design including affinity, photophysical characteristics, physical characteristics such as molecular weight and hydrodynamic diameter, and intracellular delivery methods. By developing a modular

technique this method can be adapted to imaging diverse RNAs, imaging in RNAs in many different cell types, and imaging RNAs using assorted microscopical techniques.

Probe synthesis and assembly

The synthesis of RNA imaging probes involved three steps. First was the synthesis of the oligonucleotide ligands that served two purposes. They determined the molecular targeting of the probe by sequence complementarity with the target and served as the platform for attaching organic fluorophores used for detection of the probes. Oligonucleotides were purchased commercially as the technology for short oligonucleotide synthesis is mature and they could be purchased inexpensively, synthesized quickly and with high purity. The sequence of the oligonucleotides was complimentary to target sequences in the RNA of interest. Target sequences were determined by three criteria:

1. The target sequence was between 15-25 nucleotides long
2. The target sequence did not have any homology in other transcripts
3. The target sequence did not overlap with the binding sites of known RNA binding proteins (e.g. AU rich regions for ARE binding proteins)

The second step in the synthesis of the probes was the attachment of fluorophores to the oligonucleotide ligands. The ligands were designed with multiple internal functional groups for labeling with fluorophores. Multiple labeling increased the brightness of each ligand while keeping the molecular weight and diameter of the overall probe relatively unchanged. Self-quenching by over-labeling was a concern, and, as a result, the internal labels were spaced >2 bases apart, and the number of fluorophores was

limited to 2-5 per ligand. To achieve this labeling the number of internal reactive groups were between 5 and 10 per ligand. Internal amines, specifically C6-dT-amines, were used to attach NHS-ester modified fluorophores. Amine modified nucleotides were added to oligonucleotides with high yields and can be combined with thiol-maleimide labeling for heterogeneous conjugation. Several fluorophores were available for conjugation and were chosen based upon their extinction coefficient, quantum yield, propensity for self-quenching, and spectral characteristics. By conjugating the small-molecule organic fluorophores to internal amines we were able to adjust the spectral characteristics of the probe without resynthesizing the ligand. Ligand-fluorophore conjugates are separated from free fluorophores by diafiltration, an inexpensive (~$3) and fast (~1hr) method of separating larger conjugates from smaller molecules, in this case the 10kDa ligands and <1kDa fluorophores.

The third step in the synthesis of the RNA probes was homo-oligomerization of the ligands. This step served to increase the brightness of the overall probe by providing additional fluorophores and to increase the binding kinetics of individual probes. By adding additional fluorophores to each probe by linking multiple ligands together, self-quenching was minimized as each fluorophore was separated by the same distance as in a single ligand. Oligomerization of the ligands also served to increase the affinity of each probe, due to polyvalent effects, while the same concentration of probe was maintained. While unlikely, the possibility of crosslinking RNA due to the polyvalent nature of the probes was assessed by comparing the number of RNA granules detected using monovalent probes and polyvalent probes. Oligomerization was achieved in two ways. First, individual ligands were 5' modified with biotin and then tetramerized by incubation

with a biotin binding protein, neutravidin or streptavidin. Tetramerization via the biotin-streptavidin linkage is fast due to the strong binding properties of biotin-streptavidin (K_d~10^{-15}M), and allowed for exactly 4 ligands per probe, simplifying quantitation and purification. Second, ligands were be 5' modified with a thiol group and oligomerized using multivalent polyethylene glycol (PEG) cores with maleimide (thiol-reactive) groups. Using a PEG core offered several advantages including lower molecular weight and hydrodynamic diameter, compatibility with cell penetrating peptide delivery strategies, and covalent attachment of ligands to the core. Using a biotin binding proteinaceous core had an additional advantage of restricting the probes to the cytoplasm. By restricting probes to the cytoplasm, analysis was simplified and nonspecific nuclear interactions, specifically nucleoli interactions, were minimized (Tyagi and Alsmadi 2004).

To this end we designed and synthesized multiply labeled tetravalent RNA imaging probes (MTRIPs) composed of a 2′-*O*-methyl RNA-DNA chimera nucleic acid ligand with four or five amino-modified thymidines, 5′ biotin modification and a short (5–7-base) poly(T) sequence to extend the ligands from the surface of streptavidin. We used the amino-modified thymidines to conjugate *N*-hydroxysuccinimide (NHS) ester–modified fluorophores to the ligand. On average, each ligand was labeled with three fluorophores, limiting self-quenching. We chose fluorophores with quantum yields above 65% and they exhibited little triplet state excitation. The multiply labeled monovalent ligands were tetramerized via their binding to streptavidin, which increased probe brightness fourfold **Figure 2.1**.

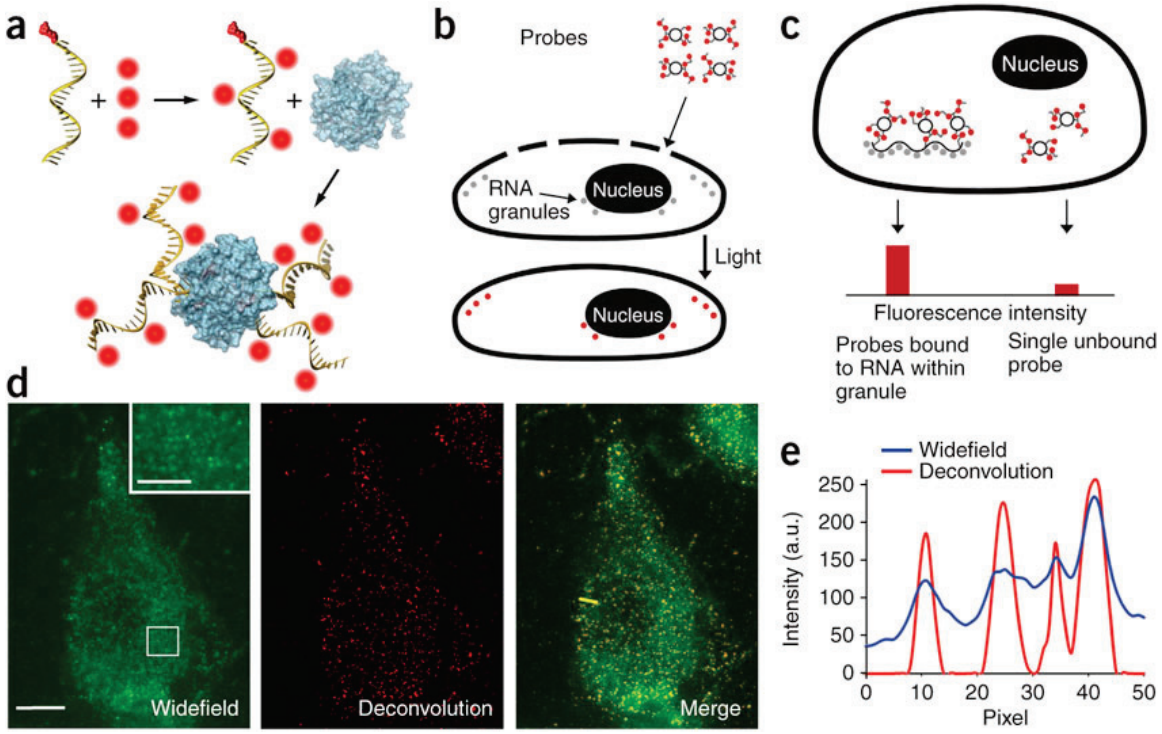

Figure 2.1: **Assembly of MTRIPs and delivery into live cells.** (a) Fluorophores (red) were conjugated to amino-modified chimera oligonucleotides and bound to streptavidin (blue). (b) Cells, permeabilized with streptolysin O, allowed probe diffusion through pores; this was followed by rapid binding of the probes to targets, which was visualized after light stimulation. (c) Single RNAs bound to multiple probes were recognized by the enhanced signal-to-background ratio. (d) Live-cell widefield, deconvolved and merged images of a single optical plane of Cy3B-labeled hRSV-targeted probes in a noninfected A549 cell. Scale bars, 10 μm (2.5 μm in inset, which is a magnification of the boxed region). (e) Intensity profile of widefield and deconvolved images through yellow line in the merge image in d.

In vitro testing and characterization

To determine the utility of these RNA probes in studying the localization the dynamics of RNA, criteria for assessing functionality must be established. The first criterion was that probes should allow for single-molecule sensitive detection of mRNA throughout the volume of the cell. The second criterion was that probe should remain fluorescent long enough to determine the transport characteristics of the RNA within timescales necessary for studying RNA dynamics. The third criterion was that probes must not interfere with the localization of mRNA. The fourth criterion was that probes must not interfere with physiology of the target RNA. In the case of mRNA this was gene expression and for viral genomic RNA it was viral production. With these criteria for assessing the utility of the probes, several specific goals can be established with regard to the characterization of out RNA imaging probes.

1. Individual probes must be detectable by standard widefield, epifluorescent microscopes.
2. Probes must remain fluorescent under continuous illumination for >20 seconds
3. Probes must demonstrate the localization of a model RNA
4. The amount of protein produced from mRNA in cells labeled with probe must remain unchanged from that in control cells.

To assess the detectability of probes in widefield fluorescence microscopy, probes were first deposited onto glass substrates and imaged using an inverted microscope with a

63x/NA 1.4 objective and a cooled CCD camera. Imaging probes on glass offered a simplified system of quantification that allows for comparison of several critical design elements including fluorophore selection and homo-oligomerization approaches. The microscopy method selected was chosen to recapitulate what one may find in standard imaging cores and in individual research labs. To determine whether or not single probes can be detected, probes composed of ligands labeled with one of two spectrally distinct fluorophores were individually labeled and deposited onto the glass substrate. In this situated there are several possible results:

1. no signal is detected above the background
2. uniform signal is detected throughout the imaging field
3. uniform, distinct puncta of separate "colors" are detected over a background
4. non-uniform, distinct puncta of separate "colors" are detected over a background
5. puncta composed of both "colors" are detected over background

In case 1, it can be concluded that the individual probes are not detectable using this imaging modality and the probes must be made brighter. In case 2 too many probes are adsorbed to spatially distinguish individuals and a lower concentration must be used. In case 3, the first probe criterion is satisfied and individual probes can be detected using our imaging modality. In case 4 it is likely probe labeled with the same fluorophores are aggregating. In case 5, probes containing both fluorophores are aggregating.

After the probes were confirmed to be single-molecule sensitive *in vitro*, it was necessary to deliver them into cells and determine if individual probes are still detectable.

Two possible complications may have arisen due to the nature of live cell delivery. First, probes may have lost fluorescence intensity due to the different chemical environment of the cytosol. Second, probes may have aggregated either non-specifically in organelles, or probes may have been actively sequestered by the cell. To test these cases untargeted probe were delivered into the cytoplasm of cells and imaged after fixation. Probe distribution and intensity histograms were assessed to determine if individual probes are detectable or if they aggregate, and the colocalization of probes with endosomal markers was determined.

To characterize probe sensitivity we immobilized probes targeting the genomic RNA of the wild-type strain A2 of human respiratory syncytial virus (hRSV) on glass surfaces by adding them in growth media to a coverslip well and incubating them for 10minutes at 37 °C. The mixture was removed, growth medium was added, and the glass surface was imaged. Individual batches of each probe **Figure 2.2**, in addition to a mixture of Cy3B and ATTO 647N labeled probes **Figure 2.2**, were imaged on the glass surface. Individual probes were identified, and the mean intensity within the diffraction limited spots was plotted as a histogram **Figure 2.2**. From the images of the probe mixtures, the histograms of each probe, and three-dimensional plots of the intensity of individual probes **Figure 2.2**, it is clear that the images represented detect single probes and not aggregates. If the probes were aggregating, the histograms would show non-unimodal behavior and mixtures of different color probes would co-localize, which was not the case.

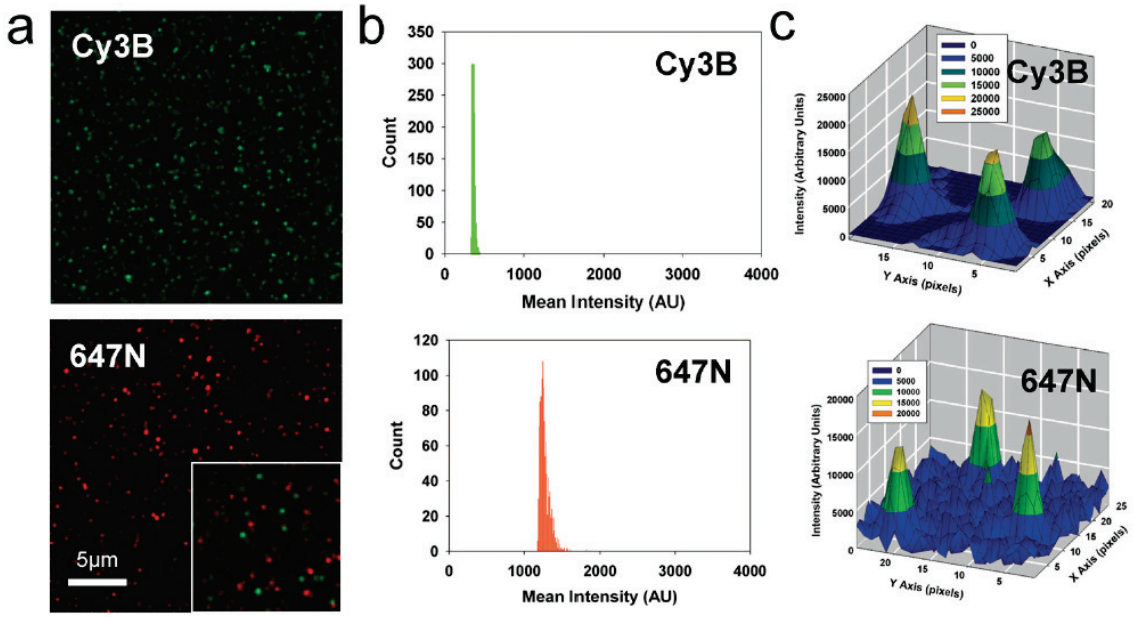

Figure 2.2: Images of single MTRIPs on glass surface. (a) Images of single Cy3B and Atto 647N probes, respectively, at 2 nM. (Inset depicts image of a mixture of Cy3B and Atto 647N MTRIPs demonstrating probe independence.) (b) Histograms of the mean intensity within each diffraction-limited spot constructed from 750-1000 detected probes. The unimodal histograms and (c) three-dimensional intensity profiles of representative probes post-deconvolution, additionally demonstrate that single probes were imaged.

Delivery Testing

We first characterized the distribution of untargeted probes in live cells by delivering hRSV targeting probes labeled with Cy3B (GE Healthcare) and Atto 647N (Atto-Tec GmbH) at low (2nM) concentrations into non-infected A549 cells. The low concentration was used such that individual probes would be present as distinct granules resolvable in the microscope. From a single optical plane within the live cell, we observed individual probes, labeled with Cy3B, to be homogenously distributed in the cytoplasm **Figure 2.1** and did not observe localization or accumulation of probes in the nucleus or mitochondria. Similar results were obtained with Atto 647M labeled probes (data not shown). These experiments suggest that even at low concentrations, the MTRIPs do not aggregate and are able to be delivered to the entire cytoplasm without aberrant accumulation in the nucleus.

Materials and Methods

The 2′ *O*-methyl RNA-DNA chimera nucleic acid ligands were synthesized by Biosearch Technologies, Inc. Each contains a 5′ biotin modification and multiple dT-C6-NH_2, modifications. The streptavidin used for the core was purchased from Pierce. Probes were assembled by first labeling the free amine groups on the ligands with either Cy3B–NHS ester (GE Healthcare) or Atto 647N–NHS ester (Atto-Tec GmbH) using manufacturers' protocols. Free dye was removed using both Nanosep spin columns (Pall Corp.), illustra G-25 size-exclusion columns (GE Healthcare), or 3 kDa kDa molecular weight cut off (MWCO) amicon columns (Millipore). The purified ligands were resuspended in 1× phosphate-buffered saline (PBS; pH 7.4) and mixed at a 10:1 molar ratio with

streptavidin for 1 h at room temperature (18–22 °C). Free ligands were removed using 30 kDa MWCO Nanosep spin columns, or 30 kDa MWCO amicon columns, and stored at 1 μM final concentration in 1× PBS at 4 °C. When multiple probes were used, each probe was completely assembled and filtered separately, and then mixed with equimolar concentrations in streptolysin O and medium just before delivery into cells We estimated the cost of MTRIPs, based on 30 nM delivery concentration, to be $0.15 per well, for a 24-well plate.

Characterization of MTRIPs targeting β-actin mRNA. Single plane images showing U2OS cells treated with SLO without (A) or with (B) MTRIPS targeting β-actin mRNA, imaged at the same exposure time (126 ms) and with similar contrast enhancement. In order to test MTRIPs specificity, MTRIPS targeting β-actin mRNA (C, red) or the genomic RSV RNA (D, green) were delivered at the same concentration (30 nM). The merged image in E demonstrates no colocalization between targeted and "scrambled" probes. Nuclei were stained with DAPI. Scale bars, 10 μm.

MTRIPs do not affect target mRNA stability and translatability. (A) mRNA decay in cells treated with SLO without or with MTRIPs was assayed upon treatment with Actynomicin D after 0, 4, 8 and 24 h as described in the text via qRT-PCR. β-actin mRNA expression fold change is normalized to GAPDH. (B) Percentage of cells expressing GFP-β-actin in control cells and in the presence of 50 nM or 200 nM siRNA or 30 nM MTRIPs. Error bars indicate standard deviation and * represents statistically significant difference ($P<0.05$).

SLO treatment does not alter SG/PB formation and/or protein composition.

Untreated U2OS cells (A) or treated with SLO (B) formed SGs that contain endogenous HuR, G3BP and TIAR proteins after treatment with 0.5 mM sodium arsenite for 1 h at 37°C. Scale bars, 10 μm. (C) Average number of SGs per cell observed upon sodium arsenite treatment with and without SLO. (D) Average number of PBs per cell in untreated (-) and treated cells (As) with and without SLO. Error bars indicate standard deviation and * represents statistically significant difference ($P<0.05$).

Fluorescence imaging.

Immobilized Cy3B and Atto 647N probes on the glass surface were imaged using a Zeiss Axiovert 200M microscope with an ×63, NA = 1.4 Plan-Apochromat objective, using Chroma 49004 ET-Cy3 and 49006 ET-Cy5 filter sets, with 500-ms exposures. An EXFO excite 120 light source with a ND (neutral density) = 0.4 (40% transmission) was used for fluorescence excitation, and a Hamamatsu ORCA-ER AG for taking digital images. Live-cell images of single probes within A549 cells were taken with 350 ms exposures under the same illumination conditions. *Z*-dimension stacks were taken in both cases, in 200-nm steps, and deconvolved using Volocity iterative deconvolution algorithm. Cells used in the human β-actin mRNA-scrambled probe experiments were fixed after live-cell hybridization and imaged similarly to the immobilized probes, but with 200-ms exposures and deconvolved in Volocity. Time-lapse live cell images were taken as discussed above, and were processed with Volocity's 2D or fast deconvolution algorithm. In the stress granule control experiments, live cell images were taken similarly to the single probe images but with 50-ms exposures. hRSV after-delivery, fixed-cell control experiments were imaged with a Zeiss LSM 510 Meta using an ×63, NA = 1.4, Plan-

Apochromat objective. All images were taken using multi-track scanning for each fluorophore to prevent bleed-through. *Z*-dimension stacks were taken in 0.5-µm increments; the 543 nm laser (Cy3B probe) was set at 25% power, the 488 nm laser (for N protein immunostaining) was set at 37%, and the pinholes were set to an airy unit of 1 (equal to airy disk). β-actin mRNA, actin-related protein 2 homolog mRNA and ZBP1, in the chicken embryonic fibroblasts, were imaged under similar conditions to the human β-actin mRNA experiments.

References

Fusco, D., N. Accornero, et al. (2003). "Single mRNA molecules demonstrate probabilistic movement in living mammalian cells." Curr Biol **13**(2): 161-167.

Molenaar, C., S. A. Marras, et al. (2001). "Linear 2' O-Methyl RNA probes for the visualization of RNA in living cells." Nucleic Acids Res **29**(17): E89-89.

Ozawa, T., Y. Natori, et al. (2007). "Imaging dynamics of endogenous mitochondrial RNA in single living cells." Nat Methods **4**(5): 413-419.

Politz, J. C., E. S. Browne, et al. (1998). "Intranuclear diffusion and hybridization state of oligonucleotides measured by fluorescence correlation spectroscopy in living cells." Proc Natl Acad Sci U S A **95**(11): 6043-6048.

Politz, J. C., K. L. Taneja, et al. (1995). "Characterization of hybridization between synthetic oligodeoxynucleotides and RNA in living cells." Nucleic Acids Res **23**(24): 4946-4953.

Rhee, W. J. and G. Bao (2010). "Slow non-specific accumulation of 2'-deoxy and 2'-O-methyl oligonucleotide probes at mitochondria in live cells." Nucleic Acids Res **38**(9): e109.

Shav-Tal, Y., X. Darzacq, et al. (2004). "Dynamics of single mRNPs in nuclei of living cells." Science **304**(5678): 1797-1800.

Tyagi, S. and O. Alsmadi (2004). "Imaging native beta-actin mRNA in motile fibroblasts." Biophys J **87**(6): 4153-4162.

Vargas, D. Y., A. Raj, et al. (2005). "Mechanism of mRNA transport in the nucleus." Proc Natl Acad Sci U S A **102**(47): 17008-17013.

CHAPTER 3

BETA ACTIN MRNA TARGETING

Background

Despite the importance of mRNA in the regulation of gene expression, there have been few studies thoroughly characterizing the transport of mRNA in live cell systems. Moreover, many of the studies to date contain conflicting conclusions as to the nature of mRNA transport mechanisms. One reason for this may be that few model systems exist upon which to develop and test new methods of studying RNA transport. Despite this, the transport of β-actin mRNA is one of the most studied systems and will therefore serve as the test case for validating MTRIPs and demonstrating the utility of MTRIPs to further the research in this field. Additionally, current methods for studying mRNA movement have focused on expression of an engineered mRNA and not on native transcripts which may influence the results of the experiments performed thus far.

To date few studies have been published on imaging the dynamics of RNA in live cells and none have verified this data against native RNA dynamics. The ability to image native RNAs will be useful in and of itself and, when combined with plasmid based systems, may allow for even more methodological flexibility as cis-acting elements in expression systems can be easily modified.

In addition to demonstrating the validity and utility of MTRIPs in the study of RNA dynamics, this study will bridge the gap between previous works, which analyzed the dynamics of β-actin mRNA at disparate time scales in different model systems.

Where previous studies have forced mRNA dynamics data into models developed for small molecule diffusion and membrane protein dynamics, we hope to define a new model for mRNA dynamics that describes the phenomena seen in this study and explains the discordance of results from others.

The β-actin mRNA model system will be employed as there have been several studies of this model system using various technologies including MS2-GFP for live cell studies, and in situ hybridization for fixed cell studies. MTRIPs will be designed to target coding and non-coding regions of the RNA. Non-coding sites will be designed to avoid binding to known RNA binding proteins binding sites specifically HuR and ZBP1.

MTRIPs, when delivered via reversible cell membrane permiabilization (Santangelo and Bao 2007) with streptolysin O **Figure 2.1**, allowed for single RNA molecule sensitivity using conventional fluorescence microscopy techniques. We identified the target RNA by the enhanced signal-to-background ratio achieved through the binding of multiple MTRIPs per RNA (two or three), via Watson-Crick base pairing (Vargas, Raj et al. 2005; Utley, Ducharme et al. 2008), or if using a single MTRIP per RNA, through the natural localization of RNA **Figure 2.1**. This is analogous to the MS2-GFP binding systems, but uses native target sequences and fewer binding sites.

Probe Delivery and signal discrimination

As an initial test of the ability to image single RNAs, we simultaneously delivered two Cy3B-labeled MTRIPs designed to target two regions of the human β-actin mRNA coding sequence (human β-actin mRNA probes 1 and 2; **Table 3.1**) and an Atto 647N–labeled 'scrambled' probe (no target in human genome) (30 nM each) using streptolysin O

into A549 cells. Twenty minutes after delivery, we fixed the cells in 4% paraformaldehyde and imaged them. We could image individual RNAs in both fixed and live cells, but we fixed the cells for quantification because of the dynamic nature of RNA granules as moving RNAs may have caused the granule count to be artifactually high. For β-actin, we observed individual 'unbound' probes as well as localized granules with twice the intensity **Figure 3.1**. It was assumed that granules with twice the intensity represented mRNAs with both targeting probes bound to them. Although it is possible that mRNAs may have been bund only by one probe; this criterion was used as an initial threshold. The use of more target sequences could further increase the likelihood that mRNA granules could be reliably distinguished from free probe. β-actin mRNA signal was prevalent in the perinuclear region of the cell and also localized to the leading edges, as had previously been described. This is in contrast to the 'scrambled' probe produced perinuclear signals and localized not at the cell periphery throughout in the cytoplasm, demonstrating β-actin probe specificity. This non-colocalization between an untargeted probe and the β-actin targeting probe served to demonstrate that the MTRIPs do not non-specifically aggregate inside of living cells as they would show strong colocalization if they did. We quantified localization in an intensity profile of the confocal image **Figure 3.1**. This figure demonstrated, in another visualized form, that the signal from the targeted and untargeted probes do not colocalize nor do the changes in signal intensity correlate in space. From the lower-noise, widefield-deconvolved image **Figure 3.1** we removed via thresholding the average single-probe intensities, quantified from probes on the glass surface, and counted the remaining granules using Volocity software. Using this approach we observed single β-actin mRNAs, containing approximately twice the single

probe intensity, in the cell **Figure 3.1** and detected a total of 1,455 granules. Granule mean fluorescence intensity (calculated from the three-dimensional reconstruction) had a measured s.d. of only 25% of the mean, reflecting the uniformity of the granules when measured in three dimensions. The granule count was consistent with previous quantifications (~1,500 in serum-stimulated cells), using a similar analysis for β-actin mRNA in epithelial cells (Femino, Fay et al. 1998).

Table 3.1 Ligands for MTRIPs used to target RNA in living cells.

RNA target	**Ligand**	**Accession Number & Location within gene**
hRSV genomic RNA	5′-biotin-**U**XTXTTX**AAAAAXGGGGCAAAXAA**-3′	M74568; 39-55;590-606;2323-2339
Human β-actin mRNA		NM_001101.2
Probe 1	5′-biotin-**U**XTTTX**AXAGCACAGCCXGGAXA**-3′	494-478
Probe 2	5′-biotin- TTTTTTX**AUUXCCCGCXCGGCCGXG**-3′	696-679
Chicken β-actin mRNA		NM_205518 XM_429312
Probe 1	5′-biotin-TTTTTX**GGAGXAACGCGGXCAGXCAG**-3′	57-38 (61-38 Tyagi, 2004)
Probe 2	5′-biotin-TTXTTT**CAAXAUCAXCAUCCAXGGC**-3′	84-66 (83-66 Tyagi, 2004)
Probe 3	5′-biotin-TTTTTX**AGGAXACCXCUUXUGCUCXGG**-3′	262-242 (262-240 Tyagi, 2004)
Chicken arp2 mRNA		NM_205224
Probe 1	5′-biotin-TTTTXT**TUCCXCCCCAGCGXGUCCA**-3′	130-112
Probe 2	5′-biotin-TTTTTX**ACCAAGCXTCXCCAGCACA**C-3′	1280-1261
Probe 3	5′-biotin-TTTXTT**CAGXUGAXCUTAXAAUAGG**-3′	243-225
Scrambled probe		
	Boldface: 2′-O-Methyl RNA; X: dT-C6-NH2; all others are DNA; underline: binding region	

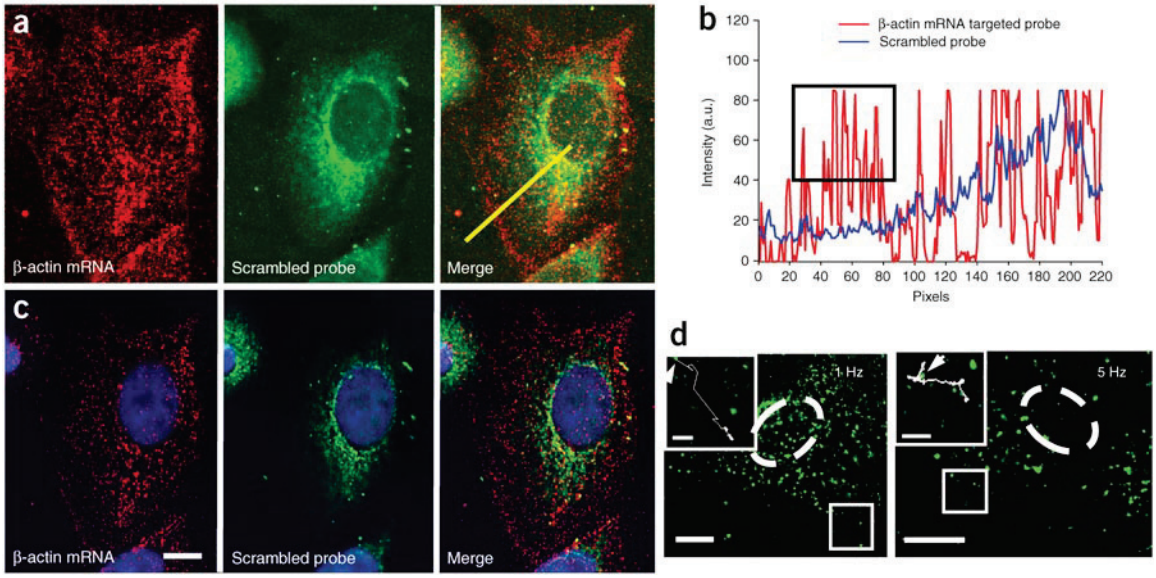

Figure 3.1: β-actin mRNA targeting in A549 cells. (a) actin mRNA and 'scrambled' probe imaged with a laser scanning confocal microscope with all image planes represented. Merge images are also shown. (b) Intensity profiles along the yellow line in a. The black box highlights the large numbers of -actin mRNA individual granules at the cell periphery detected by the targeted probe, but not by the scrambled probe. (c) Single optical plane of the same cell as in a resulting from widefield-deconvolution imaging. Scale bar, 5 m. (d) Single optical plane of two living A549 cells (nucleus denoted with dashed line) imaged at 1 Hz for 3 min and 5 Hz for 30 s, respectively. Inset, images of boxed regions, including traces of -actin mRNA granule trajectories for 70 s (1 Hz) and 30 s (5 Hz). Starting points are denoted by arrows. Scale bars, 10 m (3 m in insets).

The use of two MTRIPs was both feasible as a strategy of labeling and tracking mRNAs in the cytoplasm of live cells; however, an extension of this technique to a larger number of probes had several advantages. Using a larger number of probes provided for longer imaging time durations, a faster sampling rate, and easier discrimination between free and bound probes. In order to increase the observation time and avoid overlooking the contribution of different transport mechanisms due to temporal under-sampling, we designed additional MTRIPs targeting distinct sequences in both the coding region and 3' UTR of native β-actin mRNAs **Table 3.1**. 3' UTR probes were designed to avoid binding to the ZBP1, HuR, and TIA-1 binding sites (Kislauskis, Zhu et al. 1994; Lopez de Silanes, Zhan et al. 2004; Lopez de Silanes, Galban et al. 2005). Probes were delivered into live cells via streptolysin-O (SLO) reversible permeabilization as before (Barry, Gesek et al. 1993; Bhakdi, Weller et al. 1993; Paillasson, Van De Corput et al. 1997; Giles, Spiller et al. 1998; Spiller, Giles et al. 1998; Clark, Grzybowski et al. 1999; Walev, Bhakdi et al. 2001; Santangelo, Nix et al. 2004; Santangelo, Nitin et al. 2005; Abe and Kool 2006; Santangelo, Nitin et al. 2006; Santangelo and Bao 2007; Rhee, Santangelo et al. 2008; Utley, Ducharme et al. 2008; Santangelo, Lifland et al. 2009). After recovery in complete growth medium, plasma membrane integrity was tested using an ethidium bromide exclusion assay. A small increase (2% to 6%) in ethidium bromide stained cells was observed in mock cells (no treatment) and in cells after SLO-mediated delivery of probe, while cells treated with triton X-100 showed 100% permeabilization (data not shown). This confirmed earlier results using ethidium homodimer and calcein AM assays, and propidium iodide exclusion that suggested near complete recovery of membrane integrity after the recovery phase (Paillasson, Van De Corput et al. 1997;

Santangelo, Lifland et al. 2009). To exclude the possibility that the additional probes were cross linking individual mRNAs into aggregates, we quantified the number of mRNA granules when 6 non-tetramerized ligands, and 2 or 6 MTRIP probes (probe sequences 1-6 in **Table 3.2**) were delivered into cells **Figure 3.2**. For the 2 MTRIP case, only probe sequences 1 and 2 **Table 3.2** were used. Owing to the small diameter of the tetramerized probes (~5 nm) if crosslinking of mRNA were occurring, it would result in the reduction of the number of apparent granules, since the resulting mRNA granules would be closer together than the resolvable limit of the microscope (~250 nm). No significant difference ($p>0.5$ by Kruskal–Wallis analysis of variance) was observed in the number of mRNA granules in the three experimental conditions, indicating that aggregation of mRNAs does not occur **Figure 3.2**. Comparison between experiments performed with 6 linear probes, 2 MTRIPs and 6 MTRIPs showed that MTRIPs were consistently brighter than linear probes and the additional MTRIPs demonstrated an approximately two fold increase in the fluorescence intensity of detected native mRNA granules ($p<0.05$) **Figure 3.2**. While it was initially expected that the increase in signal would be linear with respect to the number of fluorophores, several mechanisms may be at play that made the data deviate from this ideal situation; however, the most likely explanation was that not all of the additional target sequences may be available for binding. This would explain the lower intensity of the 6 linear and 6 MTRIP cases when compared with the 2 MTRIP case. This increase in intensity, along with the constant number of granules detected suggests that MTRIPs are specifically labeling β-actin mRNA granules and not non-specifically aggregating in the cell. As an initial demonstration of the additional capabilities possessed by this extended technique, we

demonstrated that the use of 6 MTRIPs allowed for an acquisition frame rate of 5 Hz and imaging time of over 5 minutes, considerably longer than imaging durations of previous single molecule sensitive mRNA tracking studies which imaged RNAs for 0.3 s, 22 s, and 60 s (Fusco, Accornero et al. 2003; Vargas, Raj et al. 2005; Ben-Ari, Brody et al. 2010). A fast acquisition rate was chosen such that, frame-to-frame, mRNA granules moving at 1 μm/s would not move further than the resolution limit of the microscope (~250nm). Additionally, no change in the mRNA distribution was apparent when either linear or tetramerized probes were used **Figure 3.2**.

Table 3.2 β-actin mRNA targeting probe sequences and modifications.

Human β-actin mRNA target	**Ligand**	**Location within transcript**
Probe 1	5′-biotin-TXTTTX**AXAGCACAGCCXGGAXA**-3'	494-478
Probe 2	5′-biotin- TTTTTTX**AUUXCCCGCXCGGCCGXG**-3'	696-679
Probe 3	5′-biotin-TXTTTT**XUCCUGXAACAAXGCAUCXC**-3'	1479-1461
Probe 4	5′-biotin-TXTTTTX**AAGCCCXGGCXGCCXCCA**-3′	1748-1730
Probe 5	5′-biotin-TTTTTX**GUXCAAXGGGGXACUUCA**GGGX-3′	290-269
Probe 6	5′-biotin-TTTTTX**GCCAGX**GGX**ACGACCAGAGGCAX**-3'	524-501
Probe 7	5′-biotin-TXTTTT**GXCACCUXCACCGUXCCAG**-3'	1377 1359
	Boldface: 2′-O-Methyl RNA; X: dT-C6-NH2; all others are DNA; underline: binding region	

We also characterized the distribution of native mRNA granules in untreated U2OS cells by delivering, using streptolysin O (SLO), Cy3B-labeled MTRIPs designed to target either the polyA+ tail of mRNAs or two regions of the human β-actin coding sequence (poly A+ probe 90 nM or ACTB probes 1 and 2, 30 nM each, **Figure 3.3** and **Table 3.3**). After delivery, the cells were fixed and various proteins were fluorescently-labeled using immunostaining. Both mRNA populations were found to be distributed in diffraction-limited spots or granules within the cytoplasm, clearly visible in comparison to background noise **Figure 3.4**; as previously shown, β-actin mRNA were abundant in the perinuclear region, in protrusions and along the edges of the cells (Figure 1B and S1B) (Santangelo, Lifland et al. 2009), while poly A+ mRNAs appeared to be relatively more abundant in the perinuclear region **Figure 3.3**. To further demonstrate MTRIPS specificity we delivered via SLO, simultaneously, probes targeting β-actin mRNA, and a "scrambled" probe, which targets the genomic RNA of respiratory syncytial virus (RSV) at the same concentration, but labeled with a Cy5 equivalent dye, CF640R (Biotium, Inc.) **Table 3.3** As previously demonstrated (Santangelo, Lifland et al. 2009), the latter were distributed in the perinuclear region and in the cytoplasm and did not colocalize with β-actin mRNA **Figure 3.4**.

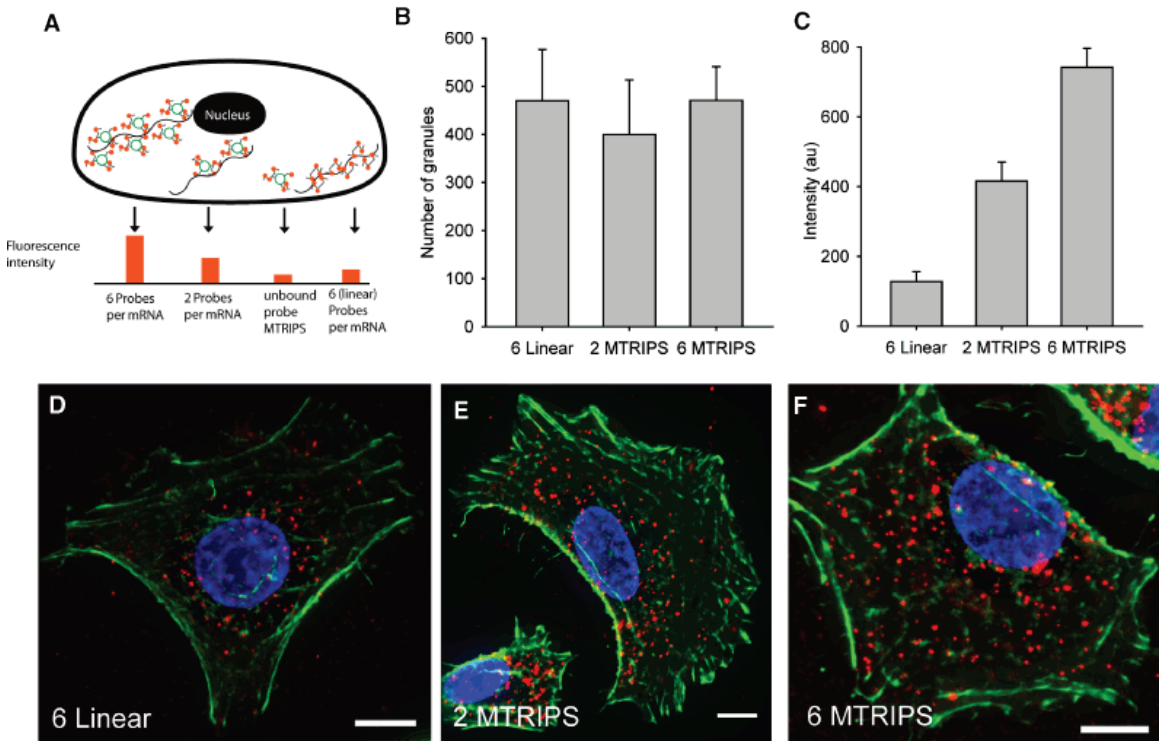

Figure 3.2. **mRNA targeting by MTRIPs.** A) Schematic representation of the detection method showing expected fluorescence intensity when six or two MTRIPs, or six linear probes target β-actin mRNA molecules and comparison with an unbound MTRIP probe. B) Quantification of the average number of mRNA granules detected using six linear probes and two or six MTRIPs, demonstrating that MTRIPs do not aggregate mRNAs. C) Average fluorescence intensity when β-actin mRNA is targeted by two or six MTRIPs or six linear probes. Extended view of β-actin mRNAs targeted by six linear probes (D), two and six MTRIPs (E and F) (red) demonstrating the typical distribution of β-actin mRNA. Nuclei were stained with DAPI (blue) and the actin fibers were stained with phalloidin (green). Scale bars are 10 μm.

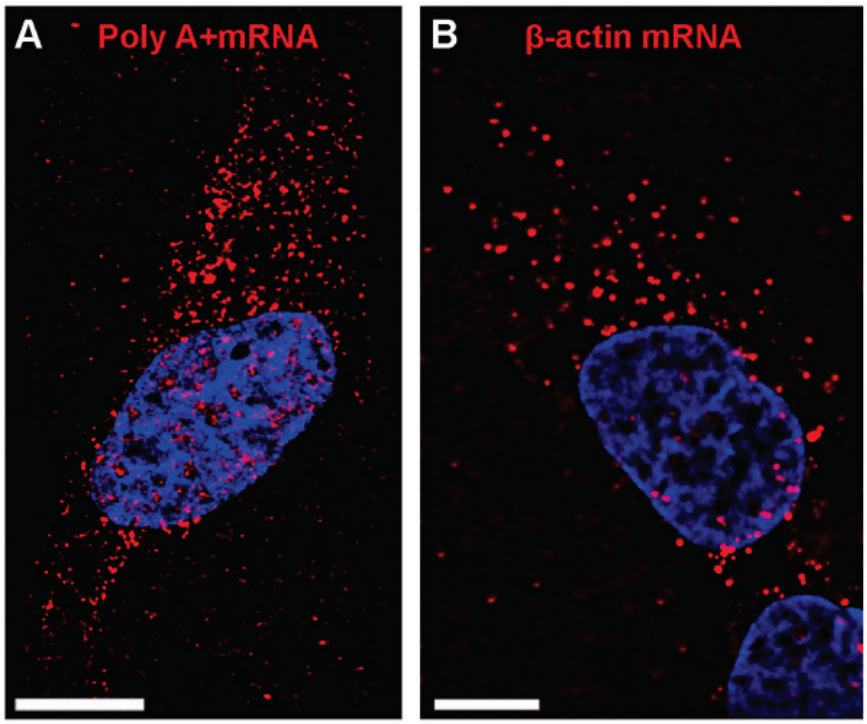

Figure 3.3 polyA+ and β-actin mRNA distribution. Single plane images showing the distribution of (A) poly A+ and (B) β-actin mRNA granules (red) in controlU2OS cells. Nuclei were stained with DAPI. Scale bars, 10 μm.

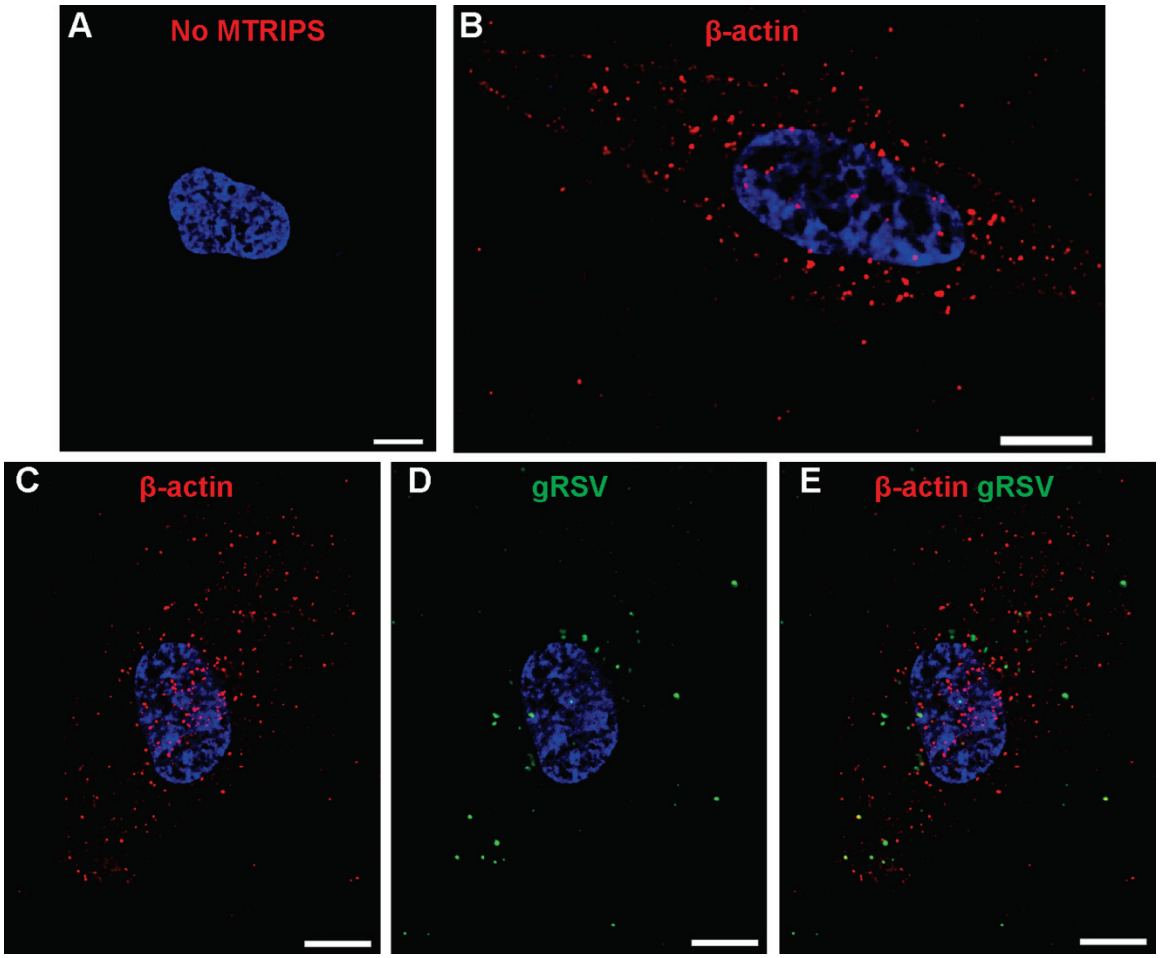

Figure 3.4 Characterization of MTRIPs targeting β-actin mRNA. Single plane images showing U2OS cells treated with SLO without (A) or with (B) MTRIPS targeting β-actin mRNA, imaged at the same exposure time (126 ms) and with similar contrast enhancement. In order to test MTRIPs specificity, MTRIPS targeting β-actin mRNA (C, red) or the genomic RSV RNA (D, green) were delivered at the same concentration (30 nM). The merged image in E demonstrates no colocalization between targeted and "scrambled" probes. Nuclei were stained with DAPI. Scale bars, 10 μm.

Demonstration of non-endocytic delivery and non-endocytic sequestration

While granule counts and fluorescence intensity offered substantial evidence that the probes were binding to the target mRNA, the possibility that the probes entered the cell by endocytosis or were sequestered in endosomes during the experiments could not directly be excluded. In order to test this hypothesis cells were fixed 15 min and 2 hrs post delivery of MTRIPs and immunostained for early endosomal antigen 1 (EEA1), cluster of differentiation 63 (CD63) and lysosome associated membrane protein 1 (LAMP1), markers for early endosomes, late endosomes, and lysosomes respectively **Figure 3.5**. These results were compared to those observed in a similar experimental setup using fluorescently labeled Neutravidin conjugated with the TAT peptide (NA-TAT), whose uptake was previously shown to depend on endocytosis (Rinne, Albarran et al. 2007). NA-TAT was shown to colocalize with all three endosomal markers after 2 hrs of incubation both by visual inspection and by Manders' overlap and Pearson's coefficients calculated on the reconstructed voxel (3D) data, confirming entry by an endocytic mechanism **Figure 3.5**. These data are in good agreement with previous reports of low colocalization with endocytic proteins at early time points and a high degree of colocalization at later time points (Rinne, Albarran et al. 2007). In contrast, the low Manders' overlap and Pearson's coefficients exhibited by MTRIPs at the same time points demonstrated they do not colocalize with endosomal markers **Figure 3.5** confirming that SLO-mediated MTRIP entry does not proceed through the endocytic pathway nor are probes sequestered in endosomes while the experiments were performed. To statistically confirm that there is a significant difference between MTRIP delivery and endosomal uptake, an ANOVA on ranks was performed, pairing Pearson's and Manders' coefficients

at the 2 hr time point for MTRIP delivery and NA-TAT incubation. All pairs were confirmed to be statistically significant ($p<0.05$). These data also suggest that the time duration of deliver of MTRIPs, approximately 10 min, would have been too short to result in significant endocytosis of probes as the NA-TAT was not endocytosed during that time frame

Table 3.3: Sequences of MTRIPs targeting β-actin mRNA (ACTB) and the polyA tail with location within transcript.

Human β-actin mRNA target	**Ligand**	**Location within transcript**
PolyA+ Probe	5′-biotin-TXTTTT**UXUUUUUUXUUUUUUXUU**-3’	
ACTB Probe 1	5′-biotin-TXTTTX**AXAGCACAGCCXGGAXA**-3′	494-478
ACTB Probe 2	5′-biotin- TTTTTTX**AUUXCCCGCXCGGCCGXG**-3′	696-679
ACTB Probe 3	5′-biotin-TXTTTT**XUCCUGXAACAAXGCAUC**XC-3′	1479-1461
ACTB Probe 4	5′-biotin-TXTTTTX**AAGCCCXGGCXGCCXCCA**-3′	1748-1730
ACTB Probe 5	5′-biotin-TTTTTX**GUXCAAXGGGGXACUUCA**GGGX-3′	290-269
ACTB Probe 6	5′-biotin-TTTTTX**GCCAGX**GGX**ACGACCA**GA**GGCAX**-3′	524-501
hRSV Probe	5′-biotin-**U**XTXTTX**AAAAAXGGGGCAAAXAA**-3′	39-55;590-606;2323-2339
	Boldface: 2′-O-Methyl RNA; X: dT-C6-NH_2; all others are DNA; underline: binding region	

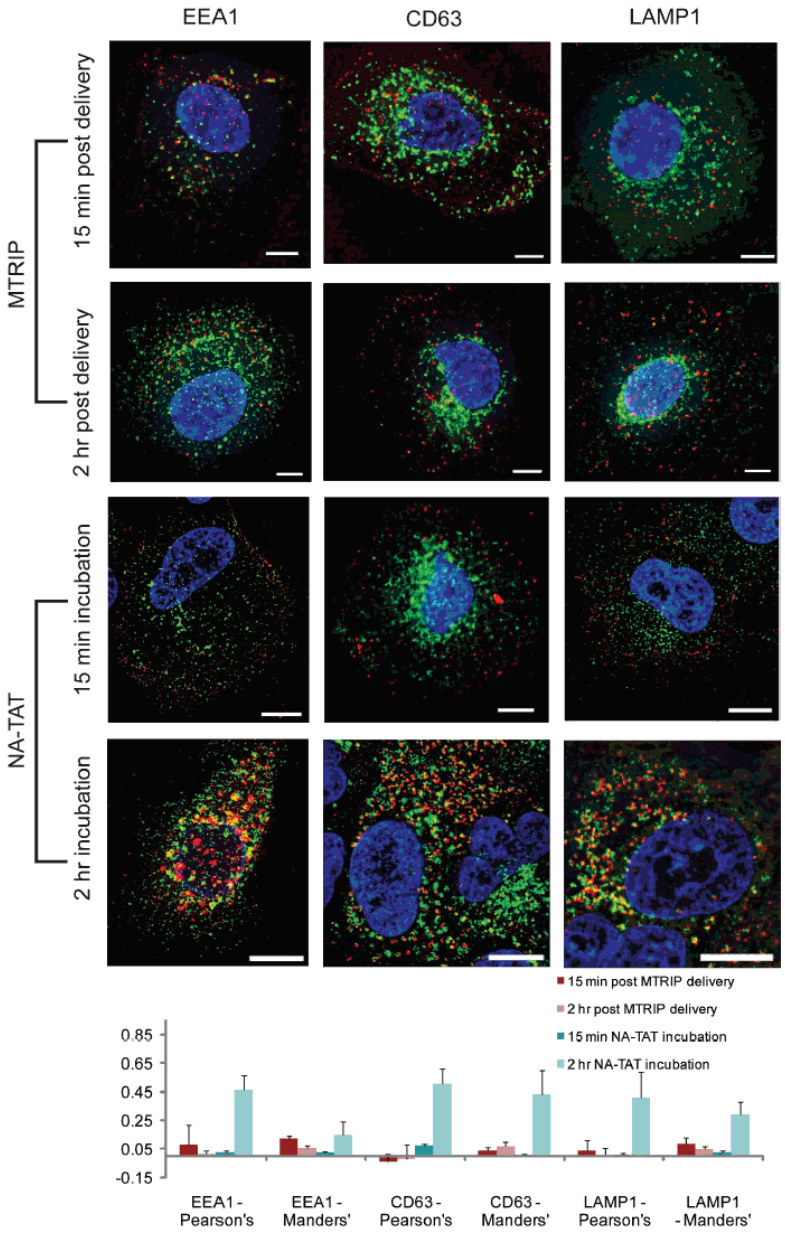

Figure 3.5 β-actin mRNA granules do not colocalize with endosomal markers. Single plane images of β-actin mRNA (top 2 rows) or Neutravidin-TAT (NA-TAT)(bottom 2 rows) (red) distribution in A549 cells fixed and stained for EEA1, CD63 and LAMP 1 (green) at 15 min and 2 hr after probe delivery or after 15 min and 2 hr of incubation with NA-TAT. Nuclei are stained with DAPI (blue). Bar graphs show Pearson's and Manders' overlap coefficients generated from 3D deconvolved images. Scale bars are 10 μm. Error bars are standard deviation.

Molecular specificity

Molecular specificity was tested by several independent tests both utilizing imaging and standard molecular biology approaches. In the first set of experiments the number of granules detected using MTRIPs was quantified under different conditions. To demonstrate that the granule number is associated with the copy number of mRNA we needed to establish the following criteria.

1. Increasing the number MTRIPs used will not increase the number of granules detected.
2. Increasing the number of MTRIPS used will increase the brightness of individual granules
3. Decreasing the copy number of mRNAs will decrease the granules count

In order to determine if MTRIPs meet the first two criteria, MTRIPs targeting a subset of sequences and a larger number of sequences was delivered into cells, and the number of detected granules was quantified. Within those granules the fluorescence intensity was calculated. To determine if MTRIPs meet the third criterion siRNA was used to specifically reduce the copy number of β-actin mRNA and the number of granules detected using MTRIPs was quantified for both the targeted and control siRNA. RT-PCR was used as a gold standard to confirm knockdown.

In the second set of experiments, the localization of mRNA detected using MTRIPs was assessed by comparison with fluorescence in situ hybridization and with immunostaining for known RNA binding proteins.

Verification by simultaneous FISH

Previous experiments have demonstrated the likelihood that the MTRIPs are binding to their target RNAs. However, there remained a question of whether or not the MTRIPS were binding to a representative RNA population. For instance, owing to the fact that the probes were delivered into live cells, trans acting factors, such as ribobsomes or RNA binding proteins, may have been preventing the probes from binding to the target sequences and therefore the granules identified would have been biased to those that were translationally repressed, or those in a subset of RNA transport granules. To demonstrate that the use of MTRIPs to target mRNAs does not bias our data to a subset of transcripts, β-actin mRNAs were simultaneously detected using MTRIPs delivered into live cells and, subsequently after fixation, using FISH as described in the material and methods section. FISH, because it involves the use of denaturing conditions, lessens the likelihood that target sites will be blocked and therefore was assumed to represent the ground truth for RNA localization. **Figure 3.6** shows the distribution of MTRIP probes and FISH staining in a representative A549 cell as well as their colocalization. Both probes prevailed throughout the cytoplasm in the perinuclear region and cell edge. Image intensity plots (**Figure 3.6 D and H**) demonstrated that MTRIP and FISH signals are coincident at the single granule level. These data are consistent with the hypothesis that MTRIPs are able to bind to representative mRNA and do not bias the imaging data to a subset of granules. Moreover, these data demonstrate that MTRIPs are compatible with in situ hybridization, and; therefore, this methodology can be used in future studies to confirm probe binding. Similarly, this experiment demonstrated that MTRIPs can be used in place of FISH, opening up important experiments that were previously untenable. Specifically, MTRIPs could be used simultaneously with immunostaining, which was

previously limited by the denaturing conditions of *in situ* hybridization or limited by the use of proteases which opened up binding sights hidden by fixation.

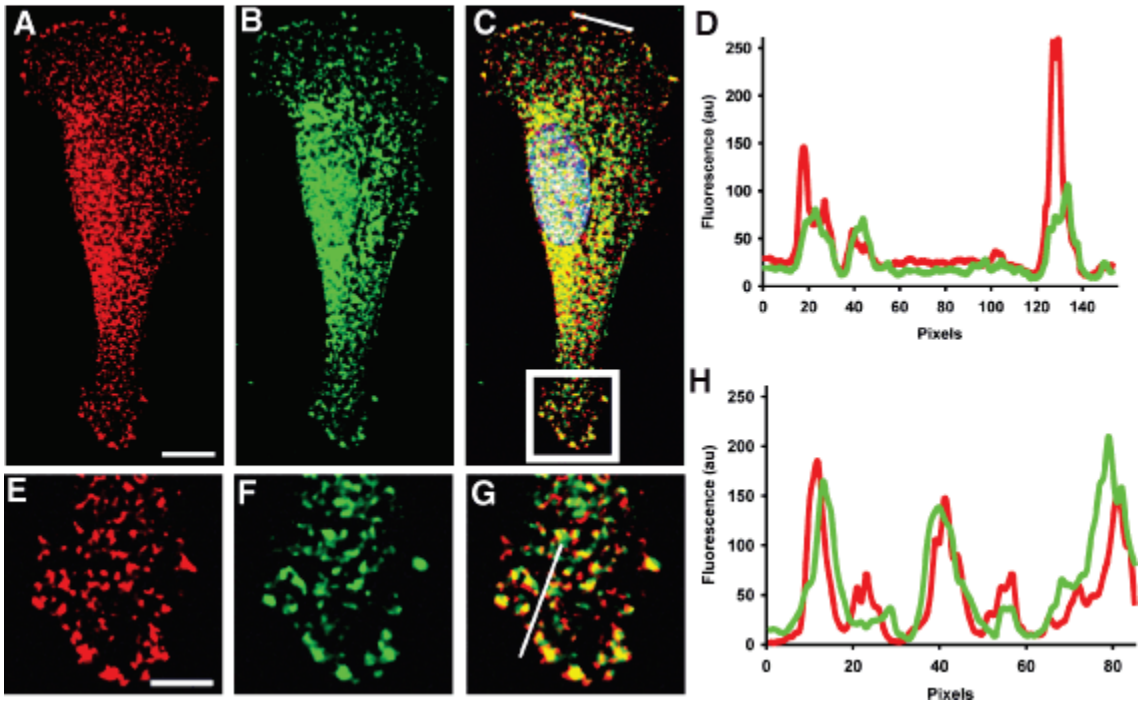

Figure 3.6: MTRIPs colocalize with FISH probes targeting β-actin mRNA and exhibit a similar subcellular distribution. MTRIPs labeled with Dylight 649 (B, green) were delivered into live A549 cells, which were subsequently fixed and stained for β-actin mRNA using Cy3B-labeled linear FISH probes (A, red). Colocalization of MTRIPs and FISH probes is demonstrated in the merged figure (C), where the magnification of a boxed region is shown in (E–G). Fluorescence intensity profiles in (D) and (H) show intensities along the white lines in (C) and (G), respectively, and demonstrate colocalization of probes at the single granule level. The nucleus is stained with DAPI (blue) and the image shown is a single deconvolved plane. Intensity profiles were generated from deconvolved images. Scale bars in (A) and (C) are 10 and 5 μm, respectively.

Verification by RNA interference

The previous experiments have demonstrated that the probes bind to RNA, are not sequestered into endosomes and do not bind to a subset of the RNA granules. However, it was important to demonstrate that the copy number obtained through granule counting was proportional to the copy number of mRNAs present. By doing so it could be concluded that the MTRIPs bound to mRNA in a molecularly specific manner and the signal from them could be assumed to be a surrogate for the mRNA itself. Without this verification, it would have been possible that MTRIPs bound nonspecifically to larger mRNA granule containing several different mRNAs, and this was responsible for the colocalization seen in the FISH data. To demonstrate the molecular specificity of MTRIPs in targeting native β-actin mRNA, siRNA against β-actin was used to specifically lower the transcript copy number. β-actin mRNA levels were assessed 48 hr post delivery, using either qRT-PCR or fluorescence imaging **Figure 3.7**. In the fluorescence imaging experiments, MTRIPs were delivered into cells 48 hr post siRNA delivery, fixed, and imaged. Cells were randomly selected and the number of mRNA granules counted using the automatic algorithms in Volocity with objects identified by the standard deviation intensity method. Both PCR and granule counting displayed a significant drop in β-actin mRNA upon siRNA delivery (90% and 80% respectively, $p>0.05$) when compared with control siRNA treated cells. Several factors may play a role in the discordance in the number of granules counted using MTRIPs compared with mRNA levels determined by RT-PCR including the presence of multiple mRNAs within individual granules, limitations in resolving and identifying diffraction limited objects, background from unbound probes and heterogeneity of the mRNA granules. Even with

these complications in counting mRNA granules, the extent of observed knockdown clearly demonstrates the specificity of MTRIPs targeting β-actin mRNA. One complication with using siRNA to lower the copy number of an mRNA is the off target effects of delivery or the siRNA itself. However, the non-targeted siRNA controlled for the delivery variable and the off target (TLRs and other PAMP receptors) effects.

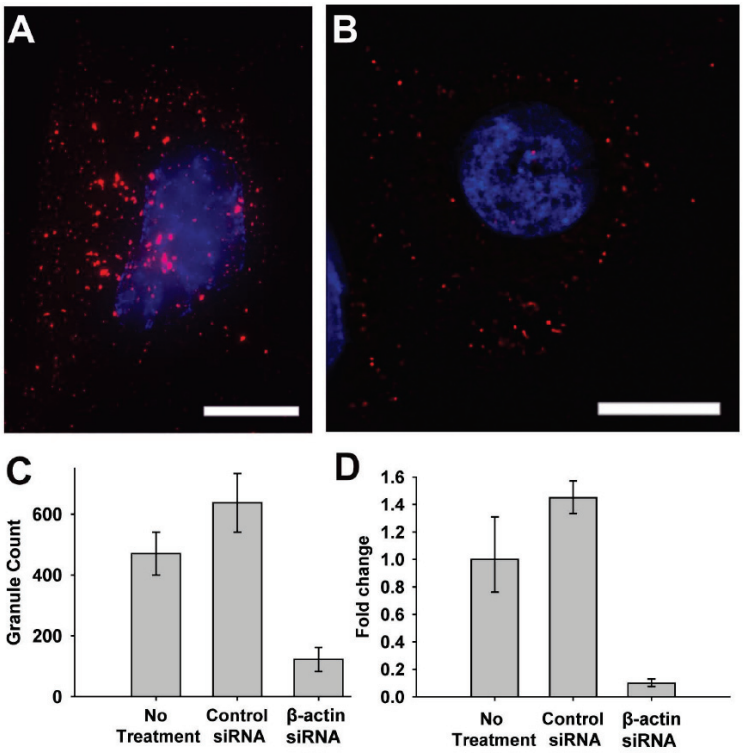

Figure 3.7: Decrease of the number of mRNA granules after treatement with β-actin siRNA. Image of β-actin mRNA targeted by MTRIPs in cells treated with control siRNA (A) or siRNA targeting β-actin (B). Nuclei are stained with DAPI. Scale bars are 10 μm. Images are extended views. (C) Quantification of the average number of mRNA granules per cell with no treatment, treatment with a control siRNA, and treatment with β-actin targeted siRNA. (D) Confirmation of β-actin mRNA levels by qRT-PCR. Error bars are standard deviation.

Verification by colocalization with known RNA binding proteins

As mentioned previously, one advantage MTRIPs have over FISH for imaging mRNA in fixed cells is that MTRIPs could be imaged simultaneously with immunofluorescence. This makes it possible to colocalize specific RNAs with RNA binding proteins and other cellular proteins such as cytoskeletal components. This property was exploited to further demonstrate that the signal from MTRIPs was likely to be due to binding to the target mRNA and not nonspecific aggregation. To to this we performed single-probe imaging of clustered RNAs and co-localized them with β-actin mRNA binding protein, ZBP1 (Ross, Oleynikov et al. 1997) in three dimensions **Figures 3.8 and 3.9**, and simultaneously imaged β-actin mRNA, actin-related protein 2 homolog mRNA and ZBP1 protein, in primary chicken embryonic fibroblasts **Figure 3.10**. Further evidence that these probes can be used to image native RNA was provided by targeting human β-actin mRNA in motile A549 cells. In this case, when targeting β-actin mRNA only one site, previously identified (Abe and Kool 2006), was used **Table 3.1**. β-actin mRNA, in motile cells, has been described to colocalize with the RNA binding protein, ZBP1 (Farina, Huttelmaier et al. 2003) and with F-actin (Oleynikov and Singer 2003). Delivering MTRIPs at 30 nM and 1 nM concentrations, we easily observed those associations in cells fixed post live-cell hybridization and stained with an anti-ZBP1 antibody. In **Figure 3.8 a and b** outstretched pseudopods showed colocalization in both the image and in the intensity profile plot, while in **Figure 3.8 c and d**, MTRIPs were observed aligned with stained stress fibers (see merge as well as inset image). From the widefield deconvolved 2D images, 3D images were reconstructed in Improvision's Volocity software (**Figure 3.9a**). From the overlap of voxels generated in Volocity, the

Manders overlap coefficient was calculated as 0.92, (**Figure 3.9b**) clearly indicating colocalization in three dimensions between human β-actin mRNA detected with MTRIPs and ZBP1. These experiments demonstrate that, using MTRIPs, it was possible to image the RNA of interest and an RNA binding protein simultaneously. These experiments also provided further evidence that the β-actin mRNA probes bound to their targets as β-actin mRNA are known to reside in RNA granules positive for ZBP1.

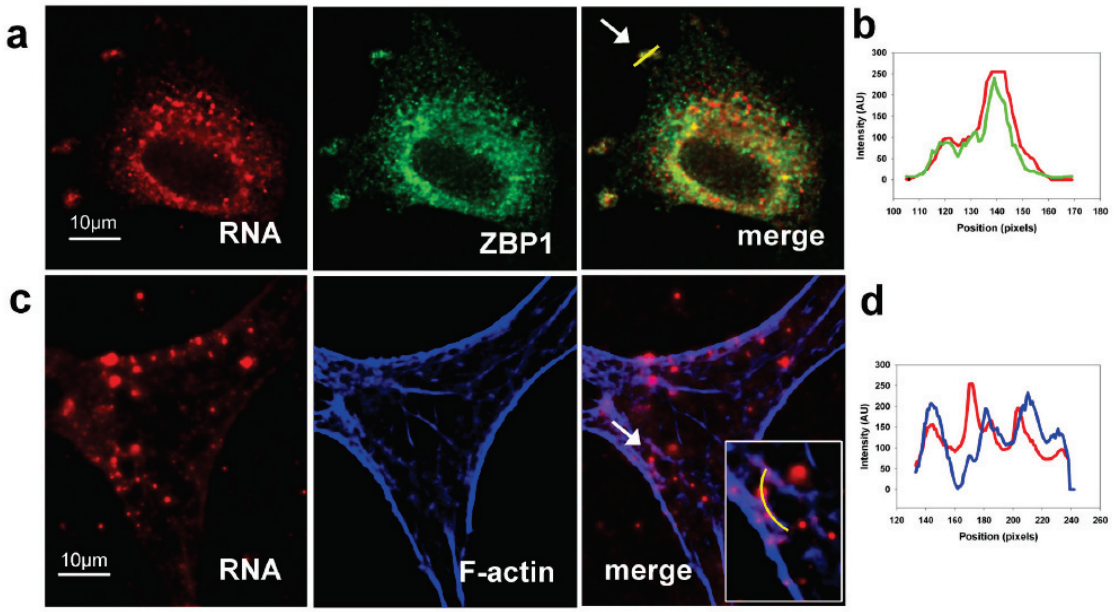

Figure 3.8 Single MTRIP targeting of native β-actin mRNA in motile A549 cells showing specific targeting when RNA aggregates spatially. (a,b) MTRIPs using human β-actinprobe 1 (red), delivered at 30 nM, colocalize (yellow) with ZBP1 (green), especially in the ends of pseudopods. Colocalization is observed both in the merge image, as well as in the intensity profile drawn through one of the pseudopods. (c,d) β-actin mRNA are also known to colocalizewith F-actin, and MTRIPs (red) delivered at 1 nM show colocalization (purple) with phalloidin stainedstress fibers (blue). Inset image within merge focuses on a region of significant colocalization, and intensity profile shows correlation of F-actin signal (blue) with MTRIPs (red).β-actin mRNA images were taken using epifluorescence microscopy, deconvolved, and a single optical plane is shown.

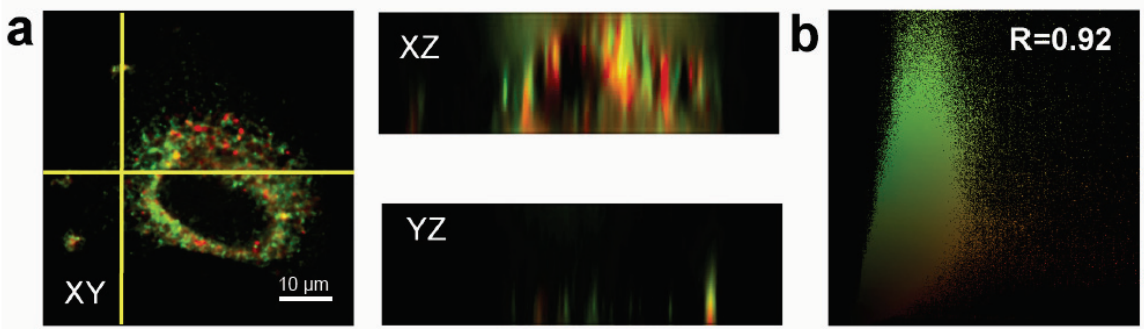

Figure 3.9: Quantification of MTRIP signal in 3D. Quantification of 3D colocalization of single (human β-actin mRNA probe 1) MTRIP targeted to β-actin mRNA and ZBP1 in a motile epithelial cell. (a) XY, XZ, and YZ profiles at location designated by the yellow cross-hair are provided as evidence of colocalization within both a pseudopod (YZ) and within the perinuclear region (XZ). Strong yellow signal can be observed in both cross-sections. (b) From the 3D reconstruction of voxels, a scatter plot of voxel intensities was generated and the Manders overlap coefficient calculated. In this case the Manders overlap coefficient was 0.92, suggesting significant colocalization in three dimensions.

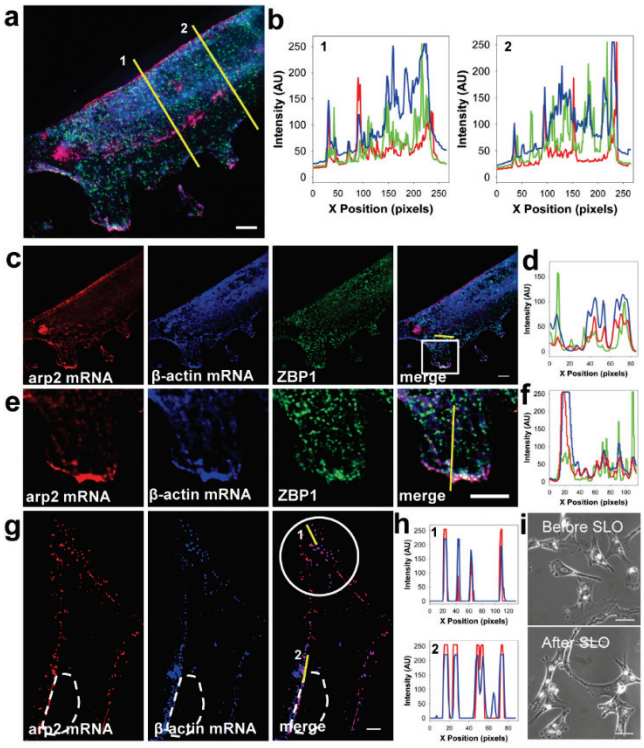

Figure 3.10: Imaging of arp2 and β-actin mRNA and ZBP1 in primary chicken embryonic fibroblasts (CEF). (a) Extended view of arp2 (red) and β-actin (blue) mRNA, and ZBP1 (green) in a motile primary CEF. Arp2 and β-actin mRNA were tagged with 3 MTRIPs (all probes in Supplementary Table) each labeled with Cy3B and Atto-647N via live-cell hybridization via SLO delivery, post-fixed in paraformaldehyde and immunostained with a guinea pig anti-ZBP1 antibody. (b) Intensity profiles through two cross-sections (denoted 1 and 2) of the extended view reveal two types of localization; within the perinuclear region, β-actin mRNA signal is not correlated with the arp2 mRNA signal, especially from approximately pixel 100 to 225 in profile 1 and from 100 to 150 and 175 to 225 in profile 2; ZBP1 and β-actin mRNA are correlated within these same regions. (c, d, e, f) While, from a single plane image of the cell, near the glass surface and within a lamellipodium (indicated by the white box), colocalization of arp2 (red) mRNA, β-actin (blue) mRNA, and ZBP1 (green) can be observed especially within the lamellipodium near the leading edge. (g,h) Live cell image of arp2 (red) and β-actin (blue) mRNA tagged with the same MTRIPs as above; granules within a protrusion of CEF show significant colocalization. Dashed white region represents the cell nucleus. (i) Phase contrast images of primary CEFs before and after SLO exposure show no significant changes in cellular morphology. The images were taken 20 minutes after SLO exposure. The white bars in (a,c,g,e) represent 5 μm and in (i) represent 50 μm.

Imaging of arp2 and β-actin mRNA and ZBP1 in primary chicken embryonic fibroblasts (CEF)

The experiments showing the lack of colocalization between an untargeted probe and a probe targeted toward the β-actin mRNA showed clear evidence that MTRIPs did not non-specifically aggregate in living cells. Taking this concept one step further, we hypothesized that two RNAs could be simultaneously imaged along with an RNA binding protein. β-actin mRNA and arp2 mRNA were chosen as it had previously been shown that the two mRNAs localize to the protrusions of motile CEFs (Mingle, Okuhama et al. 2005). The previous studies, however, were unable to test if they colocalize. The colocalization of these two mRNAs may further the evidence that in eukaryotes, mRNAs are packaged into functional granules which contain the mRNAs for proteins that function together and that these granules are transported to the sites where they are translated. In order to show the flexibility and applicability of this method, simultaneous imaging of two mRNAs in primary chicken embryonic fibroblasts (CEF) was performed (**Figure 3.10**). CEFs were used because they have been a well-studied model system for studying RNA localization (Oleynikov and Singer 2003). Three MTRIPS targeting separate sequences on β-actin mRNA and arp2 mRNA were chosen based on both previous sequences used 4 and mFOLD folding of arp2 mRNA, where large single stranded loop sections were chosen. Even though only 2 probes per RNA are necessary for specific detection in non-clustered RNA **Figure 3.1**, in order to optimize the signal for future dynamics studies, three probes per RNA were utilized **Table 3.1**. β-actin targeted MTRIPs were labeled with ATTO 647N and arp2 targeted probes with Cy3B. Probes were delivered into CEFs (30 nM for each probe) for 10 minutes via SLO

permeabilization; twenty minutes after delivery one set of cells was fixed for ZBP1 immunostaining while the other set utilized for live-cell imaging. In **Figure 3.10a** an extended view image of arp2 (red) and β-actin (blue) mRNA, and ZBP1 (green) in a motile primary CEF is presented. Intensity profiles **Figure 3.10a,b** through two crosssections of the extended view demonstrate two types of localization; in the perinuclear region, β-actin mRNA signal is not correlated with the arp2 mRNA signal, especially from approximately pixel 100 to 225 in profile 1 and from 100 to 150 and 175 to 225 in profile 2; ZBP1 and β-actin mRNA are correlated within these same regions. While, from a single plane image (**Figure 3.10 c-f**) of the cell near the glass surface, (**Figure 3.10 c,d**); colocalization of arp2 (red) and β-actin (blue) mRNA, and ZBP1 (green) can be observed within the lamellipodium, especially at the leading edge. Similar colocalization of the RNAs was observed in the live-cell image within a cellular protrusion and along the cellular periphery; this was demonstrated quantitatively in the intensity profiles (**Figure 3.10 g,h**).

In addition, in order to demonstrate that SLO delivery does not significantly affect even primary cells, phase contrast images of representative cells before and after SLO exposure (**Figure 3.10i**), show no changes in cell morphology or their ability to create lamellipodia, necessary for motility. The localization of both mRNA within the lamellipodia shown here, is consistent with a previous report on their localization(Mingle, Okuhama et al. 2005); our data though suggests that the two mRNA are likely separate within the perinuclear region but are packaged together when transported to protrusions or lamellipodia. This is reasonable given a report that arp3 mRNA likely contain a ZBP1 binding site (Shestakova, Singer et al. 2001), and from our

own sequence alignments (data not shown), arp2 mRNA are also likely to contain one. From the one previous report (Mingle, Okuhama et al. 2005), they claim these mRNA localize but do not colocalize, but from our examination of their data (data not shown), they may have underestimated the amount of colocalization.

Effects of SLO and MTRIPs mRNA stability and translatability

We subsequently investigated if SLO treatment and MTRIPs binding to their target transcripts would affect mRNA stability. While Lloyd et al. (Lloyd, Giles et al. 2001) demonstrated that SLO does not affect TNFα mRNA level and protein synthesis, mRNA decay in the presence of targeting MTRIPS has not been tested. To do this, we extracted total RNA from U2OS cells exposed to Actinomycin D for 0-4-8 and 24 h after either a mock treatment, SLO treatment or SLO-mediated MTRIPs delivery. We converted the total RNA in cDNA in the presence of random hexamers and analyzed the reaction product via qRT-PCR in the presence of either ACTB or GAPDH gene specific primers. We used GAPDH as an internal control since it was previously employed to study off target effects of SLO-delivered antisense RNAs (Giles, Spiller et al. 1998). The results, reported as the fold change of ACTB mRNA expression normalized to the control experiment (time 0, no treatment) relative to that observed for GAPDH, demonstrated that neither SLO treatment nor MTRIPS significantly affect mRNA stability for periods up to 8 h post delivery **Figure 3.11a**.

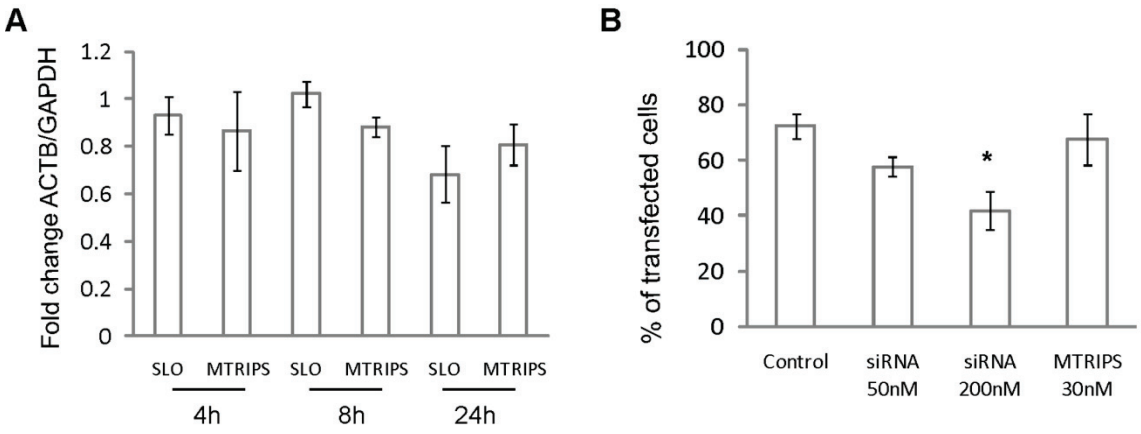

Figure 3.11: MTRIPs do not affect target mRNA stability and translatability. (A) mRNA decay in cells treated with SLO without or with MTRIPs was assayed upon treatment with Actynomicin D after 0, 4, 8 and 24 h as described in the text via qRT-PCR. β-actin mRNA expression fold change is normalized to GAPDH. (B) Percentage of cells expressing GFP-β-actin in control cells and in the presence of 50 nM or 200 nM siRNA or 30 nM MTRIPs. Error bars indicate standard deviation and * represents statistically significant difference ($P<0.05$).

We also studied the effects of MTRIPs on mRNA translatability. To do so, we monitored the expression of GFP-β-actin protein in transiently transfected U2OS cells in the presence of siRNA or MTRIPS, as described in Material and Methods. The results, summarized in **Figure 3.11b**, clearly demonstrated that, while siRNAs efficiently lowered the expression of GFP-β-actin, MTRIPs did not inhibit mRNA translation.

Effect of SLO and MTRIPs on stress granule formation

We verified that cell exposure to SLO does not cause SG formation (data not shown), then, after delivering MTRIPs, we induced oxidative stress, by incubating U2OS cells with 0.5 mM sodium arsenite for 1 h at 37°C, the typical sub-lethal concentration used to study stress-dependent translational inhibition. We observed that SGs formed within 90% of the cells and, as expected, they contained TIAR, G3BP and HuR (**Figure 3.12a**). SLO treatment had no effect on the efficiency of SG formation or protein content (**Figure 3.12b,c**). Using the Volocity software we identified the mRNA granules and the SGs as described in Material and Methods, and quantified their interactions. Poly A+ mRNA granules interacted with all detected SGs and occupied approximately 96% of their volume (**Figure 3.13a-c and Table 3.3**). β-actin mRNA granules interacted with over 90% of the analyzed SGs and occupied approximately 52% of their volume (**Figure 3.13d-f and Table 3.3**). As can be observed by comparing **Figure 3.13b and f**, the polyA+ transcripts within the SGs were larger and more visible than the β-actin ones and clearly filled the SG volume. Similar results were obtained using sodium arsenate at 2.5 mM for 1 h at 37°C in U2OS and treating U2OS cells with 1 mM and 2 mM sodium

arsenite for 1 hour at 37°C (**Table 3.4**). In this case, while the number of cells containing SGs increased to 100%, SG occupation by β-actin mRNAs was similar to that observed in the presence of 0.5 mM sodium arsenite or slightly lower, indicating that SG occupancy did not increase with the amount of stress, possibly due to saturation.

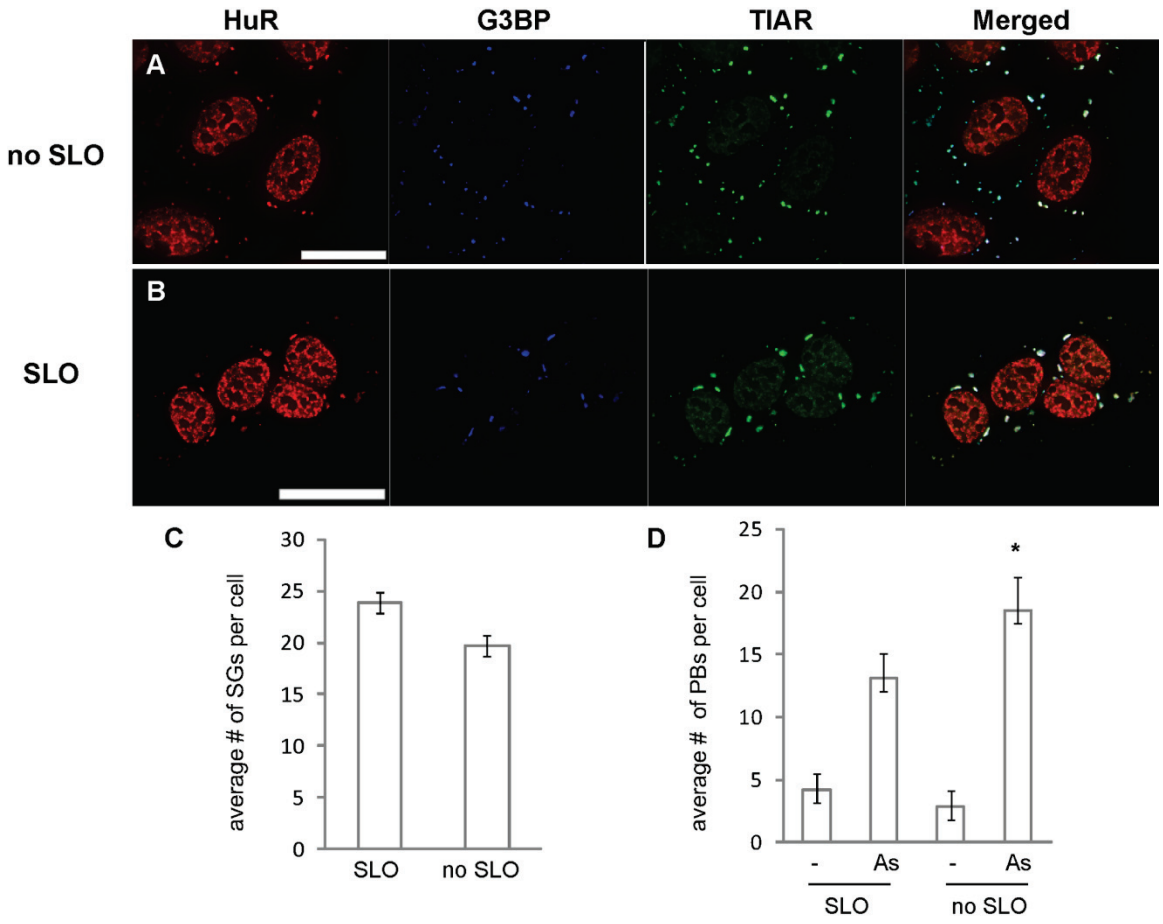

Figure 3.12: SLO treatment does not alter SG/PB formation and/or protein composition. Untreated U2OS cells (A) or treated with SLO (B) formed SGs that contain endogenous HuR, G3BP and TIAR proteins after treatment with 0.5 mM sodium arsenite for 1 h at 37°C. Scale bars, 10 µm. (C) Average number of SGs per cell observed upon sodium arsenite treatment with and without SLO. (D) Average number of PBs per cell in untreated (-) and treated cells (As) with and without SLO. Error bars indicate standard deviation and * represents statistically significant difference ($P<0.05$).

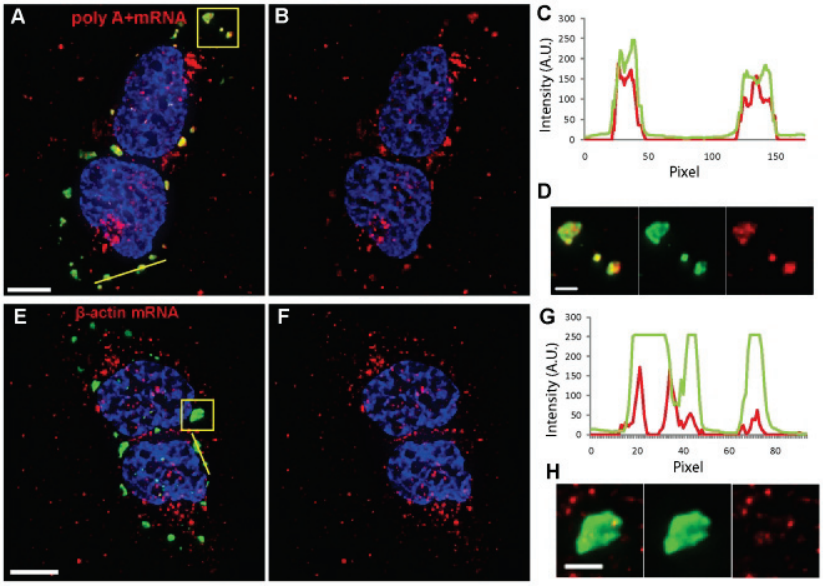

Figure 3.13: Poly A+ and β-actin mRNAs interact with SGs in the presence of sodium arsenite. (A, B) Poly A+ and (E, F) β-actin mRNA granules (red) interact with G3BP-stained SGs (green) in U2OS cells as demonstrated by intensity profiles along yellow lines (C, G) and insets displaying magnification of boxed areas (D,H). β-actin mRNA in B and F and in insets was contrast enhanced to allow visualization of granules. Nuclei were stained with DAPI. Scale bars, 10 μm and inset scale bars, 2.5 μm.

Table 3.4: SGs occupancy by β-actin mRNA in U2OS cells treated with increasing sodium arsenite concentrations. Percentage of SGs (% SGs) and percentage of SG volume (% SG vol) occupied by β-actin mRNA granules in the presence of sodium arsenite (As) 0.5, 1 and 2 mM. Standard deviations values are indicated.

	0.5 mM As	*1mM As*	*2 mM As*
% SGs	93	86	80
% SG vol	52±20	43±18	34±20

Preliminary live cell imaging

In addition, we imaged β-actin mRNA granules in living cells by time-lapse widefield fluorescence microscopy (**Figure 3.1**). We collected images with 90-ms exposure times at both 1 Hz and 5 Hz for 3 min and 30 s, respectively (**Videos 1, 2, 3**). This demonstrated the capacity to use this method in low- and high-speed tracking experiments; similar particle trajectories have been demonstrated for plasmid-derived mRNAs (Fusco, Accornero et al. 2003). As an additional control, we serum-starved A549 cells for 48 h and counted the β-actin mRNA granules in cells fixed after live-cell hybridization. A representative cell contained only 409 granules as compared with 1,455 granules detected in a cell grown with serum (data not shown), consistent with previous experiments (Latham, Kislauskis et al. 1994; Femino, Fay et al. 1998).

Quantification of a specific native mRNA within a live cell

In order to use this technique to accurately quantify the number of a specific native mRNA within a cell in a wider variety of granules, additional information will need to be obtained, that are beyond the scope of this paper. Currently using MTRIPS we can easily distinguish between single probes (377 ± 27 a.u.) and single RNAs (two probes, 677± 55 a.u.) and demonstrated that statistically. Once an mRNA is packaged into larger granules it would be difficult, at this point, to know if the fluorescence signal remains linear with RNA number. Non-linearity in the signal within a granule as a function of mRNA number could likely be caused by many effects, such as collisional quenching, and may require calibration-based compensation or post-processing depending on the contents and size of the granule and its location within the cell (Iseni,

Garcin et al. 2002). Future experiments using time-resolved fluorescence microscopy could be performed to evaluate the effects of quenching and correlate them with granule size and location within the cell.

Summary

In this chapter the experiments outlining the targeting of β-actin mRNA were outlined and analyzed. Using complementary techniques we attempted to assess whether or not MTRIPs, with sequences complementary to those of the β-actin mRNA, were capable of labeling β-actin mRNA in live cells. The following results were obtained that we believe positively demonstrates MTRIPs are useful in labeling mRNA in live cells:

- A 2× increase in fluorescence intensity was seen for probes on glass vs. cytoplasmic granules.
- There was little colocalization of targeted and untargeted probes delivered into cells
- Proper localization of actin mRNA targeted probes to leading edge and pseudopodia
- The number of granules per cell in serum stimulated cells
- Increase in fluorescence intensity with increasing number of probes
- Non colocalization of MTRIPs with early and late endosomal markers
- Increase in the number of mRNA granules under serum stimulation as compared with non-stimulation and serum starvation
- Decrease in the number of β-actin mRNA granules upon treatment with β-actin mRNA specific siRNA
- Colocalization of MTRIP granules with mRNA granules identified by FISH

- Colocalization of mRNA granules and ZBP1 immunofluorescence
- Colocalization of β-actin mRNA granules with f-actin
- Colocalization of β-actin mRNA in lamelepodia with arp2 mRNA and ZBP1 in CEFs

In addition to demonstrating the MTRIPs can accurately label β-actin mRNA, we also demonstrated several important aspects relating to the utility of MTRIPs, delivered using SLO, in imaging mRNA in live cells. Specifically we demonstrated:

- Probes observable in widefield and confocal microscopy
- Probes fluorescent for >30 s
- SLO did not cause cell death
- Probes did not crosslink mRNA granules
- Probes did not alter mRNA stability
- Probes did not alter mRNA translatability
- Probes did not cause or prevent stress granule formation

With these results, it was assumed that MTRIPs, delivered by SLO, allowed for the accurate imaging of β-actin mRNA in live cells. In the proceding chapter these probes will be used to study the dynamics of β-actin mRNA and resolve standing dispute in thefield of mRNA dyanics.

Materials and methods

MTRIPs.

The 2′ *O*-methyl RNA-DNA chimera nucleic acid ligands were synthesized by Biosearch Technologies, Inc. Each contains a 5′ biotin modification and multiple dT-C6-NH_2,

modifications. The streptavidin used for the core was purchased from Pierce. Probes were assembled by first labeling the free amine groups on the ligands with either Cy3B–NHS ester (GE Healthcare) or Atto 647N–NHS ester (Atto-Tec GmbH) using manufacturers' protocols. Free dye was removed using both Nanosep spin columns (Pall Corp.) and illustra G-25 size-exclusion columns (GE Healthcare). The purified ligands were resuspended in 1× phosphate-buffered saline (PBS; pH 7.4) and mixed at a 10:1 molar ratio with streptavidin for 1 h at room temperature (18–22 °C). Free ligands were removed using 30 kDa Nanosep spin columns, and stored at 1 μM final concentration in 1× PBS at 4 °C. When multiple probes were used, each probe was completely assembled and filtered separately, and then mixed with equimolar concentrations in streptolysin O and medium just before delivery into cells We estimated the cost of MTRIPs, based on 30 nM delivery concentration, to be $0.15 per well, for a 24-well plate.

Probe delivery.

MTRIPs were delivered into A549 and CEF cells using a reversible permeabilization method with streptolysin O (Sigma). Cells grown in complete medium were first washed with 1× PBS and then incubated with a mixture of 0.2 U ml^{-1} of streptolysin O and probe (concentrations were noted in the main text) in an appropriate amount of complete growth medium for 10 min at 37 °C. The mixture of streptolysin O, probe and medium was then removed and replaced with fresh, complete growth medium or Leibovitz's L15 medium supplemented with 10% FBS. Live cells were imaged typically 20 min immediately after delivery by epifluorescence microscopy. Using streptolysin O–based delivery, probes were delivered into A549 and CEF cells with 100% efficiency.

Fluorescence in situ hybridization (FISH): MTRIPs labeled with Dylight 649 targeting β-actin mRNA (probe sequences 2 and 7 in Table S1) were delivered into A549s as described above. Cells were subsequently fixed in 4% paraformaldehyde, permeabilized in 70% ethanol overnight, rinsed in PBS three times and incubated for 2hr at 55ºC in hybridization buffer (2×SSC (Ambion), 100 µg BSA, 10% dextran sulfate, 50 µg tRNA, 70 % formamide, 50 µg salmon sperm DNA and probes at 1 nM each). Probes used for FISH were linear Cy3B-labeled nucleic acid ligands (probe sequences 1, and 3-6 in Table S1). After hybridization, cells were rinsed with 2×SSC for 5 min, 10% fomamide in 2×SSC for 10 min and in 2×SSC for 5 min. Nuclei were stained using DAPI (Invitrogen) and cells were mounted on slides using Prolong gold (Invitrogen).

siRNA delivery and qRT-PCR: A549 cells were transfected with 200 nM control siRNA or siRNA targeting β-actin mRNA (On target plus non targeting siRNA #1 and smart pool respectively, Dharmacon thermo Scientific) via electriporation using the Neon system (Invitrogen) according to manufacturer instructions. Transfections were performed in duplicates and a set of control cells was also plated. 48h post transfection MTRIPs targeting β-actin mRNA were delivered to a set of cells, which were subsequently fixed, stained with phalloidin and DAPI and mounted. The second set of cells was used for total RNA extraction using the RNeasy Mini kit (Quiagen). Total RNA was subsequently checked for integrity via agarose gel electrophoresis and quantified via UV-VIS spectrometry. 1µg total RNA was used for cDNA synthesis using the RT^2 first strand kit (SA biosciences) according to the manufacturer instructions. 1µl of the product was then used for qRT-PCR using the Real-time RT^2 qPCR primer assay (SYBR green) in the presence of human ACTB and GAPDH gene-specific primers (SA bioscences).

qRT-PCR was performed using ABI StepOnePlus real-time PCR system (Applied biosciences).

Immunofluorescence: Cells were fixed for 10 min in 4% paraformaldehyde (Electron Microscopy Sciences, Hatfield, PA) and they were then immunostained for Early Endosomal Antigen 1 (mouse anti-EEA1, BD Biosciences, San Jose, CA), Cluster of Differentiation 63 (mouse anti-CD63, Developmental Studies Hybridoma Bank, Iowa City, IA), Lysosomal-associated membrane protein 1 (mouse anti-LAMP1, Developmental Studies Hybridoma Bank), β-tubulin (Invitrogen), or γ-tubulin (Sigma) as described (Lifland, Zurla et al. 2010) or by manufacturers' protocol. Alexa fluor 488 Phalloidin was used to stain actin fibers. Cells were subsequently stained with DAPI (Invitrogen) and mounted on slides using Prolong gold (Invitrogen).

Delivery of Neutravidin-TAT: Neutravidin was fluorescently labeled with Cy3B according to the manufacturer's protocol. Labeled Neutravidin was subsequently conjugated to biotin-TAT peptide (Anaspec, Fremont, CA) by incubation at room temperature at a 1:40 molar ratio. Unbound biotin-TAT peptides were separated from the conjugate using a 30K MWCO centrifugal filter. A549 cells were incubated with 250 nM NA-TAT conjugates in normal growth media for 15 min or 2 hrs, fixed and immunostained as described.

Image Processing and analysis: All live and fixed cell images were deconvolved using Volocity’s deconvolution algorithms. Image Z-stacks were deconvolved using iterative restoration and live cell movies were deconvolved using fast restoration. Granule counting and intensity quantification as well as Manders' and Pearson’s coefficients were

computed in Volocity and imported into Excel (Microsoft, Redmond, WA) or Sigma Plot (Systat, Chicago, IL for plotting. Kruskal–Wallis and ANOVA statistical tests were performed in MATLAB (The MathWorks, Natick, MA) or Sigma Plot. Images presented have been linearly contrast enhanced for clarity. All calculations were performed directly on unenhanced, deconvolved data. Standard deviation maps were computed using the ZProject plugin for NIH ImageJ on deconvolved image sets exported in Tiff format. Intensity profile plots were generated in ImageJ using the RGB profiler plugin.

Counting granules and statistical analysis of RNA granule populations.

For data shown in **Figure 3.1**, granules were identified and counted using Improvision's Volocity software in three dimensions using either confocal images or from widefield fluorescence images, deconvolved using an iterative deconvolution algorithm in Volocity. For data shown in **Figure 3.1**, granules were counted using deconvolved data and identified based on the s.d. of intensities; 4 s.d. above the mean was used to locate the granules in all cases because it avoided the detection of noise or objects substantially smaller than the point spread function. Because of this, no limit on minimum granule size was necessary when counting granules. In general, the cells deconvolved using the three-dimensional interative algorithm in Volocity lacked considerable noise due to filtering in the algorithm. Notably, the s.d. in mean granule intensity for the granules in **Figure 3.1c** and in the serum-starved cell (data not shown) were only 25% and 21%, respectively, reflecting the uniformity of the granules when measured in three dimensions.

Time-lapse fluorescence microscopy: Live-cell video microscopy was performed using cells grown in Bioptechs T4 plates with an objective heater. The cells were imaged in

Leibovitz's L15 medium supplemented with 10% FBS. Images were taken with a Zeiss Axiovert 200M microscope, with an ×63, numerical aperture (NA) = 1.4 Plan-Apochromat objective and Hamamatsu ORCA-ER AG camera, using Chroma 49002 ET-GFP and 49004 ET-Cy3 filter sets, controlled by Volocity software. For β-actin mRNA granule dynamics, images were taken either at 1 or 5 Hz with 90-ms exposures for 3 min and 30 s, respectively. For the stress granule-RNA experiments, images of GFP–TIA-1 and the Cy3B-labeled MTRIPS were taken at 0.2 Hz (every 5 s), with exposure times of 71 and 41 ms, respectively, for up to 8 min.

Starvation assay: A549 cells were serum-starved in DMEM with 100 U ml^{-1} of penicillin and 100 mg $ml^{-1}$of streptomycin for 48 h. MTRIPS (human β-actin mRNA probes 1 and 2) were delivered with streptolysin O. Twenty minutes after delivery, the cells were fixed in 4% paraformaldehyde and stained with DAPI. The granules in a particular cell were then counted using the method described above.

Fluorescence imaging. Immobilized Cy3B and Atto 647N probes on the glass surface were imaged using a Zeiss Axiovert 200M microscope with an ×63, NA = 1.4 Plan-Apochromat objective, using Chroma 49004 ET-Cy3 and 49006 ET-Cy5 filter sets, with 500-ms exposures. An EXFO excite 120 light source with a ND (neutral density) = 0.4 (40% transmission) was used for fluorescence excitation, and a Hamamatsu ORCA-ER AG for taking digital images. Live-cell images of single probes within A549 cells were taken with 350 ms exposures under the same illumination conditions. *Z*-dimension stacks were taken in both cases, in 200-nm steps, and deconvolved using Volocity iterative deconvolution algorithm. Cells used in the human β-actin mRNA-scrambled probe experiments were fixed after live-cell hybridization and imaged similarly to the

immobilized probes, but with 200-ms exposures and deconvolved in Volocity. Time-lapse live cell images were taken as discussed above, and were processed with Volocity's 2D or fast deconvolution algorithm. In the stress granule control experiments, live cell images were taken similarly to the single probe images but with 50-ms exposures. hRSV after-delivery, fixed-cell control experiments were imaged with a Zeiss LSM 510 Meta using an ×63, NA = 1.4, Plan-Apochromat objective. All images were taken using multi-track scanning for each fluorophore to prevent bleed-through. *Z*-dimension stacks were taken in 0.5-μm increments; the 543 nm laser (Cy3B probe) was set at 25% power, the 488 nm laser (for N protein immunostaining) was set at 37%, and the pinholes were set to an airy unit of 1 (equal to airy disk). β-actin mRNA, actin-related protein 2 homolog mRNA and ZBP1, in the chicken embryonic fibroblasts, were imaged under similar conditions to the human β-actin mRNA experiments.

References

Abe, H. and E. T. Kool (2006). "Flow cytometric detection of specific RNAs in native human cells with quenched autoligating FRET probes." Proc Natl Acad Sci U S A **103**(2): 263-268.

Barry, E. L., F. A. Gesek, et al. (1993). "Introduction of antisense oligonucleotides into cells by permeabilization with streptolysin O." Biotechniques **15**(6): 1016-1018, 1020.

Ben-Ari, Y., Y. Brody, et al. (2010). "The life of an mRNA in space and time." J Cell Sci **123**(Pt 10): 1761-1774.

Bhakdi, S., U. Weller, et al. (1993). "A guide to the use of pore-forming toxins for controlled permeabilization of cell membranes." Med Microbiol Immunol **182**(4): 167-175.

Clark, R. E., J. Grzybowski, et al. (1999). "Clinical use of streptolysin-O to facilitate antisense oligodeoxyribonucleotide delivery for purging autografts in chronic myeloid leukaemia." Bone Marrow Transplant **23**(12): 1303-1308.

Farina, K. L., S. Huttelmaier, et al. (2003). "Two ZBP1 KH domains facilitate beta-actin mRNA localization, granule formation, and cytoskeletal attachment." J Cell Biol **160**(1): 77-87.

Femino, A. M., F. S. Fay, et al. (1998). "Visualization of single RNA transcripts in situ." Science **280**(5363): 585-590.

Fusco, D., N. Accornero, et al. (2003). "Single mRNA molecules demonstrate probabilistic movement in living mammalian cells." Curr Biol **13**(2): 161-167.

Giles, R. V., D. G. Spiller, et al. (1998). "Selecting optimal oligonucleotide composition for maximal antisense effect following streptolysin O-mediated delivery into human leukaemia cells." Nucleic Acids Res **26**(7): 1567-1575.

Iseni, F., D. Garcin, et al. (2002). "Sendai virus trailer RNA binds TIAR, a cellular protein involved in virus-induced apoptosis." Embo J **21**(19): 5141-5150.

Kislauskis, E. H., X. Zhu, et al. (1994). "Sequences responsible for intracellular localization of beta-actin messenger RNA also affect cell phenotype." J Cell Biol **127**(2): 441-451.

Latham, V. M., Jr., E. H. Kislauskis, et al. (1994). "Beta-actin mRNA localization is regulated by signal transduction mechanisms." J Cell Biol **126**(5): 1211-1219.

Lifland, A. W., C. Zurla, et al. (2010). "Single Molecule Sensitive Multivalent Polyethylene Glycol Probes for RNA Imaging." Bioconjug Chem.

Lloyd, B. H., R. V. Giles, et al. (2001). "Determination of optimal sites of antisense oligonucleotide cleavage within TNFalpha mRNA." Nucleic Acids Res **29**(17): 3664-3673.

Lopez de Silanes, I., S. Galban, et al. (2005). "Identification and functional outcome of mRNAs associated with RNA-binding protein TIA-1." Mol Cell Biol **25**(21): 9520-9531.

Lopez de Silanes, I., M. Zhan, et al. (2004). "Identification of a target RNA motif for RNA-binding protein HuR." Proc Natl Acad Sci U S A **101**(9): 2987-2992.

Mingle, L. A., N. N. Okuhama, et al. (2005). "Localization of all seven messenger RNAs for the actin-polymerization nucleator Arp2/3 complex in the protrusions of fibroblasts." J Cell Sci **118**(Pt 11): 2425-2433.

Oleynikov, Y. and R. H. Singer (2003). "Real-time visualization of ZBP1 association with beta-actin mRNA during transcription and localization." Curr Biol **13**(3): 199-207.

Paillasson, S., M. Van De Corput, et al. (1997). "In situ hybridization in living cells: detection of RNA molecules." Exp Cell Res **231**(1): 226-233.

Rhee, W. J., P. J. Santangelo, et al. (2008). "Target accessibility and signal specificity in live-cell detection of BMP-4 mRNA using molecular beacons." Nucleic Acids Res.

Rinne, J., B. Albarran, et al. (2007). "Internalization of novel non-viral vector TAT-streptavidin into human cells." BMC Biotechnol **7**: 1.

Ross, A. F., Y. Oleynikov, et al. (1997). "Characterization of a beta-actin mRNA zipcode-binding protein." Mol Cell Biol **17**(4): 2158-2165.

Santangelo, P., N. Nitin, et al. (2006). "Live-cell characterization and analysis of a clinical isolate of bovine respiratory syncytial virus, using molecular beacons." J Virol **80**(2): 682-688.

Santangelo, P. J. and G. Bao (2007). "Dynamics of filamentous viral RNPs prior to egress." Nucleic Acids Res **35**(11): 3602-3611.

Santangelo, P. J., A. W. Lifland, et al. (2009). "Single molecule-sensitive probes for imaging RNA in live cells." Nat Methods **6**(5): 347-349.

Santangelo, P. J., N. Nitin, et al. (2005). "Direct visualization of mRNA colocalization with mitochondria in living cells using molecular beacons." J Biomed Opt **10**(4): 44025.

Santangelo, P. J., B. Nix, et al. (2004). "Dual FRET molecular beacons for mRNA detection in living cells." Nucleic Acids Res **32**(6): e57.

Shestakova, E. A., R. H. Singer, et al. (2001). "The physiological significance of b-actin mRNA localization in determining cell polarity and directional motility." PNAS **98**: 7045-7050.

Spiller, D. G., R. V. Giles, et al. (1998). "Improving the intracellular delivery and molecular efficacy of antisense oligonucleotides in chronic myeloid leukemia cells: a comparison of streptolysin-O permeabilization, electroporation, and lipophilic conjugation." Blood **91**(12): 4738-4746.

Utley, T. J., N. A. Ducharme, et al. (2008). "Respiratory syncytial virus uses a Vps4-independent budding mechanism controlled by Rab11-FIP2." Proc Natl Acad Sci U S A **105**(29): 10209-10214.

Vargas, D. Y., A. Raj, et al. (2005). "Mechanism of mRNA transport in the nucleus." Proc Natl Acad Sci U S A **102**(47): 17008-17013.

Walev, I., S. C. Bhakdi, et al. (2001). "Delivery of proteins into living cells by reversible membrane permeabilization with streptolysin-O." Proc Natl Acad Sci U S A **98**(6): 3185-3190.

CHAPTER 4

DYNAMICS OF BETA ACTIN MRNA

Background

Messenger ribonucleic acids (mRNAs) are thought to serve as a key intermediary in gene expression through their specific and dynamic molecular composition (Anderson and Kedersha 2009). Transport of mRNAs in the cytoplasm is essential for localization to sites of translation and for the sorting to discrete cytoplasmic foci during post-transcriptional regulation (Anderson and Kedersha 2009; Holt and Bullock 2009; Martin and Ephrussi 2009). Owing to the high viscosity, significant crowding and inhomogeneous nature of the cytoplasm, active transport of mRNA is likely required even if the overall result is to evenly distribute individual mRNAs throughout the cell (Luby-Phelps 2000). Actin and microtubule-dependent motors, myosin, kinesin and dynein, have all been shown to be necessary for mRNA localization but their role in mRNA transport is not clear (Jansen 2001). Indeed, it may be obscured by non-enzymatic and indirect functional roles such as anchoring to the cytoskeleton or reshaping of the environment around the mRNA granules (Delanoue and Davis 2005). In order to determine the contribution of molecular motors and the cytoskeleton to mRNA transport, it is essential to be able to visualize and track single mRNAs or single mRNA granules in live cells. Many cis and trans-acting factors responsible for the localization and regulation of mRNA have been identified; however, mechanistic information has been largely inferred from endpoint analysis, insertion of cis-acting sequences into transgenes, and delivery of synthetic transcripts into live cells (Sundell and Singer 1991; Bertrand,

Chartrand et al. 1998; Wilkie and Davis 2001; Fusco, Accornero et al. 2003; Zimyanin, Belaya et al. 2008). Since proper regulation of mRNAs requires the correct mRNA coding sequence, untranslated regions (UTRs), and the placement of exon junction complexes (EJCs) during nuclear processing (Hachet and Ephrussi 2004; Ben-Ari, Brody et al. 2010), the study of unaltered, native transcripts is critical.

Among all the transcripts in the mammalian genome, β-actin mRNA represents a useful model system to investigate mRNA transport because its localization has been studied in different cell types such as fibroblasts, epithelial cells and neurons (Condeelis and Singer 2005). Several mechanisms have been proposed for the transport of β-actin mRNA, including transport on microtubules, transport on microfilaments and diffusion throughout the cytoplasm (Condeelis and Singer 2005; Yamagishi, Ishihama et al. 2009; Yamagishi, Shirasaki et al. 2009). Initial reports using endpoint analysis and fluorescence in situ hybridization (FISH) in chicken and mouse embryonic fibroblasts, suggested that β-actin mRNA localization was dependent on actin filaments and that movement occurred along actin fibers (Sundell and Singer 1991; Latham, Yu et al. 2001; Johnsson and Karlsson 2010). Because these experiments were performed in fixed cells, the actual mode of transport needed to be inferred from experimental treatments. Several alternative hypotheses can be generated from these data including non-motor based movement of mRNAs attached to an actin cytoskeleton that is actively protruding, and movement of mRNA by diffusion or along microtubules along with anchoring of mRNA selectively on actin filaments. Later, live cell experiments using the MS2-GFP system in COS7 cells showed that a reporter mRNA encoding the bacterial protein LacZ was actively transported along microtubules in the presence and absence of the zipcode binding

protein (ZBP1) binding sequence, a key factor in β-actin mRNA localization. The presence of the ZBP1 binding site did, however, increase the persistence of transport, that is the distance a single RNA traveled during motor driven transport, and the apparent number of particles undergoing directed, motor-driven transport, although the latter may be due to the greater ease of identifying directed particles as they move larger distances (Fusco, Accornero et al. 2003). While this microtubule dependent transport is consistent with live cell tracking studies of IMP1-containing granules (the human ZBP1 orthologue) (Nielsen, Nielsen et al. 2002), it is inconsistent with the FISH experiment results on native β-actin mRNA. Other reports using the MS2-GFP and MS2-YFP system with a reporter mRNA containing the β-actin coding sequence suggest that both transport and localization are diffusion dependent (Yamagishi, Ishihama et al. 2009; Yamagishi, Shirasaki et al. 2009; Ben-Ari, Brody et al. 2010), controlled by the size of the mRNA and not by its sequence (Yamagishi, Shirasaki et al. 2009). This however is inconsistent with multiple reports that the sequences of mRNA, in particular the 3'-UTR of mRNA and specifically the zipcode binding region of β-actin mRNA, are necessary for the proper localization to the lamellipodium.

Here, we employed single-RNA sensitive multiply-labeled tetravalent imaging probes (MTRIPs) delivered into live cells to track the movement of native, non-engineered, β-actin mRNA at the single mRNA granule level and analyzed the data using standard deviation maps and single particle tracking with temporal analysis. This was done in order to establish the role of the different cytoskeletal elements in mRNA dynamics, in the attempt to provide clarity in the conflicting data in the field and test the hypotheses that the observed differences previously discussed might be cell type

dependent, as recently proposed (Condeelis and Singer 2005). For this purpose, experiments were performed in A549 cells, an epithelial cell line, as well as in primary human dermal fibroblasts (Santangelo, Lifland et al. 2009). We demonstrated that native β-actin mRNAs, under physiologic conditions, exhibit bursts of intermittent, processive motion on microtubules, interspersed between time periods of diffusive motion, during which transport is aided by non-thermal forces, resulting in enhanced diffusivity. We demonstrate that the movement of the mRNA granules throughout the cytoplasm is mediated by processive, active transport, since it is ATP and temperature-dependent, and it relies on molecular motors. Moreover, we demonstrate that an intact microtubule network is required for mRNA transport in both epithelial cells and human fibroblasts.

Live-cell Imaging

MTRIPs targeting β-actin mRNA were previously shown to colocalize with ZBP1 and with Arp2 mRNAs in the protrusions of A549s and CEFs, and were shown to undergo directed motion in A549s (19). Preliminary live cell experiments using two MTRIPs targeting the β-actin mRNA coding region allowed the imaging and tracking of native granules in live cells for approximately one minute at 5 Hz frame rate during continuous imaging (Santangelo, Lifland et al. 2009); however the nature of mRNA motion was not investigated nor was its cell type dependence addressed. Moreover, processes governing mRNA transport may occur on longer time scales than those previously utilized. Indeed, it's been proposed that mRNA may change between transport mechanisms within minutes (Fusco, Accornero et al. 2003).

Live cell imaging was performed using MTRIPs with all 6 probe sequences (**Figure 4.1A** and **Video 4**) and data were analyzed either by computing standard deviation (SD) maps for each image time series over short (seconds) or long (tens of seconds) time scales, or using single particle tracking. SD maps are pixel by pixel calculations of the standard deviation of the intensity calculated over given time lags that yield two dimensional representations of time series imaging data. High fluctuations in intensity over the time series correspond to high intensity values in the SD map and indicate particle movement through the area over the time scale analyzed (Cai, Verhey et al. 2007; Cai, McEwen et al. 2009). SD maps, therefore, allow discrimination between fast movements of mRNA granules within the cells when analysis takes place over short time scales and slow or cumulative movements when analysis is performed over longer time scales. SD maps were used in place of maximal intensity projections because SD maps reduce signal from static particles and are less sensitive to loss of signal intensity by photobleaching. While less quantitative than single particle tracking, whole cell mapping provided insight into the nature of mRNA movement while remaining computationally less intensive. SD Maps also allowed for all of the granules to be analyzed at once and movement through subcellular regions to be isolated. In A549 cells, short time scale analysis of cytoplasmic mRNAs revealed fast curvilinear movements, indicative of molecular motor-driven active transport (**Figure 4.1B**) and diffusive motion (**Figure 4.1C**). Active transport was observed to be intermittent and granules would often undergo several rounds of transport during the five minute imaging period. Some mRNA granules exhibited a coordinate motion as they would simultaneously begin moving collinearly and simultaneously stop (**Figure 4.1D** and **Video 5**). SD maps revealed that

these intermittent directed movements over time allowed the mRNAs to explore the entire cytoplasmic volume in ~300 seconds (**Figure 4.1E**). mRNAs not undergoing such movements were observed to be either stalled or exhibited a random walk-like motion (**Figure 4.1C**) and were observed in the perinuclear region as well as along the cell edges. Stalled granules displayed few, short (~5 s) time-scale movements (**Figure 4.1F**), but motion was indeed observed over long (~100 s) time scales, particularly at the leading edge of cells (**Figure 4.1G and H**). This motion suggested that these stalled granules were anchored to the cytoskeleton and moving according to extensions or retractions of the leading edge. In contrast, static mRNA granules in the perinuclear region did not exhibit either short or long time scale movements (**Figure 4.1 I and J** respectively). The curvilinear motion was more indicative of microtubule driven motion as the particle tracks formed lines of straight sections curved sections and rarely parallel tracks. Actin stress fibers tend to be formed parallel to each other and form straight lines with little curvature. The slow, parallel movement toward the edge of the cell suggests that the mRNAs are anchored to the cytoskeleton there and are protruding out with the plasma membrane. Phase contrast imaging confirmed that the plasma membrane is perpendicular to the movement of the mRNA granules. These data provide the first evidence that previous phenomena, where β-actin mRNA are seen localized to the edge of spreading and moving cells, may be due to mRNA spreading and moving with the cell and not localization post lamellae formation. These data also refute the supposition that diffusion of the mRNA is sufficient to localize them to the leading edge as diffusion is rarely results in particle tracks that are parallel and linear. While diffusion through a restricted structure with a diameter smaller than the diffraction limit may account for the

linearity of motion, it cannot account for the persistence of motion toward the leading edge as particles would diffuse both toward and away from the edge. SD maps are limited in their ability to precisely measure diffusion coefficients and transport velocities, so other analysis methods needed to be used to measure these values.

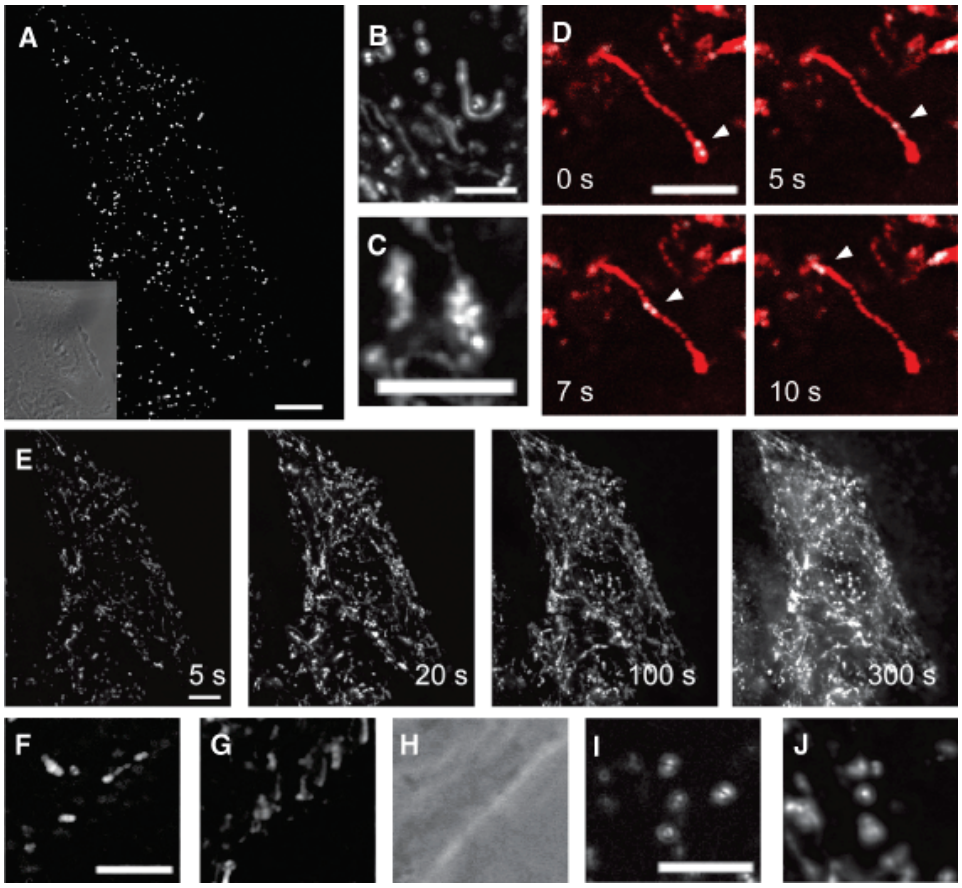

Figure 4.1: SD maps of β-actin mRNA dynamics in live A549 cells. A) A single optical plane at one time-point showing well-spaced distribution of β-actin mRNA granules. Inset shows the phase contrast image of the same cell. B) SD map over 14 seconds of imaging showing mRNA granules undergoing processive motion. C) SD map over 40 seconds of imaging showing mRNA granules undergoing diffusive motion. D) Time series of two particles (white, denoted by arrowheads at each time point) undergoing co-ordinated movement overlaid to the corresponding SD map (red). E) SD maps of the same cell as in (A) calculated over 5, 20, 100 and 300 seconds. mRNAs display an increase in the area explored as analysis is performed on larger time scales. SD map of mRNA granules near the leading edge of a cell calculated over (F) 5 and (G) 120 seconds. mRNAs are nearly static as the 5-second time scale but at longer time scales appear to undergo slow movement. (H) Phase contrast image showing edge of cell at the beginning of the time series for (F) and (G). SD maps of particles near the nucleus of a cell calculated over (I) 5 and (J) 120 seconds show almost no movement even over the longer time scales. Scale bars are 10 µm in (A, E and D) and are 5 µm in the remaining images.

Single particle tracking

Single particle tracking (SPT) allowed for a more detailed analysis of the dynamics of individual mRNAs (**Figure 4.2** A-G). **Figure 4.2 A** and **Video 6** show a typical particle trace of a β-actin mRNA granule within the cytoplasm of A549 cells with the corresponding SD map. Each particle trace was segmented using a temporal rolling window algorithm (Arcizet, Meier et al. 2008) in order to discriminate between states of active, processive motion, and passive, diffusive motion. The temporal nature of this analysis was needed because classifying each particle as either an actively transported granule or a diffusive granule would lead to an averaging of both of these transport modes. In order to separate active motion from passive motion a metric must be used by which individual sections of the particle track can be classified into each category. In SPT two main categories of metrics are used, trajectory extent and trajectory shape. Trajectory extent metrics measure, in various ways, the distance a particle moves over time. Because particles do not move in one direction and may even move toward and away from a point of origin along the same track, simple distance measures, such as displacement, may give artifactually low measures of trajectory extent. Measures of trajectory shape, typically asymmetry, are used to distinguish the random angle nature of random walks from the straight line nature of motor driven transport. Several complications arise with this metric principally that any given random walk will likely be asymmetric and several segments must be averaged in order to distinguish between an asymmetrical path and a circular one. Temporal analysis for these experiments was performed by calculating the square of the radius of gyration (R_G^2) for each mRNA granule along the rolling window. The radius of gyration, typically used as a measure of

the spread and growth of organic polymers, ameliorated the problems with displacement in that it can measure a trajectory extent even as the trajectory loops back upon itself and ends at the origin. An asymmetry parameter, the ratio of the smaller to the larger principal radius of gyration, termed the eigenvalue ratio, was tested as a means of further separating and identifying active and passive motion. However, because the duration of motor driven transport was on average 1-2 s the number of data points in each track was only 5-10. With this number of points, it is nearly impossible to determine if an individual track segment is asymmetric making the asymmetry parameter of no value in bifurcating the particle trace (Saxton 1994). In order to determine whether or not a particular track segment represents active, directed motion or passive, diffusive motion, a threshold value for the radius of gyration needed to be determined. Monte Carlo simulations were used to set a threshold such that there was less than a 1% chance that passive motion would be categorized as active transport or active transport categorized as passive (**Figure 4.2**) (Saxton 1994). Two set of Monte Carlo simulations were run. In the first, only pure diffusion was simulated. Diffusion coefficients were chosen from the literature and the radius of gyration was plotted as a histogram. In the second set of simulations, an active, directed motion with constant velocity was superposed onto the same diffusive motion used previously. The velocity value was chosen from representative literature. When both of these simulations are plotted as histograms with respect to the resulting radius of gyration, it can be seen that less than 1% of the trajectories from the pure diffusion experiments exceed a radius of gyration of 0.05 μm^2 and less than 1% of the diffusion plus directed motion have a radius of gyration less than 0.05 μm^2; therefore, 0.05 μm^2 was chosen as the threshold value to separate diffusive and

motor driven transport. Trajectory segments where R_G^2 exceeded the threshold of 0.05 μm^2 corresponded to linear increases in displacement, sustained increases in instantaneous velocity, and linear motion in the particle trace (**Figure 4.2C-E**). We analyzed 60 independent particle tracks and obtained a cumulative histogram of the instantaneous velocities during active transport. Manual tracking, where particle centroids are found by a user on a particle by particle and frame by frame basis was utilized due to the failure of the Volocity software to reliably track particles using the automatic tracking module. Bias was minimized by utilizing separate users to track particles and analyze the resulting tracks. A Gaussian fit of the histogram revealed a peak at 0.9 μm/s ±0.3μm/s (±s.d.) (**Figure 4.2 E**), which is in agreement with previous reports of mRNA transport in epithelial cells (Fusco, Accornero et al. 2003). The mean instantaneous velocity during the entire imaging time period was found to be lower (0.15 μm/s), as would be expected from averaging directed motion and diffusive states. This average velocity over entire particle paths is in good agreement with previous reports of the tracking of IMP1-containing granules (Nielsen, Nielsen et al. 2002). Interestingly, the histogram of the duration of time during which mRNAs displayed directed motion could not be well modeled by a single exponential decay, but rather by a log-normal fit with a median of 1.2s (**Figure 4.2 G**), indicating that active transport of the mRNAs may not follow simple first order kinetics. Segments categorized as passive transport were analyzed by calculating the mean square displacement (MSD) over a moving window and yielded a median apparent diffusion coefficient of 5.3×10^{-3} $\mu m^2/s$ (**Figure 4.2 F**) based on a model of normal diffusion (Saxton and Jacobson 1997).

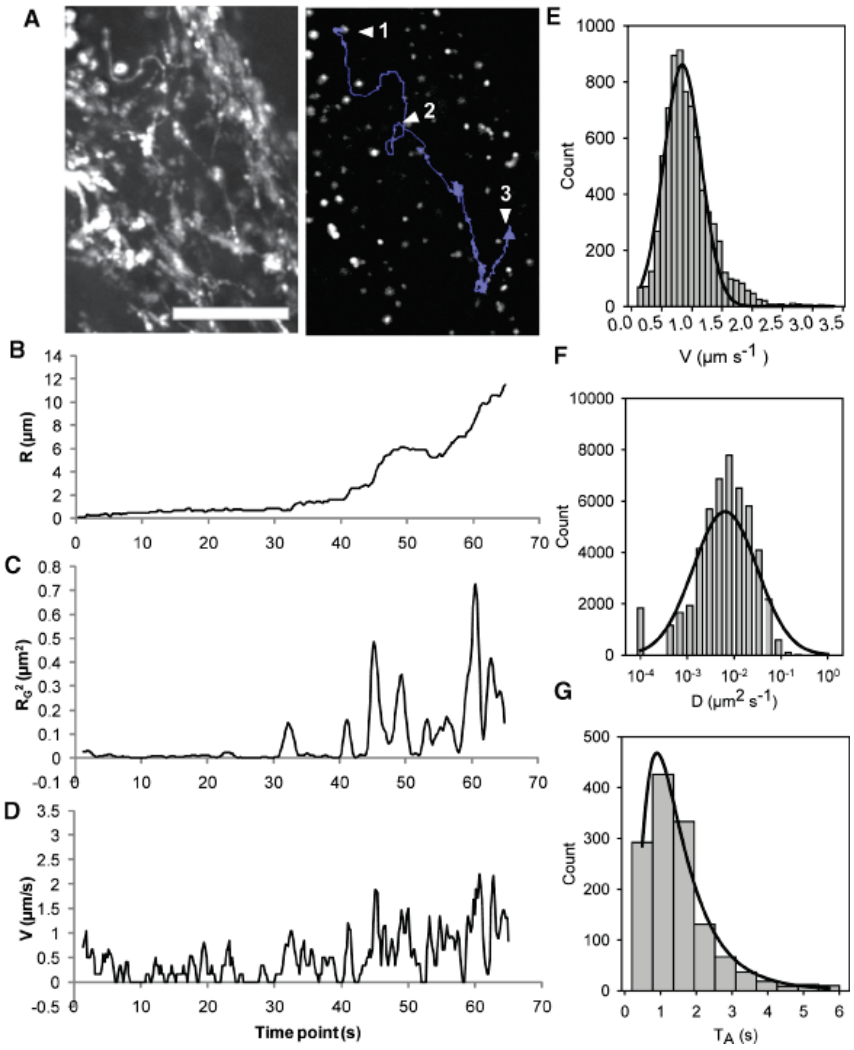

Figure 4.2: SPT analysis of β-actin mRNA in an A549 cell. A) SD map (right) over 120 seconds of imaging and particle track (purple, left) showing a single mRNA granule initial position (1), position at 60 seconds (2) and final position (3); scale bar is 10 μm. B) Overall displacement, (C) square of the radius of gyration determined from a rolling window of 1.6 seconds and (D) instantaneous velocity of the mRNA granule shown in (A) over 60 seconds of analysis. Cumulative histograms calculated from 60 independent particle tracks showing (E) instantaneous velocities during processive motion states (black line is a Gaussian fit), (F) diffusion coefficients during diffusive states calculated over rolling windows of 1.6 seconds (black line is a Gaussian fit), and (G) time duration of processive motion states (black line is a log-normal fit).

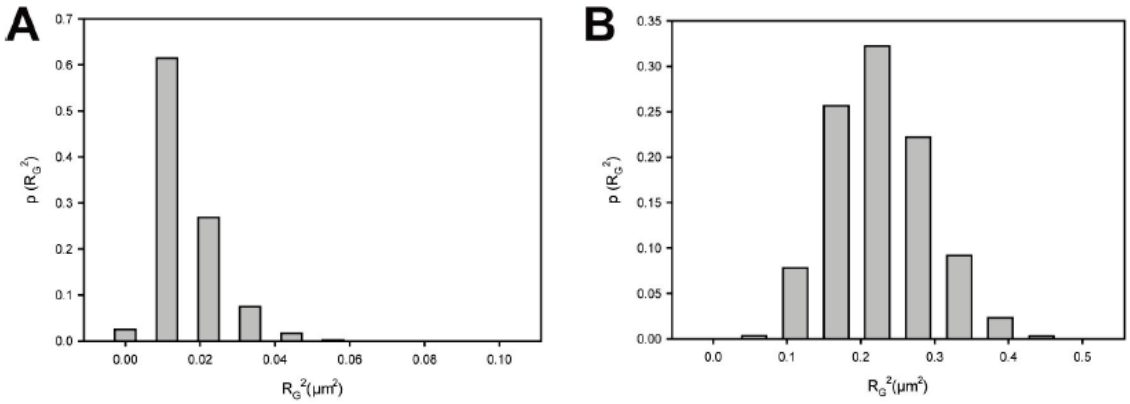

Figure 4.3: Probability distribution function of the radius of gyration R_G^2 from Monte Carlo simulations. (A) normal diffusion ($D=10^{-2}$ μm2 s^{-1}) and (B) diffusion with directed motion ($V=1$ μm s^{-1}). Simulations were performed over windows of 1.6 s.

Analysis of ATP dependent motion

The observed fast, directed motion could either be due to molecular motors that are involved in mRNA transport or to inhomogeneities in the cytoplasm that cause apparent deviations from the stereotypical random walk. In order to demonstrate that the observed fast processive motion is a result of an enzymatically driven process rather than diffusion, mRNAs were tracked at 25ºC or after depletion of ATP. These two experimental conditions were complimentary in that, off target effects were minimized by temperature reduction as there were no drugs used to inhibit the motion and the effect is seen immediately as the cells cool to room temperature, and ATP depletion allowed for imaging at room temperature, so that the cooling of the cytoplasm did not affect the pure diffusion and the effect should be isolated to ATP dependent processes. The analysis of β-actin mRNAs in live cells incubated at 25ºC showed a dramatic decrease in the number of granules undergoing directed motion (**Figure 4.4**) while ATP depletion completely abolished directed motion (**Figure 4.4**). To quantify the reduction in the number of processive motion events seen with temperature reduction, SD maps of independent 5 s intervals were generated and the fraction of mRNA undergoing processive motion during those intervals were counted. The analysis time of 5 s was chosen as it was sufficient for a particle to undergo 1 μm or more of directed transport, which was far enough for an operator to note its presence. Incubation of the cells at 25ºC resulted in an 80% decrease in the fraction of mRNA in processive motion (**Figure 4.5**). The dramatic effect of ATP depletion was confirmed by the SD maps that revealed very little movement both over 5 s and 30 s time scales (**Figure 4.4**). To quantify the treatment's effect on the diffusive transport characteristics, single particle tracking using Volocity's automatic tracking

algorithm was used. Single particle tracking analysis yielded an estimation of apparent diffusion constants of 1.1×10^{-3} $\mu m^2/s$ and 5.8×10^{-5} $\mu m^2/s$ for cells incubated at 25ºC and ATP-depleted respectively (**Figure 4.6**). Both of these treatments were reversible, since removing the metabolic inhibitors or raising the temperature restored directed motion within an hour (**Figure 4.4 & 5** and data not shown). The reversible nature of the treatment is important to note because it suggests that these effects were specific to the treatment and were not the result of the cell undergoing necrosis, apoptosis, or other cell death mechanisms. The observation that directed motion is dramatically decreased in these experimental conditions, as well as the apparent diffusion coefficients, implies that diffusion is not an efficient transport process for mRNAs, probably as a consequence of molecular crowding in the cytoplasm (Luby-Phelps 2000). Indeed, biophysical measurements of the relative diffusivity of synthetic polymers and DNA in the cytoplasm indicate that large structures such as mRNA transport granules will have limited diffusion in this cellular compartment (Seksek, Biwersi et al. 1997; Luby-Phelps 2000; Lukacs, Haggie et al. 2000). Moreover, molecular interactions of constituents of the mRNA granule, such as molecular motors, eEF1 or ZBP1, with the cytoskeleton, may be hindering the ability of the mRNA granules to diffuse freely (Condeelis and Singer 2005). Our data indicate that enzymatically driven, ATP-dependent transport is responsible for the capability of native mRNAs to explore the cytoplasm.

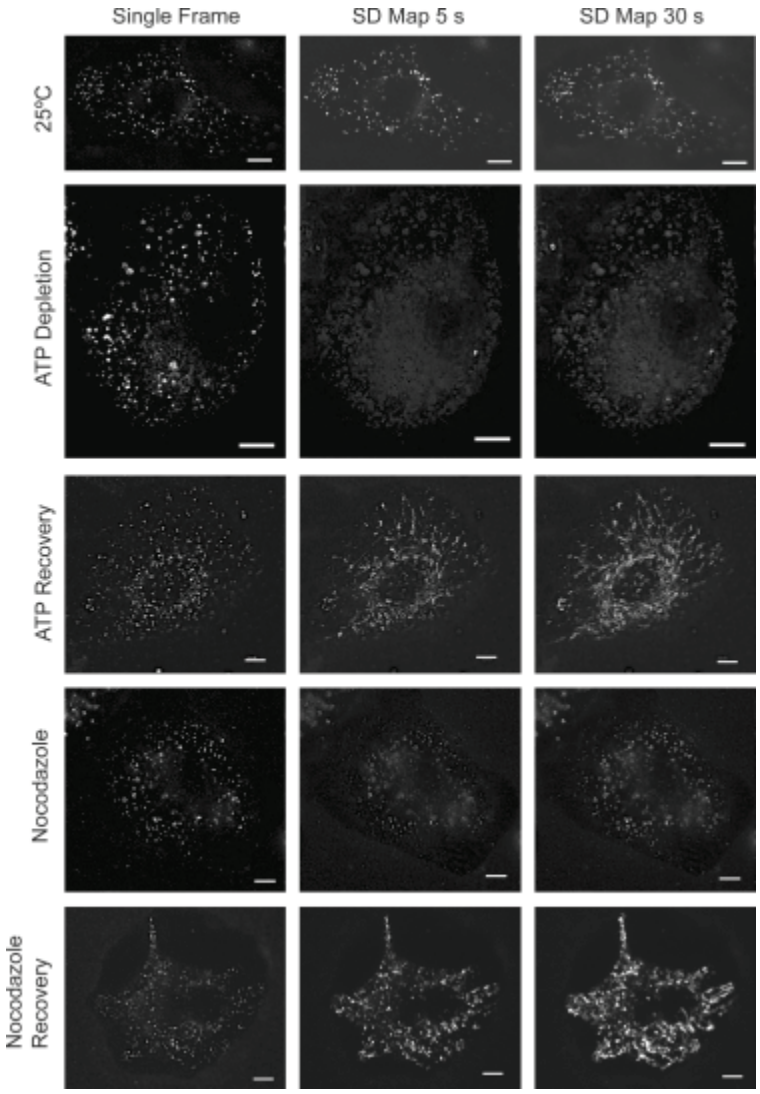

Figure 4.4: β-actin mRNA transport depends on processive, active motion and on microtubules. (Top to bottom rows) Effects of temperature reduction, ATP depletion, recovery from ATP depletion, microtubule disruption via nocodazole, and recovery from nocodazole on mRNA transport. The left column of images shows single frames to demonstrate mRNA distribution. The middle column shows SD maps over 5 seconds of imaging to demonstrate movements over short time scales indicative of processive motion. The right column shows SD maps over 30 seconds of imaging to demonstrate movements over longer time scales. Scale bars are 10 μm.

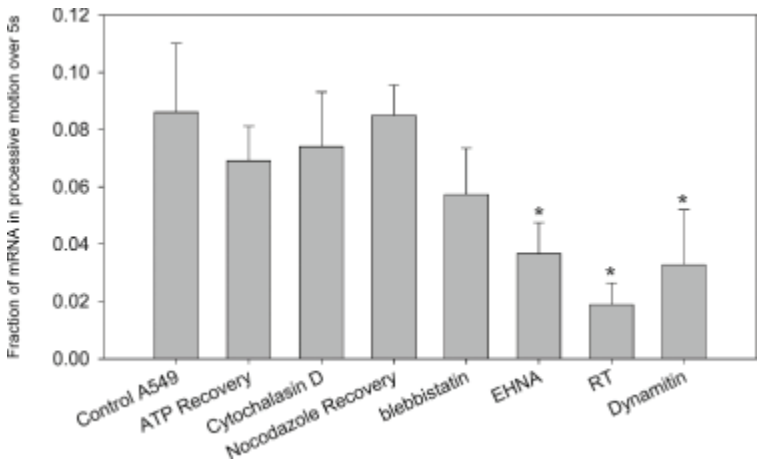

Figure 4.5: Quantification of processive motion. A549 cells were treated with ATP-depleting drugs, microtubule-disrupting drugs (nocodazole), myosin IIB inhibitor (blebbistatin), dynein inhibitor (EHNA), when cells were incubated at room temperature, when cells were recovered from ATP depletion and nocodazole treatment, and when cells were transfected with p50/dynamitin. The fraction of mRNAs undergoing fast motion indicative of motor-driven transport was calculated manually from SD maps generated over 5-second time scales. Error bars are SD. Asterisks denote a statistically significant difference compared with control A549, $p < 0.05$, Kruskal–Wallis analysis of variance.

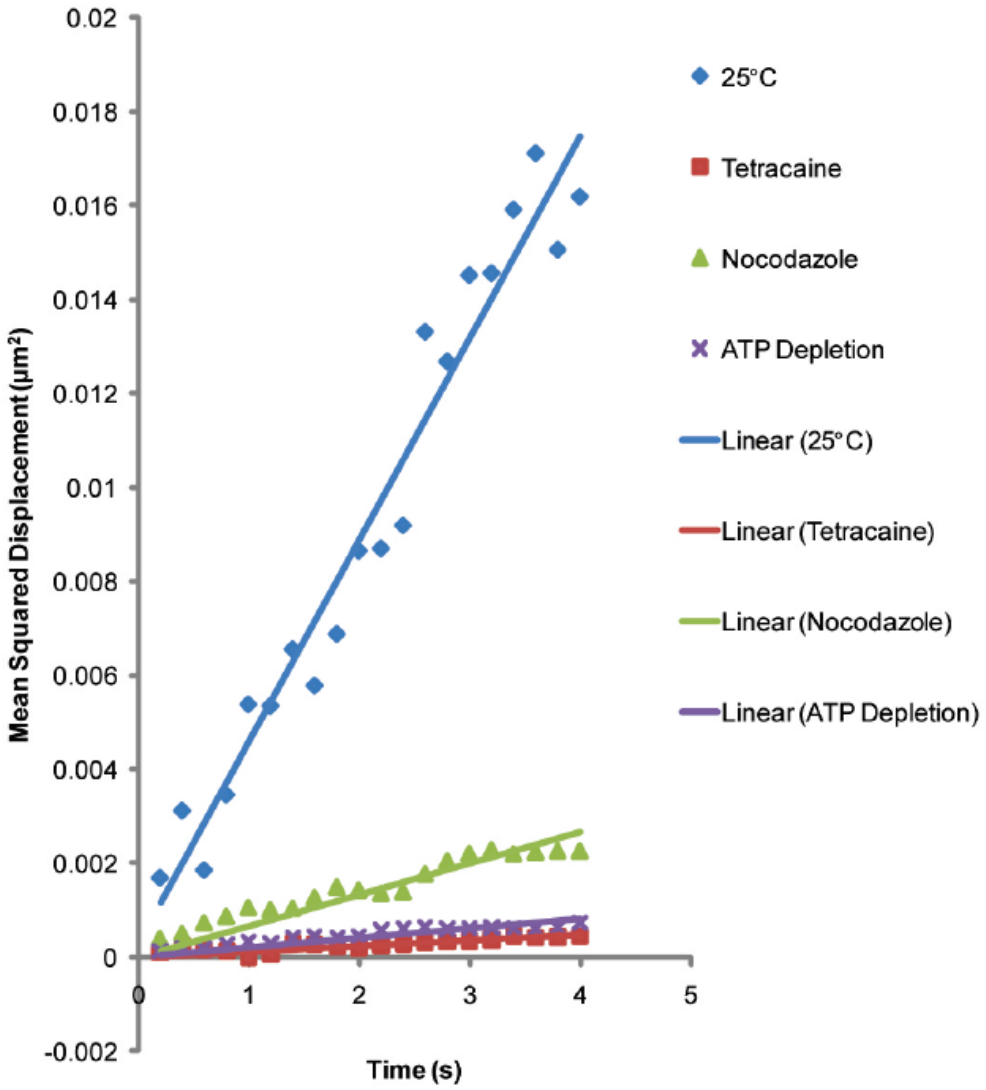

Figure 4.6: MSD from single particle tracking. MSD for experiments in A549s performed at 25°C or in the presence of nocodazole, ATP depletion or tetracaine. Data were fit with linear regressions.

Analysis of cytoskeleton dependent motion

Transport of mRNA in the cytoplasm has previously been shown to depend on either microtubules or actin microfilaments, depending on the specific mRNA and model organism (Jansen 2001). For example, transport of mRNA on actin filaments has been observed for ASH1 mRNA in yeast, while transport in mammalian cells and drosophila embryos has been observed to be driven primarily by kinesin or dynein (Jansen 2001). The localization of β-actin mRNA has been shown to be dependent on actin cytoskeletal filaments in fibroblasts (Sundell and Singer 1991; Latham, Yu et al. 2001) and, while it is hypothesized that transport of β-actin mRNA may occur along actin microfilaments (Latham, Yu et al. 2001), this has not been shown in a live cell. In order to determine the cytoskeletal element required for the transport of β-actin mRNA in A549 epithelial cells we used cytoskeleton disrupting agents to selectively depolymerize the microtubule or actin networks and observe the effects on the observed mRNAs fast directed motion. Disruption of microtubules using nocodazole, confirmed by immunofluorescence (**Figure 4.7**), hindered all mRNA directed motion (**Figure 4.4**). Nocodazole is a widely used microtubule disrupting drug that binds with high affinity to αβ tubulin dimer, though the exact mechanism of depolymerization is unknown. Nocodazole is preferable to use over other microtubule disrupting agents, such as colchicines and vinblastine, as colchicines have several off target effects, such as nucleoside transport inhibition (Berlin 1973; Allison and Davies 1974) and vinblastine results in the formation of paracrystals of tubulin dimers (Xu, Schwarz et al. 2002). Interestingly, β-actin mRNA granules appeared to aggregate after disruption of microtubules (**Figure 4.7 F**). This may be due to the

aggregation of mRNA around islands of microtubules that have not yet depolymerized or are composed of nocodazole resistant tubulin isoforms.

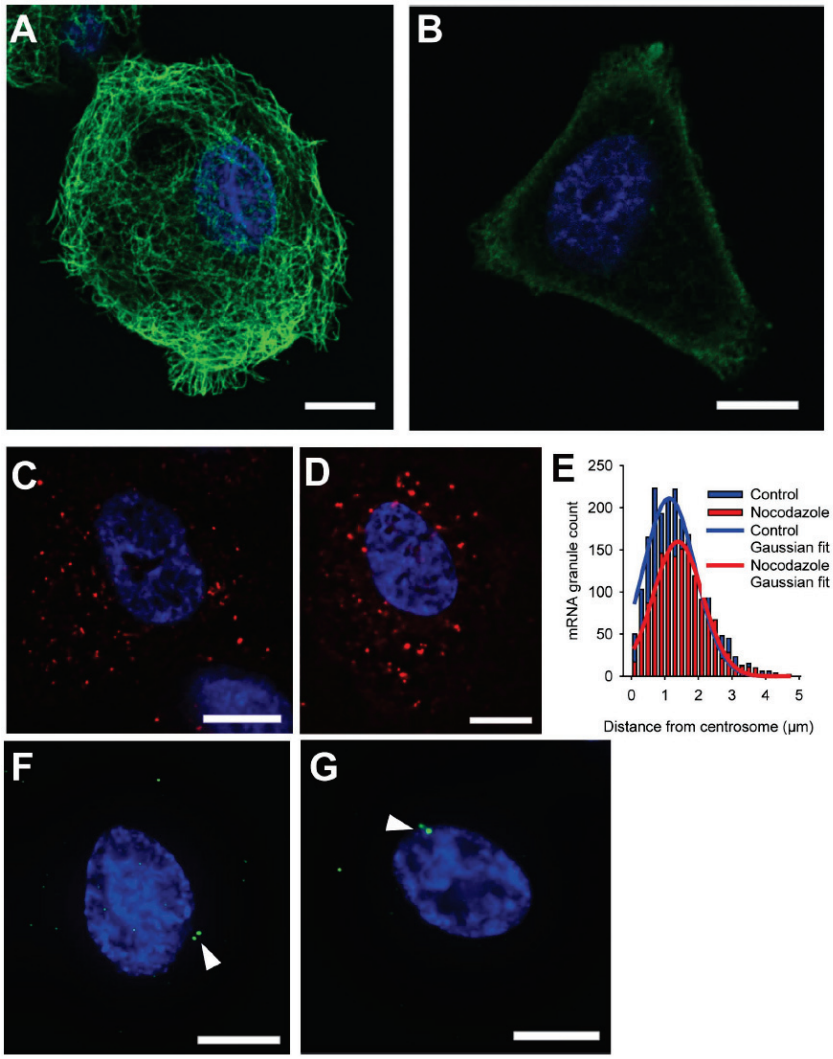

Figure 4.7: Effects of nocodazole mediated microtubule depolymerization.
Microtubule staining in A549 cells untreated (A) and treated with nocodazole (B). Examples of β-actin mRNA (red) distribution in untreated and nocodazole treated cells are shown in C and D respectively. The distribution of mRNA granules with respect to the centrosome (E) was determined by calculating the relative distance of each mRNA granule from the centrosome. The position of the centrosome, visualized by anti γ-tubulin immunostaining (green, see white carrots in F and G), in untreated (F) and nocodazole treated (G) cells relative to the nucleus (blue) is unchanged .Images in (F) and (G) are extended focus projections. Nuclei were stained with DAPI (blue). Scale bars are 10 µm. Images in (A) and (B) are single-plane confocal images. Images in (C) and (D) are single deconvolved planes.

After verifying that nocodazole does not alter centrosomes localization relative to the nucleus within cells (**Figure 4.6 H and I**) we demonstrated that the overall distribution of β-actin mRNA granules relative to the centrosome, was unchanged (**Figure 4.7 G-I**). These controls demonstrate that the nocodazole treatment did not lead to a redistribution of the mRNA granules. Particle tracking yielded an apparent diffusion coefficient of 2.5×10^{-4} $\mu m^2/s$ (**Figure 4.6**). This effect was reversible since removal of nocodazole from the media restored directed movement of mRNA granules (**Figure 4.4** and **Figure 4.5**) in agreement with previous experiments indicating that the loss of directed motion and diffusive mobility was not due to necrosis or apoptosis of the cell. In contrast, treatment with Cytochalasin D did not affect directed motion of mRNA granules despite the dramatic alteration of cell morphology (**Figure 4.8** and **Figure 4.5**). The alteration of cell morphology upon treatment with Cytochalasin D is a known complication (Fusco, Accornero et al. 2003); however, as before, no effect was see upon treatment indicating that the directed motion seen here is not the result of actin dependent molecular motors. Our data indicate that native mRNAs directed motion is dependent on an intact microtubule network and requires ATP.

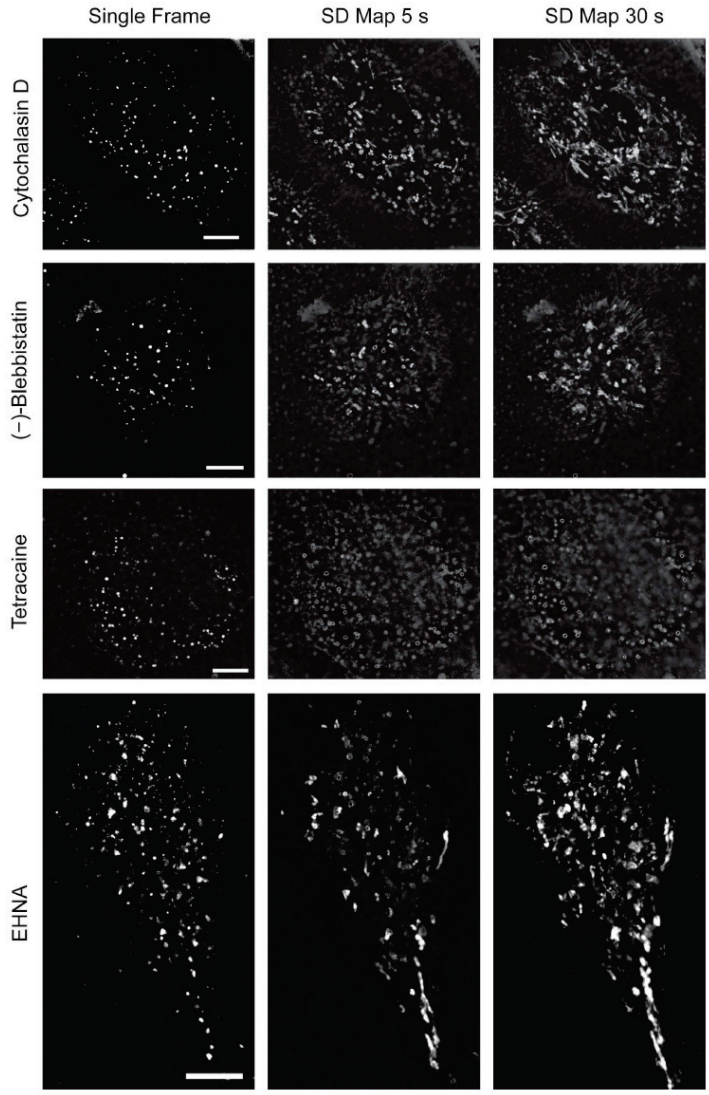

Figure 4.8: β-actin mRNA transport requires molecular motors. (Top to bottom rows) Effects of Cytochalasin D, blebbistatin, tetracaine and EHNA on β-actin mRNA granules motion. Left column of images show single frames to demonstrate mRNA distribution. Middle column shows SD maps over 5 s of imaging to demonstrate movements over time scales indicative of processive motion. Right column shows SD maps over 30 s of imaging to demonstrate movements over longer time scales. Scale bars are 10 μm.

To further verify this, we incubated cells with blebbistatin, which selectively inhibits Myosin II activity (Straight, Cheung et al. 2003), and, as expected, no alteration in mRNAs directed motion was observed (**Figure 4.8** and **Figure. 4.5**). This is in contrast to previous reports that BDM inhibited localization of β-actin mRNA (Latham, Yu et al. 2001). In recent reports, the mechanism of action of BDM had been explored and it has been demonstrated that it is not a specific inhibitor of myosin motors, but rather, it causes the collapse of lamellae altogether (Yarrow, Lechler et al. 2003). However, when cells were treated with tetracaine, a promiscuous inhibitor of molecular motors (Tsuda, Mashimo et al. 1996; Miyamoto, Muto et al. 2000), directed motion was halted within 1 minute, and particle tracking of mRNA granules yielded a diffusion coefficient of 2.5×10^{-5} $\mu m^2/s$ (**Figure 4.6**, **Figure 4.8** and **Figure 4.5**). While the exact mechanism of action of tetracaine on motor proteins is unknown, its effect on motility does not diminish kinesins' or Myosins' ATPase activity and likely acts at the neck region interfering with its forward motion (Yoon, Whipple et al. 2011). It also does not interfere with the binding of the motor protein to its cognate cytoskeletal element. One drawback of tetracaine is it's off target effects including changes in calcium concentrations and neurotransmitter reuptake (Laver and van Helden 2011). However, in the present study neither of these effect are likely to contribute to the phenomena seen here as the changes in calcium concentrations happen at much larger timescales (hours) and neurotransmitter reuptake is unlikely to play any significant role in the physiology of the cell types under investigation. These data suggest that the active, motor driven motion is likely due to microtubule dependent motors. To better characterize this phenomena, we quantified the relative contributions of the microtubule dependent motors, kinesins and dynein, to the

processive motion displayed by β-actin mRNA granules, cells were treated with EHNA, a chemical inhibitor of dynein or were transfected with p50/Dynamitin-GFP, which specifically causes the dissociation of the dynactin complex. EHNA, a structural analogue of adenosine and not ATP, is an allosteric inhibitor of dynein and as such is specific for dynein like ATPases with little to no effect on most other ATPases (Penningroth 1986). EHNA is, however, a potent inhibitor of adenosine deaminase and a mild inhibitor of actin polymerization. While EHNA is a potent and specific inhibitor of dynein, a second treatment, expression of p50/Dynamitin-GFP was used to confirm its effects. p50/Dynamitin inhibits dynein by disrupting the dynein-dynactin complex. Because it was an over expression of a dynactin complex molecule, it was molecularly specific to the dynein-dynactin complex. It was seen that the fraction of mRNA particles in processive motion was reduced by 60% after treatment with EHNA (**Figure 4.8** and Figure 4.5) and after over expression of p50 (**Figure 4.9**) and that this reduction was statistically significant. This suggested that both kinesins and dynein may play a significant role in β-actin mRNA transport and that plus and minus end directed transport occur on microtubules. Further work will be necessary to determine the relative contribution of individual members of the kinesin family to mRNA motion possibly by RNA interference by knocking down individual genes or by inhibition using function blocking antibody or antibody fragments. The data presented above are consistent with the studies of mRNA trafficking in neurons which showed that both kinesin and dynein are responsible for axonal transport (Smith R Neuroscientist 2004). It also shows a possible mechanism for differential localization distinct from that of drosophila embryos, which showed that even though oskar mRNA is differentially transported to the posterior

pole (Zimyanin VL Cell 2008) it is achieved through a polarized microtubule network and not through selective plus or minus end transport. Further work will be needed to see if differential transport has any effect on β-actin mRNA localization or if localization is achieved solely through mRNA trapping at the lamellipodium.

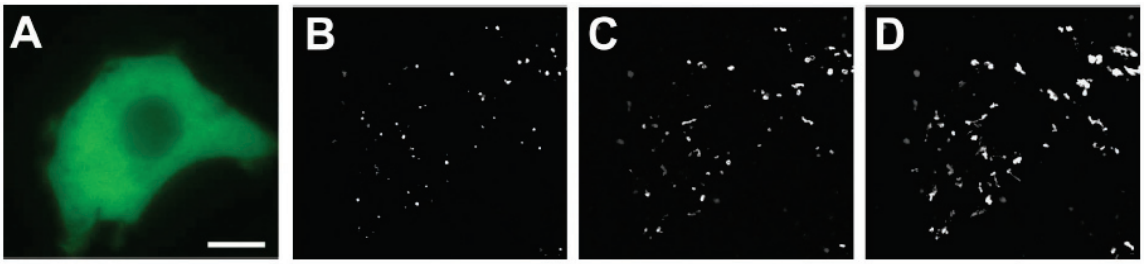

Figure 4.9: β-actin mRNA transport in the presence of p50/dynamitin-GFP. (A) Fluorescence from p50/dynamitin-GFP. (B) Single time point image of fluorescence from Cy3B labeled MTRIPs targeting β-actin mRNA. SD maps over 5 s (C) and 30 s (D) of imaging showing β-actin mRNA transport at shorter and longer time scales. Scale bar is 10 μm, all images are of the same field at the same magnification.

Transport in fibroblasts

To address whether microtubule dependent motion was specific to epithelial cells or if it was a more general mechanism of transport, the movement of β-actin mRNA in primary human dermal fibroblasts (HDFs) was analyzed before and after nocodazole treatment. While the prototypical cell type used for localization of β-actin mRNA has been the chicken embryonic fibroblast, this phenomena has been shown to occur in HDFs, although it occurs in a lesser percentage of cells and to a lesser extent. As in the A549 cells, β-actin mRNA in fibroblasts exhibited motion indicative of molecular motor driven transport. However, in HDFs, the fraction of mRNA granules undergoing processive motion was notably lower than in A549s. To quantify this, the number of mRNA granules undergoing processive motion during independent 5s intervals were counted using SD maps for both A549s and HDFs. In A549s the fraction of mRNA granules undergoing processive motion during a 5s time span was 0.08, for HDFs this was reduced to 0.01 (**Figure 4.10**) ($p<0.05$). As in the A549 cells, processive motion was practically eliminated when the fibroblasts were treated with nocodazole, resulting in no apparent motor driven motion (**Figure 4.10**). Particle tracking of mRNA granules in the nocodazole treated cells yielded an apparent diffusion coefficient of 4×10^{-4} $\mu m^2/s$ similar to the one obtained in A549s. These data suggest that molecular motor transport of β-actin mRNA is driven by microtubule dependent motors in both epithelial cells and fibroblasts and that in neither cell type is there long distance (>10 microns) transport of β-actin mRNA without an intact microtubule network. There are several explanations as to why the fraction of mRNA undergoing directed motion is smaller in HDFs than in A549. However, it is important to note that in fibroblasts, a large percentage of mRNAs

are through to interact with the actin cytoskeleton, particularly at the vertices formed by two actin microfilaments (Bassell 1993). Because motor driven motion of mRNAs occurs primarily on microtubules, it is likely that this fraction is instead anchored to the actin network and is either undergoing translation or is translationally repressed.

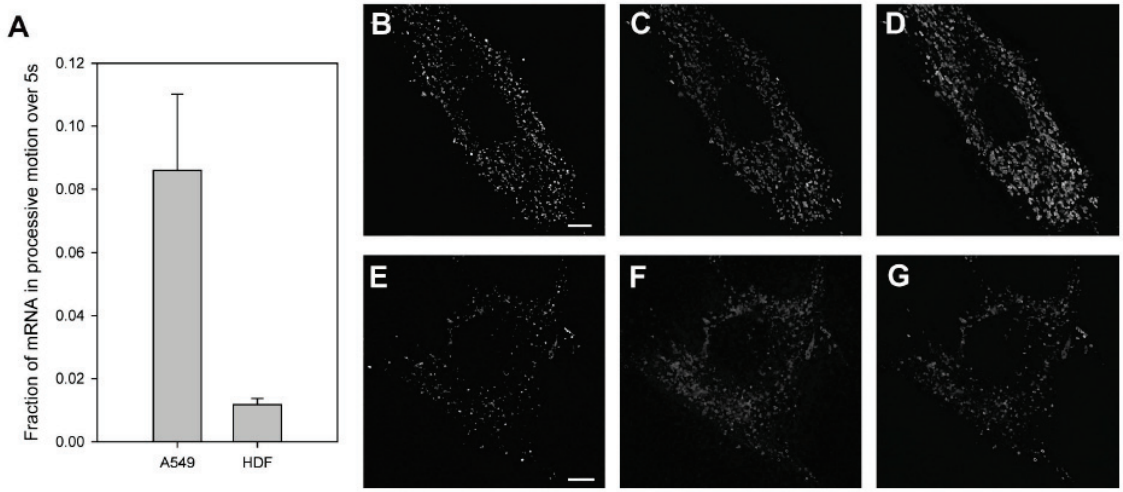

Figure 4.10: Transport of β-actin mRNA transport in fibroblasts is microtubule dependent. (A) Fraction of mRNA granules undergoing processive motion during a 5s window. Error bars are standard deviation. β-actin mRNA transport in fibroblasts under physiological conditions (B-D) and after treatment with nocodazole (E-G). (A, D) are single frames to show mRNA distribution, (C, F) SD maps over 5 s and (D,G) over 30 s of imaging. Scale bars are 10 μm.

Simulated motion

It is important to note that while the fraction of mRNA undergoing directed transport during any given 5s period is low, this transport is intermittent and granules switch between diffusive motion and directed transport. Our data indicate that nearly all mRNA granules will undergo at least one round of directed transport within 60s in A549s and 8 min in HDFs. Furthermore these data clearly indicate that the duration of the experimental time for live cell imaging is crucial when studying these processes. For example, live cell imaging, in an HDF, for 1s would require tracking 500 granules to capture directed motion of 1 mRNA granule. Short imaging times would also adversely affect particle trace segmentation by temporal analysis. This may explain, for instance, why in previous studies of mRNA transport, no motor driven motion was seen. In Yamagishi 2009, imaging was performed for 0.3 s, using the percent of mRNA undergoing directed motion found above, the authors would have had to analyze >1500 granules in order to capture a single one undergoing directed motion during that time period, this would be barely at the detectable limit and due to statistical chance or differences between CEFs and HDFs, may not have occurred at all.

To better demonstrate the effect that intermittent processive motion has on RNA transport, Monte Carlo simulations were used to model diffusion and diffusion with intermittent processive motion. Simulations were performed using a diffusion coefficient of 0.005 $\mu m^2 s^{-1}$ and a velocity of 1 $\mu m\ s^{-1}$ calculated from SPT analysis and over time periods of 5 min and 30 min for comparison with data presented here, and to demonstrate the effect of intermittent processive motion over longer time scales. Probabilities for

switching into an active state were fixed at 0.016 s^{-1}, while probabilities of leaving an active state were dependent upon how long particles were in the state, and were calculated from active state durations from SPT experiments. When RNA transport was simulated over 5 min, median displacement was increased from 1.1 um to 3.8 um (**Figure 4.11** red lines) when intermittent processive motion was added to normal diffusion. More strikingly, when transport was simulated over a 30 min period median displacement increased from 2.6 um to 23 um with the addition of intermittent processive motion (**Figure 4.11** blue lines). These data suggest that for phenomena such as β-actin mRNA localization during cell spreading or induction by serum stimulation, which occur over a time scale of 30 min to 1 hr, diffusion alone is not sufficient to localize the mRNA and that motor driven motion, is necessary to move mRNAs far enough to be captured at the leading edge and that even intermittent motor driven motion is sufficient to give the mRNAs the displacement necessary to localize throughout the cell within 1 hr.

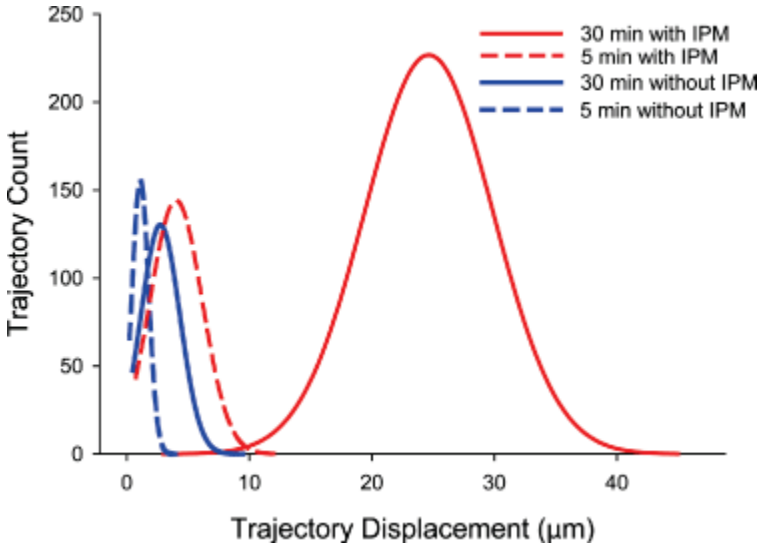

Figure 4.11: Results of a Monte Carlo simulation using models of diffusion with and without intermittent processive motion (IPM). Trajectories were simulated for 5 and 30 min intervals. A diffusion coefficient of 0.005 μm^2/second and a velocity of 1 µm/second were used in the model. Plots shown are Gaussian fits of the histograms of displacements from 1000 trajectories.

Materials and Methods

MTRIPS: MTRIPS were prepared as previously described (Santangelo, Lifland et al. 2009). Briefly, 2'-O-methyl RNA-DNA oligonucleotide chimeras were designed with a 5'-biotin and dT-C6-NH2 internal modifications (Biosearch Technologies, Novato, CA). MTRIPs were assembled by first conjugating either Cy3B-NHS ester fluorophores (GE Heathcare, Buckinghamshire, England) or Dylight 649-NHS ester fluorophores (Pierce, Rockford, IL) to the oligonucleotide amine groups using the manufacturer's protocol. Labeled oligonucleotides were then tetramerized by incubation with Neutravidin (Pierce). MTRIPs targeting different mRNA sequences (**Table 3.2**) were assembled separately prior to delivery.

Cells and Cell Culture: A549 lung carcinoma cells (ATCC, Manassas, VA) and primary human dermal fibroblasts (Lonza, Basel, Switzerland) were maintained in High Glucose DMEM (Lonza, Basel, Switzerland) with 10% fetal bovine serum (Hyclone, Logan, UT), 100 U ml^{-1} penicillin, and 100 μg ml^{-1} streptomycin (Invitrogen, Carlsbad, CA). Cells were plated one day prior to imaging.

Probe Delivery: For probe delivery, cells were washed in DPBS (Lonza) -Ca^{2+} -Mg^{2+}, and then incubated 0.2U ml^{-1} activated streptolysin-O (SLO) (Sigma) in OptiMEM (Invitrogen) containing 15nM of each MTRIP for 10 min at 37ºC. Delivery media was replaced with growth media for 15 min to restore membrane integrity before live cell imaging or fixation.

Drugs: After probe delivery, cells were incubated for 1 hr in glucose free DMEM (Invitrogen) containing 60 mM 2-deoxy-d-glucose (2DG) (CalBioChem, San Diego, CA) and 10 mM sodium azide (NaN_3) (VWR, West Chester, PA) for ATP depletion, for 90 min with 1 μM cytochalasin D (Sigma) for actin depolymerization, for 90 min with 4 μM nocodazole (Sigma) for microtubule depolymerization, and for 15 min with 1 mM erythro-9-(2-Hydroxy-3-nonyl)-adenine hydrochloride (EHNA) (Sigma). After incubation, live cell imaging was performed in Leibovitz L15 media supplemented with the appropriate drug. Drug recovery was achieved by replacing the drug-containing media with growth media. Tetracaine (Sigma) and blebbistatin (Sigma) were used at 100 μM and 50 μM in Leibovitz L15 media respectively and cells were imaged immediately.

p50/Dynamitin-GFP expression: A plasmid expressing p50Dynamitin-GFP (supplied by Dr. Richard Vallee) was transfected into A549 cells using the Neon Transfection System (Invitrogen) following the manufacturers' protocol for 10μl electroporation volumes. Assays were carried out 24 hrs post-transfection in cells exhibiting GFP florescence indicative of efficient transfection and exhibiting normal cellular morphology.

Fixed and Live Cell Microscopy: For live cell Imaging, cells were plated in Bioptechs T4 plates (Bioptechs, Butler, PA) and growth media was replaced with Leibovitz L15 CO_2 independent media (Invitrogen) supplemented with 10% FBS for live cell imaging. Bioptechs dishes were maintained at 37ºC using a Bioptechs Delta T system and an objective heater. For fixed cell imaging, cells were grown on No. 1.5 coverslips and fixed and immunostained after delivery of MTRIPS. Images were taken on an Axiovert 200M

microscope (Zeiss, Oberkochen, Germany) with a 63x NA 1.4 Plan Apochromat primary objective and an ORCA-ER AG camera (Hamamatsu, Hamamatsu City, Japan). For ethidium bromide exclusion assays, a 20x NA 0.4 Plan Neofluar was used. Fluorescent filter sets used were 49004 ET-Cy3 for live cell imaging and 89000 Sedat Quad - ET for multiple wavelength imaging (Chroma, Bellows Falls, VT). All imaging experiments were performed using the Volocity acquisition software (Improvision, Waltham, MA). Image stacks were recorded at 200nm intervals for fixed cell samples to adequately sample volumes for iterative deconvolution.

Confocal Imaging: Images were captured on a Zeiss LSM 510 Meta using a 63x, NA 1.4 Plan-Apochromat objective. Resolution was set to 1024x1024. Files were imported into Volocity and linearly contrast enhanced for display.

Image Processing and analysis: All live and fixed cell images were deconvolved using Volocity's deconvolution algorithms. Image Z-stacks were deconvolved using iterative restoration and live cell movies were deconvolved using fast restoration. Granule counting and intensity quantification as well as Manders' and Pearson's coefficients were computed in Volocity and imported into Excel (Microsoft, Redmond, WA) or Sigma Plot (Systat, Chicago, IL for plotting. Kruskal–Wallis and ANOVA statistical tests were performed in MATLAB (The MathWorks, Natick, MA) or Sigma Plot. Images presented have been linearly contrast enhanced for clarity. All calculations were performed directly on unenhanced, deconvolved data. Standard deviation maps were computed using the ZProject plugin for NIH ImageJ on deconvolved image sets exported in Tiff format. Intensity profile plots were generated in ImageJ using the RGB profiler plugin.

Two dimensional random walk simulations with and without directed motion were performed in MATLAB using a fixed step size and a random angle. For threshold determination in SPT experiments a diffusion constant of $1x10^{-2}$ $\mu m^2/s$ and a velocity of 1 μm/s for directed motion was selected to ensure accurate discrimination between diffusive states and processive motion.

Mean square displacements were calculated by averaging independent particle tracks and by averaging independent time windows within tracks. Linear fitting was performed in Excel.

Single particle tracking: Single particle tracking was performed in Volocity. For experiments performed at 25ºC or in the presence of tetracaine, nocodazole, or ATP depletion drugs, mRNA granules were tracked automatically using Volocity's tracking algorithms. For all other experimental conditions, tracking was performed manually using Volocity's manual tracking. Rolling window temporal analysis was performed in MATLAB with custom routines. Histograms were generated in Sigma Plot. Preliminary analysis was performed using a two parameter joint probability distribution (radius of gyration and eigen value ratio) to discriminate diffusive states and processive motion. However, the eigen value ratio was found to be unnecessary and for simplification only the radius of gyration was subsequently used.

Conclusions and summary

We have described here the microtubule-dependent transport of native β-actin mRNAs in the cytoplasm of epithelial cells and fibroblasts. In both cell lines, transport

was shown to be processive and occurred intermittently over 5 minutes. Without an intact microtubule network, mRNA motion was dramatically impaired, indicating that diffusion is unlikely a biologically relevant mechanism for mRNA granule transport in the cytoplasm. While this is predicted from previously published biophysical measurements of macromolecules of similar size and molecular weight as mRNA, controversy still exists on the importance of diffusion in mRNA localization (Yamagishi, Ishihama et al. 2009; Yamagishi, Shirasaki et al. 2009; Ben-Ari, Brody et al. 2010).

Interestingly, the experiments performed with nocodazole, with ATP-depletion compounds and tetracaine in A549 cells, not only eliminated processive motion of β-actin mRNA, but also yielded consistently lower apparent diffusion coefficients than those performed in control conditions. This suggests that non-processive mRNA transport may be the result of a superposition of diffusion, cytoskeletal remodeling, and indirect action of molecular motors on the adjacent cytoplasm. These factors have been proposed to have a significant effect on large particles (such as vesicles) attached to the cytoskeleton (Brangwynne, Koenderink et al. 2009) but have not, as of yet, been reported to effect the transport of mRNA.

The use of MTRIPs in imaging native mRNA in live cells has many advantages, such as the probes are bright and can achieve single-molecule sensitivity, they are sufficiently photo-stable for single particle tracking over relevant time scales, and they can be used simultaneously with fluorescent proteins in live cells. MTRIPs are not only specific, but they do not significantly increase the molecular weight or size of an mRNA granule. However, certain considerations must be taken into account when using

MTRIPs. MTRIPs bind to native mRNA sequences and, therefore, care must be taken in the selection of their sequences to avoid blocking of RNA binding protein sites. Careful thresholding of fluorescence intensity against unbound probes is also necessary to exclude background from analysis, as MTRIPs are not fluorogenic but are particularly bright. Finally, there is still little information on the effect of MTRIPs on RNA stability and decay. For long half-life mRNA, such as β-actin, such effects are minimized, but it may be an important consideration in studies on shorter lived mRNAs.

References

Allison, A. C. and P. Davies (1974). "Mechanisms of endocytosis and exocytosis." Symp Soc Exp Biol(28): 419-446.

Anderson, P. and N. Kedersha (2009). "RNA granules: post-transcriptional and epigenetic modulators of gene expression." Nat Rev Mol Cell Biol **10**(6): 430-436.

Arcizet, D., B. Meier, et al. (2008). "Temporal analysis of active and passive transport in living cells." Phys Rev Lett **101**(24): 248103.

Bassell, G. J. (1993). "High resolution distribution of mRNA within the cytoskeleton." J Cell. Biochem. **52**: 127-133.

Ben-Ari, Y., Y. Brody, et al. (2010). "The life of an mRNA in space and time." J Cell Sci **123**(Pt 10): 1761-1774.

Berlin, R. D. (1973). "Temperature dependence of nucleoside membrane transport of rabbit alveolar macrophages and polymorphonuclear leukocytes." J Biol Chem **248**(13): 4724-4730.

Bertrand, E., P. Chartrand, et al. (1998). "Localization of ASH1 mRNA particles in living yeast." Mol Cell **2**(4): 437-445.

Brangwynne, C. P., G. H. Koenderink, et al. (2009). "Intracellular transport by active diffusion." Trends Cell Biol **19**(9): 423-427.

Cai, D., D. P. McEwen, et al. (2009). "Single molecule imaging reveals differences in microtubule track selection between Kinesin motors." PLoS Biol **7**(10): e1000216.

Cai, D., K. J. Verhey, et al. (2007). "Tracking single Kinesin molecules in the cytoplasm of mammalian cells." Biophys J **92**(12): 4137-4144.

Condeelis, J. and R. H. Singer (2005). "How and why does beta-actin mRNA target?" Biol Cell **97**(1): 97-110.

Delanoue, R. and I. Davis (2005). "Dynein anchors its mRNA cargo after apical transport in the Drosophila blastoderm embryo." Cell **122**(1): 97-106.

Fusco, D., N. Accornero, et al. (2003). "Single mRNA molecules demonstrate probabilistic movement in living mammalian cells." Curr Biol **13**(2): 161-167.

Hachet, O. and A. Ephrussi (2004). "Splicing of oskar RNA in the nucleus is coupled to its cytoplasmic localization." Nature **428**(6986): 959-963.

Holt, C. E. and S. L. Bullock (2009). "Subcellular mRNA localization in animal cells and why it matters." Science **326**(5957): 1212-1216.

Jansen, R. P. (2001). "mRNA localization: message on the move." Nat Rev Mol Cell Biol **2**(4): 247-256.

Johnsson, A. K. and R. Karlsson (2010). "Microtubule-dependent localization of profilin I mRNA to actin polymerization sites in serum-stimulated cells." Eur J Cell Biol **89**(5): 394-401.

Latham, V. M., E. H. Yu, et al. (2001). "A Rho-dependent signaling pathway operating through myosin localizes beta-actin mRNA in fibroblasts." Curr Biol **11**(13): 1010-1016.

Laver, D. R. and D. F. van Helden (2011). "Three independent mechanisms contribute to tetracaine inhibition of cardiac calcium release channels." J Mol Cell Cardiol **51**(3): 357-369.

Luby-Phelps, K. (2000). "Cytoarchitecture and physical properties of cytoplasm: volume, viscosity, diffusion, intracellular surface area." Int Rev Cytol **192**: 189-221.
Lukacs, G. L., P. Haggie, et al. (2000). "Size-dependent DNA mobility in cytoplasm and nucleus." J Biol Chem **275**(3): 1625-1629.
Martin, K. C. and A. Ephrussi (2009). "mRNA localization: gene expression in the spatial dimension." Cell **136**(4): 719-730.
Miyamoto, Y., E. Muto, et al. (2000). "Direct inhibition of microtubule-based kinesin motility by local anesthetics." Biophys J **78**(2): 940-949.
Nielsen, F. C., J. Nielsen, et al. (2002). "Cytoplasmic trafficking of IGF-II mRNA-binding protein by conserved KH domains." J Cell Sci **115**(Pt 10): 2087-2097.
Penningroth, S. M. (1986). "Erythro-9-[3-(2-hydroxynonyl)]adenine and vanadate as probes for microtubule-based cytoskeletal mechanochemistry." Methods Enzymol **134**: 477-487.
Santangelo, P. J., A. W. Lifland, et al. (2009). "Single molecule-sensitive probes for imaging RNA in live cells." Nat Methods **6**(5): 347-349.
Saxton, M. J. (1994). "Single-particle tracking: models of directed transport." Biophys J **67**(5): 2110-2119.
Saxton, M. J. and K. Jacobson (1997). "Single-particle tracking: applications to membrane dynamics." Annu Rev Biophys Biomol Struct **26**: 373-399.
Seksek, O., J. Biwersi, et al. (1997). "Translational diffusion of macromolecule-sized solutes in cytoplasm and nucleus." J Cell Biol **138**(1): 131-142.
Straight, A. F., A. Cheung, et al. (2003). "Dissecting temporal and spatial control of cytokinesis with a myosin II Inhibitor." Science **299**(5613): 1743-1747.
Sundell, C. L. and R. H. Singer (1991). "Requirement of microfilaments in sorting of actin mRNAs." Science **253**: 1275-1277.
Tsuda, Y., T. Mashimo, et al. (1996). "Direct inhibition of the actomyosin motility by local anesthetics in vitro." Biophys J **71**(5): 2733-2741.
Wilkie, G. S. and I. Davis (2001). "Drosophila wingless and pair-rule transcripts localize apically by dynein-mediated transport of RNA particles." Cell **105**(2): 209-219.
Xu, K., P. M. Schwarz, et al. (2002). "Interaction of nocodazole with tubulin isotypes." Drug Development Research **55**(2): 91-96.
Yamagishi, M., Y. Ishihama, et al. (2009). "Single-molecule imaging of beta-actin mRNAs in the cytoplasm of a living cell." Exp Cell Res **315**(7): 1142-1147.
Yamagishi, M., Y. Shirasaki, et al. (2009). "Size-dependent accumulation of mRNA at the leading edge of chicken embryo fibroblasts." Biochem Biophys Res Commun **390**(3): 750-754.
Yarrow, J. C., T. Lechler, et al. (2003). "Rapid de-localization of actin leading edge components with BDM treatment." BMC Cell Biol **4**: 5.
Yoon, J. R., R. A. Whipple, et al. (2011). "Local anesthetics inhibit kinesin motility and microtentacle protrusions in human epithelial and breast tumor cells." Breast Cancer Res Treat **129**(3): 691-701.
Zimyanin, V. L., K. Belaya, et al. (2008). "In vivo imaging of oskar mRNA transport reveals the mechanism of posterior localization." Cell **134**(5): 843-853.

CHAPTER 5

TARGETING THE VIRAL GENOMIC RNA OF HRSV

Background

The imaging and tracking of cellular mRNAs can be a powerful tool in the elucidation of mRNA transport mechanisms and post-transcriptional gene regulation. However, the utility of tracking RNAs in live cells can extend beyond the study of cellular RNA. The study of viral genomic RNA of RNA viruses could also benefit from technologies that allow for the accurate localization of native RNA sequences in the cytoplasm of live cells (Pederson 2001; Brandenburg, Lee et al. 2007; Brandenburg and Zhuang 2007; Santangelo and Bao 2007; Tilsner and Oparka 2010). As in the case of cellular RNAs, a model system for viral RNA localization is needed. The viral genomic RNA of human respiratory syncytial virus (hRSV) was chosen as it has several properties that make it amenable to study by MTRIP probes. First, as a negative sense single stranded RNA virus, the genomic RNA of hRSV is encapsidated by the viral nucleocapsid (N) protein (Tawar, Duquerroy et al. 2009). This encapsidation allowed for the colocalization of the MTRIP signal with immunofluorescence for hRSV N. Second, as a single stranded RNA virus, the genomic sequence is open to binding by oligonucleotide probes. While it is possible that the N protein may block binding of oligonucleotides to the base paring region of the genomic RNA, hRSV N has been show to bind to the backbone and not nitrogenous bases of the RNA (Tawar, Duquerroy et al. 2009). Lastly, hRSV forms morphologically distinct structures, inclusion bodies and viral

filaments, which are amenable to microscopic analysis (Norrby, Marusyk et al. 1970; Ghildyal, Mills et al. 2002).

hRSV genomic RNA targeting and signal discrimination

MTRIPs ligands targeted against the hRSV genomic RNA were designed to bind to a gene-end-intergenic-gene-start sequence which has three exact repeats in the hRSV genome. These repeats allowed for increased signal to background without the use of additional probe sequences, as was the case for β-actin mRNA targeted probes. Additionally, the natural accumulation of genomic RNA into inclusion bodies also served to increase the signal from the hRSV targeted MTRIPs above the background. As an initial test to see whether or not these probes could be used to image the genomic RNA, MTRIPs at a concentration of 30 nM were delivered into live A549 cells infected with hRSV stain A2 24 hours post infection (hpi). As can be seen (**Figure 5.1**) the signal from the MTRIP probes can be seen in infected cells while, when imaged under the same conditions, the mock infected case displayed no signal. Immunostaining for the hRSV N protein in these cells demonstrated that the genomic RNA and N protein were well colocalized (Manders' overlap of 0.65). Intensity line profiles also showed good correlation between the genomic RNA granules and the n protein granules.

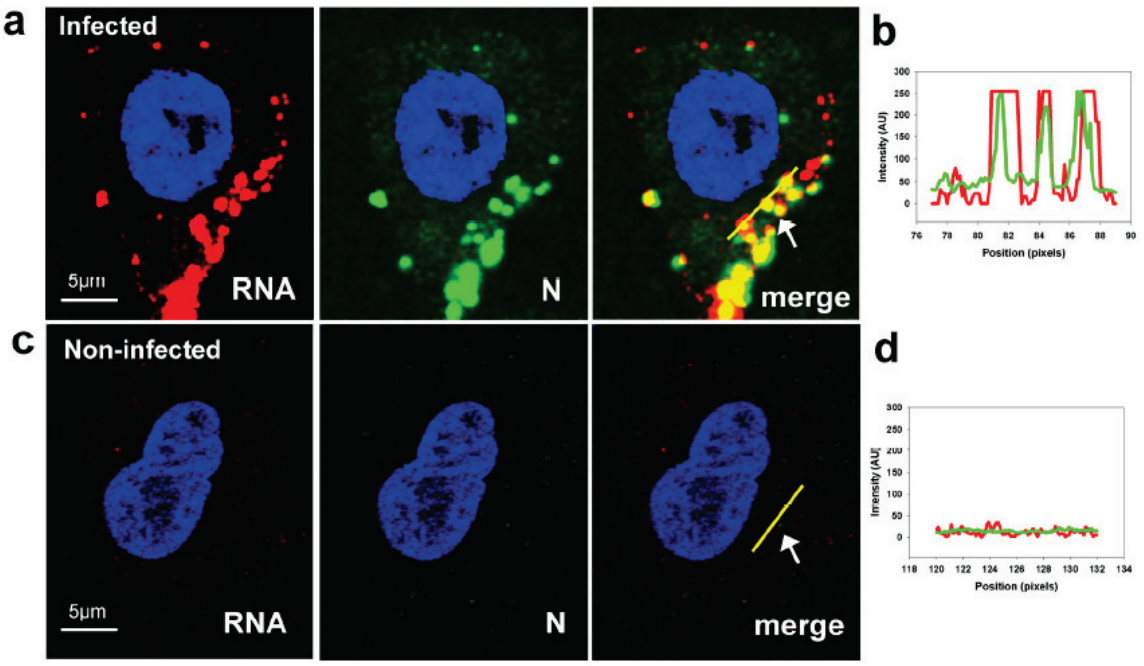

Figure 5.1: Validation of hRSV-targeted MTRIP specificity. (a,b) MTRIPs targeted the viral genomic RNA of hRSV (red) and colocalized (yellow) with hRSV nucleocapsid protein (green) in infected cells. DAPI staining (blue) stains the nucleus of the cell. (c,d) Little background was observed in non-infected cells. Colocalization was observed in the images, and quantified in intensity profiles along the yellow line, denoted by the white arrow.

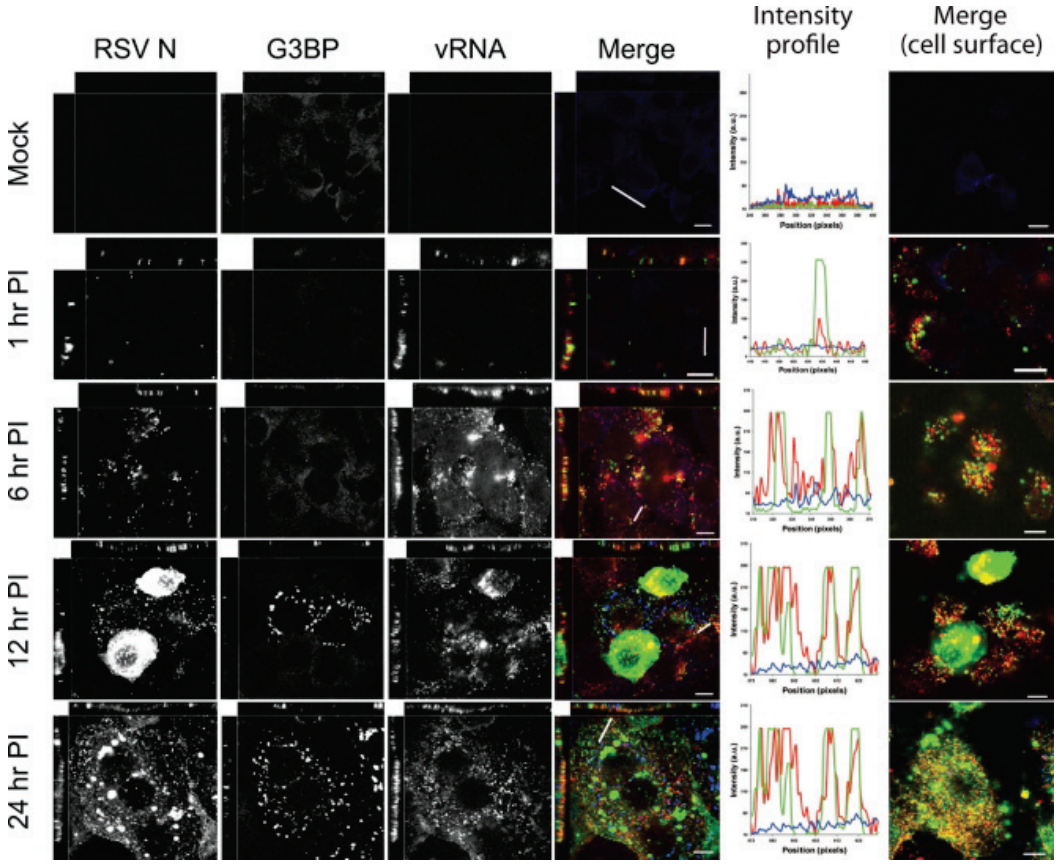

Figure 5.2: Viral genomic RNA predominantly colocalizes with RSV inclusion bodies. HEp-2 cells were mock-infected or infected with RSV (MOI = 1) for the indicated times. RSV RNA-specific probes were added as described in Materials and Methods. Cells were fixed and processed for immunofluorescence. Anti-RSV N was used as an inclusion body marker and appears green in the merged image. Anti-G3BP was used as a stress granule marker and appears blue in the merged image. RSV RNA (vRNA) appears red in the merged image (fourth column). The main images are xy cross sections, and the images above and to the left represent xz and yz cross sections, respectively. The horizontal lines are scale bars, while the diagonal or vertical lines were used to calculate the intensity profiles. Intensity profiles at each time point demonstrate the strong correlation between the N protein and viral genomic RNA (fifth column). Images of N (green), viral genomic RNA (red), and G3BP (blue) in mock infection and at 1, 6, 12, and 24 h postinfection at an image plane near the cell surface are in the sixth column. PI, postinfection; a.u., arbitrary units.

Localization over the time course of infection

To better understand the localization of the genomic RNA of hRSV during different times after infection, HEp-2 cells were infected and at 1, 6, 12, and 24 hpi MTRIPs targeting hRSV genomic RNA was delivered into the cells and the cells were subsequently fixed 15 min post delivery. The cells were then immunostained for the hRSV N protein to identify inclusion bodies and for G3BP to identify stress granules, which have been implicated in the regulation of viral RNAs (**Figure 5.2**). Mock infection showed no signal above background for the RNA, N and G3BP staining. At 1 hpi, Viral RNA was seen localized to small granules near the plasma membrane of the cells. These granules colocalized with the N protein staining. No stress granules were present. At 6 hpi these RNA granules were more numerous, larger and continued to colocalize with the N protein. No stress granules were seen at this time point. At 12 hpi, the viral RNA granules had become so numerous and large those individual granules were hard to detect and fluorescence signal was seen as continuous in some regions. The RSV N staining was even more dramatic as many cells appeared completely filled by the N protein. At this time point stress granules began to appear. While not dramatic, some viral RNAs can be seen localizing to the stress granules. At 24 hpi syncytia began to form and viral RNA could be seen localized both the inclusion bodies and to viral filaments. Stress granule positive cell were more abundant; however, only a small fraction of genomic RNA colocalized with them. To more quantitatively assess the colocalization of viral genomic RNA with stress granules and inclusion bodies, data was imported into Volocity software and the Manders' overlap coefficients were calculated on the reconstructed 3D data (**Table 5.1**).

Table 5.1 RSV RNA is predominantly associated with viral inclusion bodies.

Pair of structures analyzed	% Colocalization at time (h) postinfection		
	1	**12**	**24**
Viral RNA + inclusion bodies	87	96	91
Viral RNA + stress granules	0	2.2	4.5
Inclusion bodies + stress granules	0	1.6	3.4

hRSV and colocalization with stress granules in live cells

To test the utility of these probes for the study of RNA-protein colocalization in live cells, we used Cy3B-labeled MTRIPs targeted to the genomic RNA of hRSV in conjunction with a GFP–TIA-1 fusion protein in infected A549 cells, to evaluate the interaction between the stress granule protein TIA-1 and hRSV viral RNA when stress granules were induced by sodium arsenite treatment. Previous findings demonstrated that paramyxovirus RNA, which contains many possible TIA-1 or TIAR binding sites (uracil-rich regions), likely interacts with stress granules(Iseni, Garcin et al. 2002); this interaction though, has not been characterized in living cells. In hRSV-infected cells transfected with GFP–TIA-1, stress granules had not formed 24 h after infection as identified by the lack of aggregation of GFP–TIA-1 in cells also containing viral RNA (**Figure 5.3a**). MTRIPs were specific and did not aggregate RNA (**Figures 5.1, 5.4, 5.5**).

To induce stress granules, we exposed the cells to 1.0 mM sodium arsenite (Kedersha, Chen et al. 2002) and observed substantial transient interactions between stress and viral RNA granules **Figure 5.3b-d**. We observed a stress granule moving into a viral RNA granule and residing within it for over a minute before it was released (**Figure 5.3b-d** and **Videos 7** and **8**). Another stress granule then appeared to dock with a viral RNA granule (**Figure 5.3b-d** and **Video 9**), and appeared to be in contact for approximately 45 s. Transient interactions between RNA granules on the same time scales had been reported, supporting our observations, but previously engineered RNAs or proteins were imaged, in contrast to the non-engineered RNAs imaged in this study (Kedersha, Stoecklin et al. 2005; Mollet, Cougot et al. 2008; Zeitelhofer, Karra et al. 2008). We also observed more stable interactions between GFP–TIA-1 and the viral

RNA (**Figure 5.6** and **5.7** and **Videos 10** and **11**). Notably, the time-lapse results we present here cannot be obtained using probes that require high (micromolar) probe concentrations and have lower sensitivity. The use of less-sensitive probes would result in large RNA-protein exposure time mismatches, resulting in the inability to track the interaction of individual granules accurately.

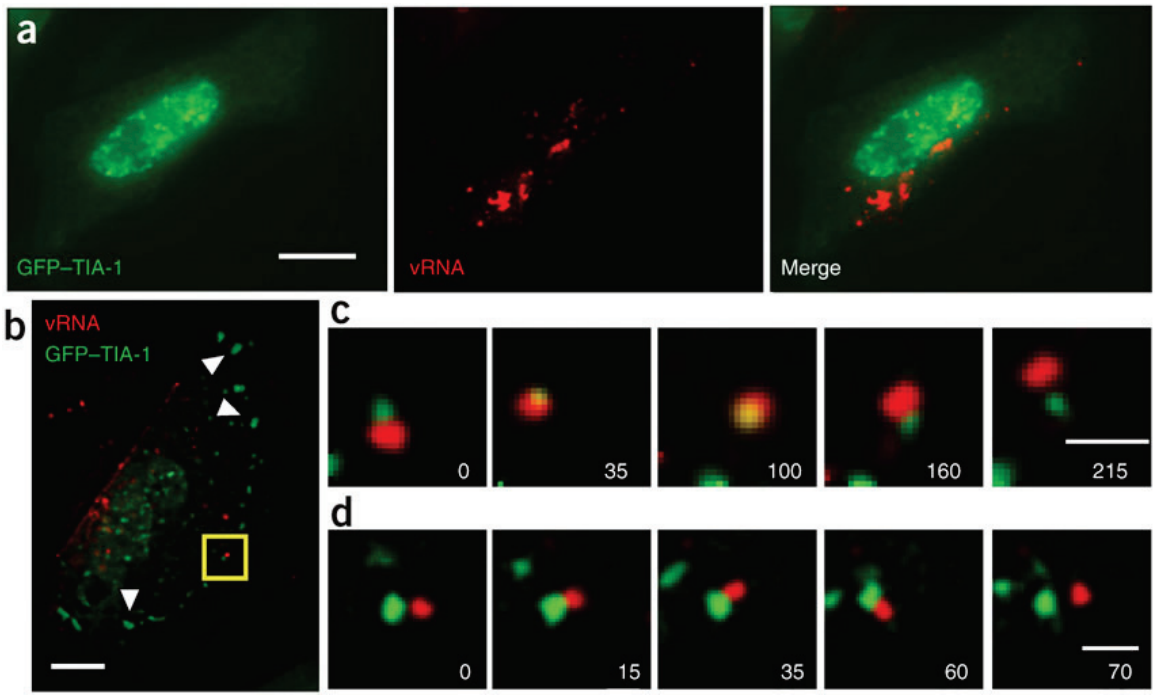

Figure 5.3: hRSV vRNA interaction with SG in a live cell. (a) Fluorescence images of a live A549 cell imaged 24 h after infection and 48 h after transfection, showing no stress granules. (b) Live-cell image of a single optical plane of GFP–TIA-1 and Cy3B-labeled hRSV-targeted MTRIPs (25 nM) in an A549 cell, 24 h after infection, 48 h after transfection and 20 min after exposure to 1 mM sodium arsenite. Arrowheads denote stress granules. (c) Time-lapse images of stress granule (green) collision, penetration and separation of a viral RNA granule (red). (d) Images of the docking of a stress and viral RNA granule, which occurred for only 45 s before separation. All granule interactions shown were imaged in the area denoted by the box in b. All times are given in seconds. Scale bars, 10 m (a,b) and 1 m (c,d).

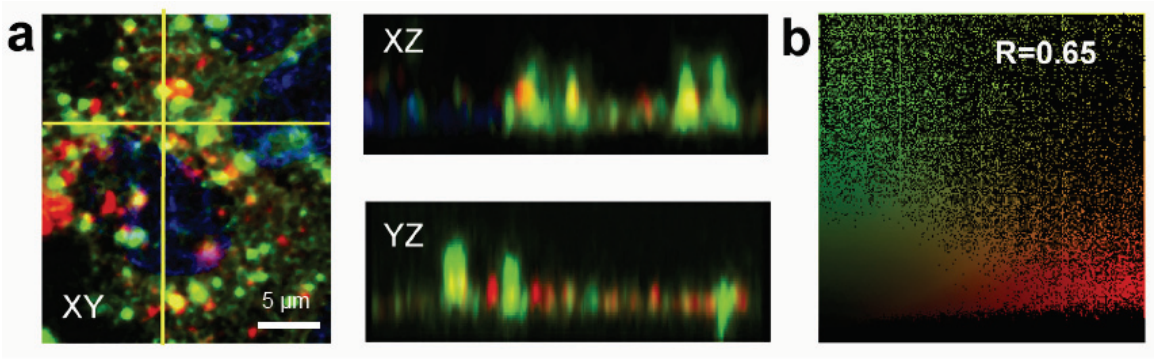

Figure 5.4: hRSV vRNA colocalization with N protein in 3D. Quantification of 3D colocalization of MTRIP targeted to hRSV genomic RNA (red) and nucleocapsid protein (green) in an epithelial cell. (a) XY, XZ, and YZ profiles at location designated by the yellow cross-hair are provided as evidence of colocalization. Strong yellow signal representing colocalization can be observed in both cross-sections.(b) From the 3D reconstruction of voxels, a scatter plot of voxel intensities was generated, and the Manders overlap coefficient calculated. In this case the Manders overlap coefficient was 0.65, demonstrating colocalization in three dimensions.

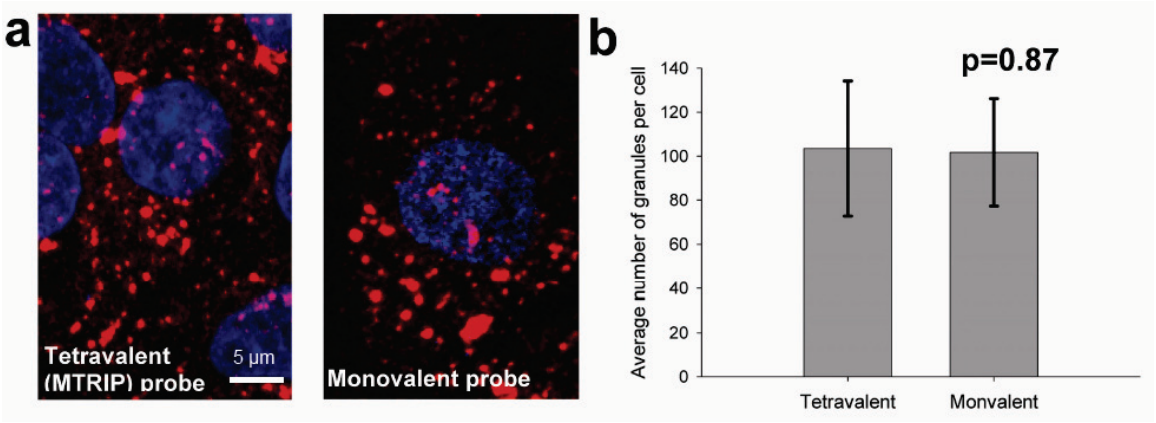

Figure 5.5: Comparison of tetravalent MTRIPs and monovalent probes (single multiply-labeled ligand) both targeted to hRSV genomic RNA (red). (a) Representative images from infections targeted by each probe type. Both sets of cells were plated simultaneously and infected from the same lot of virus. It should be noted that even though the number of granules detected is statistically similar, the photomultiplier voltage settings on the laser scanning confocal was approximately 4 times higher for the monovalent probe, which was expected. By combining 4 ligands, the resulting MTRIPs were 4 times brighter, a necessity for the live-cell imaging in Fig. 2 and 3. The nucleus (blue) was stained with DAPI. (b) RNA granules from over 30 cells for both the tetravalent and monovalent probes were counted via Volocity using the same conditions; statistical similarity of the distributions was determined with the Wilcoxon- Mann-Whitney test, resulting in a p value of 0.87, which strongly suggests that the samples originated from the same population. This provides strong evidence that MTRIPs do not significantly aggregate RNA; RNA aggregation would have resulted in the detection of different numbers of RNA granules.

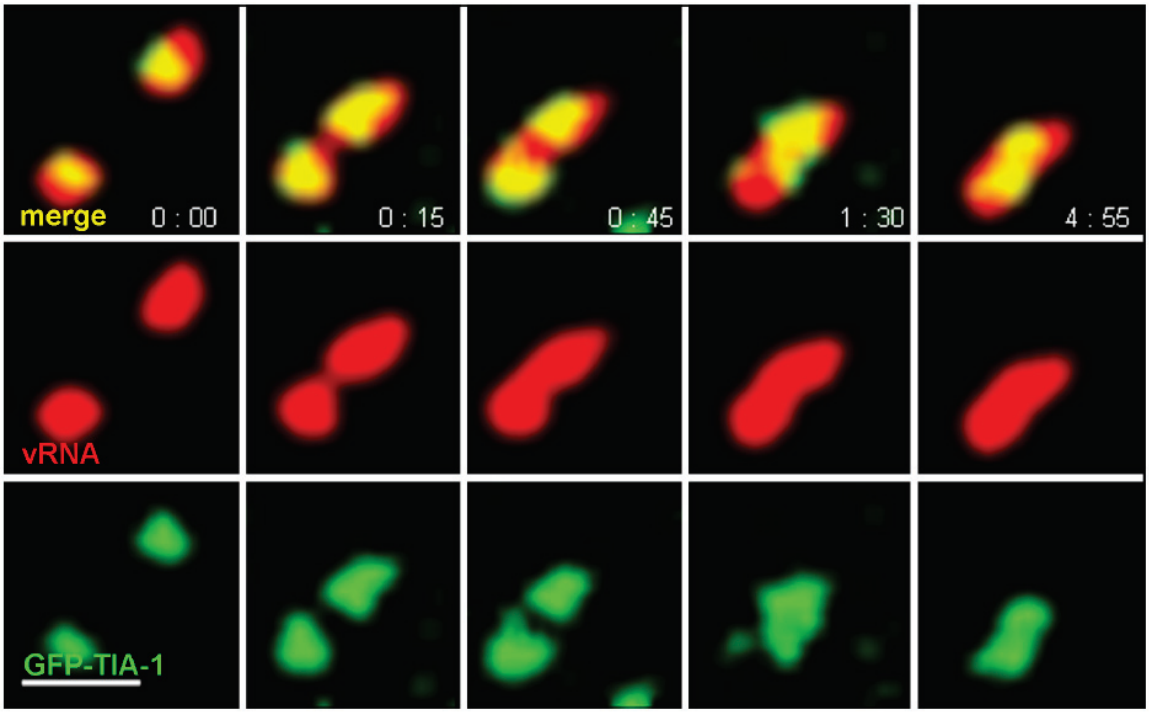

Figure 5.6: Time-lapse imaging of granule fusion. Time-lapse imaging reveals, over a 5 minute period, the fusion of a viral RNA granule that is well associated with GFP-TIA-1. Granule fusion takes approximately 30 seconds and they remain fused for over 4 minutes. The association shown here, between GFP-TIA-1 and the viral RNA, is not as transient as shown earlier in Fig. 3, given that the green signal follows the fusion process. These images suggest that there are multiple types of interactions, including an association of RNA binding protein with the RNA granules. Scale bar, 1 μm

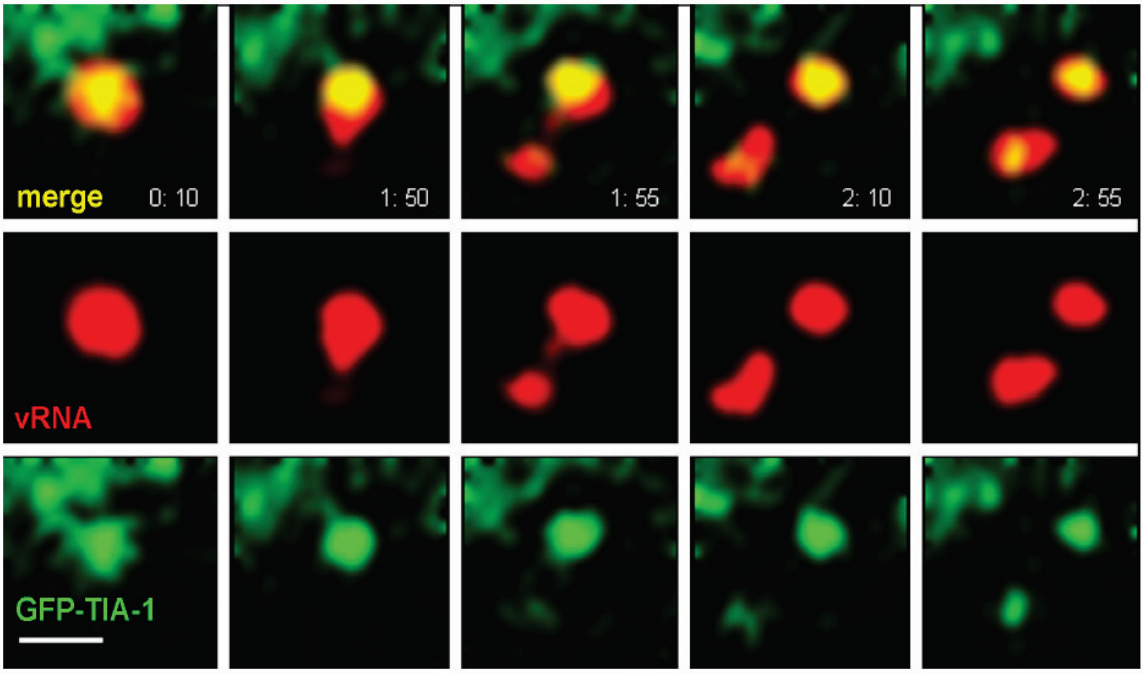

Figure 5.7: Time-lapse imaging of granule splitting. Time-lapse imaging reveals, over a 3 minute period, the splitting of a viral RNA granule that is well associated with GFP-TIA-1. Over the 3 minute period, the splitting occurs rapidly, under 15 seconds; once split, the granules remained separated during our imaging period. Again, the association shown here, between GFP-TIA-1 and the viral RNA, is not as transient as shown earlier in Fig. 3, given that the green signal follows the splitting process. Scale bar, 1 μm.

In addition to the transient behavior shown in **Figure 5.3**, we also noted that GFP-TIA-1 was visible on some of the viral RNA granules approximately 20 to 30 minutes after sodium arsenite treatment. Their association was confirmed by capturing video images of RNA granules during both a fusion (**Figure 5.6** and **Video 7**) and splitting event (**Figure 5.7** and **Video 8**), and observing the protein follow the same dynamic course as the RNA. The overlap is not perfect, suggesting that only some of the RNA in the granule may be in contact with GFP-TIA-1, but the association is quite obvious. This finding suggests that there may be multiple mechanisms by which TIA-1 interacts with RNA, in a transient, granule-granule manner (**Figure 5.3**), which may depend on granule size, and also through a more stable event, driven by RNA-protein binding.

Comparison of tetravalent MTRIPs with monovalent ligands

Tetravalent MTRIPs and monovalent probes (single multiply-labeled ligand) both targeted to hRSV genomic RNA were delivered via SLO, each at 30 nM, into separate wells of A549 cells, each infected from the exact same vial of virus, 24 hrs post-infection. The cells were then fixed in 4% paraformaldehyde and imaged via laser scanning confocal. From the reconstructed 3D images of the cells (see extended view images of the cells in **Figure 5.5a**), the number of viral RNA granules could be counted for each probe type. It should be noted that even though the number of granules detected is statistically similar via the Wilcoxon-Mann-Whitney test, the photomultiplier voltage on the laser scanning confocal microscope was approximately 4 times higher for the monovalent probe, which was expected. By combining 4 ligands, the resulting MTRIPs were 4 times brighter, a necessity for the live-cell imaging in **Figure 5.3**. From the results of counting RNA granules from over 30 cells (**Figure 5.5**) for both the tetravalent and monovalent

probes, the statistical similarity of the two populations could be estimated using the Wilcoxon-Mann-Whitney test. From this test, the resulting p value of 0.87 was determined, which conclusively demonstrates that the samples originated from the same population. This conclusively shows that MTRIPs do not significantly aggregate RNA; RNA aggregation would have resulted in the detection of different numbers of RNA granules.

Materials and Methods

MTRIPs.

The 2′ *O*-methyl RNA-DNA chimera nucleic acid ligands were synthesized by Biosearch Technologies, Inc. Each contains a 5′biotin modification and multiple dT-C6-NH_2, modifications. The streptavidin used for the core was purchased from Pierce. Probes were assembled by first labeling the free amine groups on the ligands with either Cy3B–NHS ester (GE Healthcare) or Atto 647N–NHS ester (Atto-Tec GmbH) using manufacturers' protocols. Free dye was removed using both Nanosep spin columns (Pall Corp.) and illustra G-25 size-exclusion columns (GE Healthcare). The purified ligands were resuspended in 1× phosphate-buffered saline (PBS; pH 7.4) and mixed at a 10:1 molar ratio with streptavidin for 1 h at room temperature (18–22 °C). Free ligands were removed using 30 kDa Nanosep spin columns, and stored at 1 μM final concentration in 1× PBS at 4 °C. When multiple probes were used, each probe was completely assembled and filtered separately, and then mixed with equimolar concentrations in streptolysin O and medium just before delivery into cells We estimated the cost of MTRIPs, based on 30 nM delivery concentration, to be $0.15 per well, for a 24-well plate.

Cells and Virus:

A549 lung carcinoma cells (American Type Culture Collection CCL-185) were grown in DMEM (Sigma Aldrich) with 10% fetal bovine serum (FBS; Hyclone) with 100 U ml^{-1} of penicillin and 100 mg ml^{-1} of streptomycin. Virus used was the A2 strain of hRSV (American Type Culture Collection VR-1544) at a titer of 1×10^6 50% tissue culture infectious dose ($TCID_{50}$) ml^{-1}. The titer was evaluated by serial dilution and immunostaining, 4 d after infection. Infection data was at day 1 after infection and with a multiplicity of infection of 5. All cells were infected at greater than 80% confluence, by removing the media, washing with 1× PBS (without Ca^{2+} and Mg^{2+}) and then adding virus to the cells for 30 min at 37 °C. After the 30-min incubation, complete medium was added. For the motile epithelial cell experiments, A549 cells were seeded at 5% confluence such that there were a substantial number of cells without contacts with other cells. For the motile fibroblast experiments, primary chicken embryonic fibroblasts (Charles River Laboratories) were grown in CEF growth medium (Charles River Laboratories), containing 5% FBS and seeded at 5% confluence.

Plasmids and transfections: The pSRα-GFP-HA-TIA-1 plasmid (Kedersha, Cho et al. 2000) was used to image stress granules in living cells. A549 cells plated in penicillin- and streptomycin-free medium were transfected using Fugene HD (Roche) at a ratio of Fugene HD to DNA of 2.5 μl μg^{-1}.

Time-lapse fluorescence microscopy: Live-cell video microscopy was performed using cells grown in Bioptechs T4 plates with an objective heater. The cells were imaged in Leibovitz's L15 medium supplemented with 10% FBS. Images were taken with a Zeiss Axiovert 200M microscope, with an ×63, numerical aperture (NA) = 1.4 Plan-Apochromat objective and Hamamatsu ORCA-ER AG camera, using Chroma 49002 ET-

GFP and 49004 ET-Cy3 filter sets, controlled by Volocity software. For the stress granule-RNA experiments, images of GFP–TIA-1 and the Cy3B-labeled MTRIPS were taken at 0.2 Hz (every 5 s), with exposure times of 71 and 41 ms, respectively, for up to 8 min.

Stress granule-RNA time-lapse microscopy: A549 cells, transfected with the above plasmid for 24 h were then infected with hRSV as above. Twenty-four hours after infection, the MTRIPs were delivered at 25 nM final concentration, and the cells exposed to 1.0 mM sodium arsenite for 30 min(Kedersha, Cho et al. 2000). During the 30-min incubation, the cells were observed periodically using epifluorescence microscopy. After 15 min of exposure, stress granules (marked by GFP–TIA-1 aggregates) were observed; an imaging plane containing both RNA granules and stress granules was chosen and time-lapse microscopy was initiated. Out-of-focus light was removed using Volocity's 2D deconvolution algorithm.

Conclusion

Here we have shown that MTRIPs can be used to image and track the viral genomic RNA of hRSV in the cytoplasm of live and fixed cells. Targeting was demonstrated by a high signal to background ratio and by colocalization with the hRSV N protein, a known binding partner. MTRIPs were used to demonstrate the increase in abundance and changes in localization and morphology of genomic RNA structure in infected cells. When used in conjunction with fluorescent protein fusions, MTRIPs were able to follow genomic RNA granules as they docked with, entered and passed through stress granules. These data suggest that MTRIPs will be useful in studying how viral

RNAs interact with other host factors such as cytoplasmic RNA sensors such as TLR 3, TLR 7, TLR 8 and the RIG-I like family of receptors.

References

Brandenburg, B., L. Y. Lee, et al. (2007). "Imaging poliovirus entry in live cells." PLoS Biol **5**(7): e183.

Brandenburg, B. and X. Zhuang (2007). "Virus trafficking - learning from single-virus tracking." Nat Rev Microbiol **5**(3): 197-208.

Ghildyal, R., J. Mills, et al. (2002). "Respiratory syncytial virus matrix protein associates with nucleocapsids in infected cells." J Gen Virol **83**(Pt 4): 753-757.

Iseni, F., D. Garcin, et al. (2002). "Sendai virus trailer RNA binds TIAR, a cellular protein involved in virus-induced apoptosis." Embo J **21**(19): 5141-5150.

Kedersha, N., S. Chen, et al. (2002). "Evidence that ternary complex (eIF2-GTP-tRNA(i)(Met))-deficient preinitiation complexes are core constituents of mammalian stress granules." Mol Biol Cell **13**(1): 195-210.

Kedersha, N., M. R. Cho, et al. (2000). "Dynamic shuttling of TIA-1 accompanies the recruitment of mRNA to mammalian stress granules." J Cell Biol **151**(6): 1257-1268.

Kedersha, N., G. Stoecklin, et al. (2005). "Stress granules and processing bodies are dynamically linked sites of mRNP remodeling." J Cell Biol **169**(6): 871-884.

Mollet, S., N. Cougot, et al. (2008). "Translationally repressed mRNA transiently cycles through stress granules during stress." Mol Biol Cell **19**(10): 4469-4479.

Norrby, E., H. Marusyk, et al. (1970). "Morphogenesis of respiratory syncytial virus in a green monkey kidney cell line (Vero)." J Virol **6**(2): 237-242.

Pederson, T. (2001). "Fluorescent RNA cytochemistry: tracking gene transcripts in living cells." Nucleic Acids Res **29**(5): 1013-1016.

Santangelo, P. J. and G. Bao (2007). "Dynamics of filamentous viral RNPs prior to egress." Nucleic Acids Res **35**(11): 3602-3611.

Tawar, R. G., S. Duquerroy, et al. (2009). "Crystal structure of a nucleocapsid-like nucleoprotein-RNA complex of respiratory syncytial virus." Science **326**(5957): 1279-1283.

Tilsner, J. and K. J. Oparka (2010). "Tracking the green invaders: advances in imaging virus infection in plants." Biochem J **430**(1): 21-37.

Zeitelhofer, M., D. Karra, et al. (2008). "Dynamic interaction between P-bodies and transport ribonucleoprotein particles in dendrites of mature hippocampal neurons." J Neurosci **28**(30): 7555-7562.

CHAPTER 6

HRSV AND RIG-I LIKE RECEPTORS

Background

Currently, the spatial biology of human respiratory syncytial virus (hRSV) is still under investigation, with many questions still unanswered about the ultrastructure of viral and host protein complexes in infected cells. To date, the function and complete composition of cytoplasmic inclusion bodies is still unknown, as well as details of the host cell interactions with these virus-specific structures. Host cell interactions are accomplished though varied means, but first line detectors of viral infections primarily involve two kinds of receptors: the cytoplasmic pattern recognition receptors, including the retinoic acid-inducible gene I (RIG-I) and melanoma differentiation-associated gene 5 (MDA5), both RNA helicases, and the pathogen-associated molecular pattern receptors, known as the Toll-like receptors (TLRs)(Mogensen 2009; Barbalat, Ewald et al. 2011). TLR3 and TLR7 sense double- and single-stranded RNA, respectively, and in most cell types reside within endosomes(Mogensen 2009). In contrast, TLR4, expressed on the cell surface, plays a role in sensing viral surface glycoproteins(Mogensen 2009). RIG-I and MDA5 reside within the cytosol, and there are reports of them responding to both single- and double-stranded RNA(Mogensen 2009). TLR signaling, mediated by MyD88, and RIG-I-like receptors, mediated by the mitochondrial antiviral signaling (MAVS) protein (also known as the interferon promoter-stimulating factor 1 [IPS-1] adaptor protein), results in the production of interferon(Mogensen 2009).

In response to hRSV, both TLRs and RIG-I-like receptors have been implicated in the general response to the infection. The hRSV fusion (F) protein has been shown to antagonize TLR4 in a mouse model (Kurt-Jones, Popova et al. 2000). In A549 and mouse embryonic fibroblast (MEF) cells, it has been shown that RIG-I was essential for promoting the innate immune response, with MDA5 playing an auxiliary role (Liu, Jamaluddin et al. 2007; Loo, Fornek et al. 2008; Yoboua, Martel et al. 2010). Even though there has been some confusion in the literature, recent results depicting the early events (0 to 6 hrs PI) of an hRSV infection have shown that both RIG-I and MDA5 play a significant role in both NF- κB and IRF3 signaling (Yoboua, Martel et al. 2010).

In addition, a number of viral proteins have been implicated in decreasing the innate response to hRSV. The highly glycosylated attachment (G) protein has been shown to inhibit TLR3/4 signaling in dendritic cells. Non-structural protein 1 (NS1) expression has been correlated with a decrease in TRAF3 levels, and non-structural protein 2 (NS2) has been shown to interact with RIG-I and its expression to correlate with decreases in TRAF3 and STAT2 levels (Bitko, Shulyayeva et al. 2007; Swedan, Andrews et al. 2011).

One drawback of many investigations of hRSV induction of the innate immune response to date has been the lack of spatio-temporal information at the level of the single cell. Previous work in this area has provided considerable insight primarily through biochemical assays, but these investigations often have neglected to study the events of interest within the context of the cell, retaining the spatial organization of hRSV proteins and RNAs. Many representations of the signaling events during hRSV infections depict hRSV genomic viral RNA as randomly distributed throughout the cytoplasm even though

this pattern has never been shown via microscopic investigation. Recent time-course imaging of hRSV genomic RNA using single-molecule sensitive hybridization probes clearly showed the RNA and the N protein localized near the plasma membrane in granules of varying size during the first 6 hours of infection in HEp-2 cells. The pattern progressed to a mixture of smaller granules near the cell membrane and moderate to large inclusion bodies, both at the cell membrane and deeper within the cells, at 12 hours post-inoculation (Lindquist, Lifland et al. 2010). By 24 hours PI, the plasma membrane contained many small granules, filaments and inclusion bodies, as well as inclusions deeper within the cell. It was observed via subsequent immunofluorescence staining that the N protein colocalized frequently (Manders overlap coefficient > 60%) with the genomic RNA in smaller granules (on the order of the point spread function, ~250 nm) but less frequently in moderate to large inclusion bodies, which often stained around their exterior with anti-N antibodies.

Currently the function of inclusion bodies in hRSV-infected cells is unknown. It has been speculated that they are sites of replication or transcription, morphogenic intermediates, or sites for the accumulation of dead-end products. Since their earliest mention in the literature, cytoplasmic inclusion bodies have been observed late in hRSV infections using both light and electron microscopy, both in cells infected in culture and in cells from infected children or animals. Inclusions of varying size have been immunostained with antibodies to the N, P, M, M2-1, and L proteins, but not for the F or G proteins (Garcia, Garcia-Barreno et al. 1993; Garcia-Barreno, Delgado et al. 1996; Ghildyal, Mills et al. 2002; Ghildyal, Li et al. 2005; Carromeu, Simabuco et al. 2007), and viral genomic RNA also has been detected either within them or around their

perimeter, depending on their size (Santangelo and Bao 2007; Lindquist, Lifland et al. 2010). Inclusion bodies have been shown to form spontaneously within cells in culture following the expression of both the N and P proteins, forming inclusions morphologically similar to those observed during viral infections (Garcia, Garcia-Barreno et al. 1993). When N or P was expressed separately, inclusions did not form; instead the proteins were distributed evenly throughout the cytoplasm.

Given our previous observations of hRSV organization, our initial goal in the current studies was to couple our previous localization results with additional information regarding the localization of components of the innate immune response such as RIG-I, MDA5, and MAVS, during an hRSV infection. The experiments yielded a number of interesting findings, including data showing that RIG-I and MDA5 colocalized with hRSV granules in the cytoplasm near the plasma membrane as soon as 6 hours PI, with MAVS remaining localized to mitochondria. By 12 hours PI, MAVS was still partially localized to the mitochondria, but also clearly localized within inclusion bodies, as was MDA5. By 24 hours PI, the detectable fraction of MAVS and MDA5 were contained within hRSV granules and inclusion bodies. Given that granules and inclusions can be formed from the co-expression of N and P, we investigated whether the changes in localization observed during the infection occurred with the expression of N and P in the absence of other viral components, and found that the changes in localization still occurred. Next, we postulated that N was interacting with MAVS and MDA5, so we developed a proximity ligation assay (PLA) to assess this interaction *in situ*. PLAs use oligonucleotide-linked antibodies, distance-dependent ligation of DNA to induce circularization, rolling circle amplification, and fluorescently-labeled DNA hybridization

to test if two proteins interact. The assays can exhibit single interaction sensitivity within a distance of 40 nm (Soderberg, Gullberg et al. 2006; Soderberg, Leuchowius et al. 2008). Employing such assays we confirmed that N, either expressed alone or simultaneously with the P protein, was in proximity to MAVS and MDA5 *in situ*. It was also found that hRSV N co-precipitated with MDA5 when overexpressed, indicating an interaction, direct or indirect, between the two proteins. Furthermore, in order to confirm the function of the sequestration of these proteins within inclusion bodies, N and P were co-expressed, and the cells subsequently infected with Newcastle Disease virus (LaSota strain). These experiments showed a significant decrease in interferon β mRNA production compared to that during the wild-type infection, giving credence to the function of inclusion bodies as inhibitors of the innate immune response.

Overall, through an examination of the spatio-temporal changes in the localization of proteins involved in the innate immune response, we identified for the first time that the hRSV N protein and subsequent inclusion body formation serve to antagonize the innate immune response likely by interacting with and localizing MDA5 and MAVS.

Methods and Materials

Multiply-labeled tetravalent imaging probes

MTRIPs were prepared as previously described (Santangelo, Lifland et al. 2009). Briefly, 2′-O-Methyl RNA/DNA chimeric oligonucleotides were synthesized by Biosearch Technologies, Inc. with the following sequence, 5′-biotin-**U**XTXTTX**AAAAAXGGGGCAAAXAA**-3′, where the boldface type is 2′-O-Methyl RNA, the X is a dT-C6-NH2, and all others are DNA. The binding region is underlined. MTRIPs were assembled by first conjugating Cy3B-NHS ester fluorophores (GE Healthcare) to the oligonucleotide amine groups using the manufacturer's protocol. Labeled oligonucleotides were then tetramerized by incubation with Neutravidin (Pierce).

Cell culture and viruses

A549 lung carcinoma cells (American Type Culture Collection [ATCC)]CCL-185), HEp-2 cells (ATCC CCL-23), Vero cells (ATCC CCL-81), and HeLa Cells (ATCC CCL-2) were maintained in High Glucose DMEM (Lonza) with 10% FBS (Hyclone), 100 U ml^{-1} penicillin, and 100 μg ml^{-1} streptomycin (Invitrogen). The hRSV used was the A2 strain (ATCC VR-1544) prepared in HEp-2 cells at a titer of 1×10^6 plaque forming units ml^{-1}. Virus at a multiplicity of infection (MOI) of 1 was adsorbed to the cells for 1 h at 37°C. Following adsorption, fresh medium was added to the inoculum and the cells were incubated for the indicated times. The Newcastle disease virus (NDV) used was the LaSota strain and was a gift of Claudio L. Afonso, USDA. NDV was adsorbed onto cells at an MOI of 5 for 1 h at 37°C. Following adsorption, fresh medium (DMEM with 5% allantoic fluid) was added to the inoculum and the cells were incubated for the indicated times.

RNA probe delivery

For RNA probe delivery, cells were washed in Dulbecco's Phosphate Buffered Saline (DPBS) without Ca^{2+} and without Mg^{2+} (Lonza), and then incubated with 0.2 U ml^{-1} activated streptolysin O (Sigma) in OptiMEM I medium (Invitrogen) containing 30 nM MTRIP for 10 min at 37°C. Delivery medium was replaced with growth medium for 15 min to restore membrane integrity before fixation. In these experiments HEp-2 cells were used for expedience in comparison to previous studies of hRSV RNA and protein localization.

Immunostaining

Cells were fixed with 4% paraformaldehyde (Electron Microscopy Science) in PBS, permeabilized using 0.2% Triton X-100 (Sigma), and blocked with 5% bovine serum albumin (EMD). Cells then were incubated with primary antibody for 30 min at 37 °C, washed three times in PBS and subsequently incubated with the secondary antibody for 30 min at 37 °C. Multiple labeling was done sequentially. Cells then were washed three times in PBS and nuclei were stained using DAPI (Invitrogen). Cells were mounted on slides using Prolong Gold (Invitrogen).

Antibodies

Primary antibodies used were: goat anti-RIG-I (Santa Cruz), rabbit anti-MDA5 (ProSci inc.), rabbit anti-MAVS (Abcam), mouse anti-hRSV N (Abcam), and mouse anti-hRSV P (Clone 3_5). Secondary antibodies used were: donkey anti-mouse Alexa Fluor 488 (Invitrogen), donkey anti-rabbit Cy3 (Jackson ImmunoResearch), and donkey anti-goat Cy5 (Jackson ImmunoResearch).

Transfection and mitochondria staining

Vero and HeLa cells were cultured on glass coverslips in 24 well tissue culture plates for imaging experiments or directly in 6 well tissue culture plates for RT-PCR. Vero cells were utilized as they are a common model system for RSV infection, and HeLa cells were used where the interferon response was measured. Both of these cell lines were used in place of HEp-2 and A549 as the later are less efficiently transfected. Cells were transfected using Lipofectamine 2000 (Invitrogen) by the manufacturer's protocol. For each well in the 6 well plates, 8 µl of Lipofectamine 2000 and 4 µg of DNA was used. For each well in the 24 well plates, 2 µl of Lipofectamine 2000 and 1 µg of DNA was used. For IB and mitochondria colocalization experiments, Vero cells were grown in glass bottom petri dishes (In Vitro Sci) and transfected as above using 2 µl of Lipofectamine 2000 and 1 µg of DNA. Mitotracker 633 was used per the manufacturer's protocols at a dilution of 1:500. Plasmids used were pcDNA3.1, containing optimized cDNAs encoding the RSV A2 strain nucleoprotein (N) and phosphoprotein (P) genes (synthesized by GeneArt, Regensburg, Germany), GFP-MDA5 in a pEGFP-C2 vector (a gift of Dong-chul Kang), and a GFP-MAVS in a pEGFP vector (a gift of Stanley M. Lemon).

Imaging and processing

Cells were grown on No. 1.5 coverslips and fixed and immunostained. For hRSV N and vRNA colocalization studies an LSM 510 confocal microscope (Zeiss) using a 63×, NA = 1.4, Plan-Apochromat primary objective was used. All images were taken using multi-track scanning for each fluorophore to prevent bleed-through. Z-dimension stacks were taken in 0.5-µm increments; the 543 nm laser was used for the Cy3B, the 488 nm laser

for N protein immunostaining, and the pinholes were set to an airy unit of 1 (equal to airy disk). For all other experiments, images were taken on an Axiovert 200M microscope (Zeiss) with a 63×, NA= 1.4 Plan-Apochromat primary objective and an ORCA-ER AG camera (Hamamatsu). Fluorescent filter sets used were 89000 Sedat Quad - ET for multiple wavelength imaging (Chroma). All imaging experiments were performed using the Volocity acquisition software (PerkinElmer). Image stacks were recorded at 200-nm intervals for fixed cell samples to adequately sample volumes for iterative deconvolution. Images presented are deconvolved from the widefield data and linearly contrast enhanced unless otherwise noted. Granule counting and object identification were performed in Volocity. Objects were identified by the standard deviation of intensity and filtered to remove objects less than one point spread function in volume.

RT-PCR

HeLa cells were grown on 6-well plates and transfected as described and inoculated with NDV LaSota strain 24 h post-transfection. Total RNA was extracted at the indicated time points using the RNeasy Mini kit (Qiagen). Total RNA was checked subsequently for integrity via agarose gel electrophoresis and quantified via UV-VIS spectroscopy. 1 µg total RNA was used for cDNA synthesis using the RT^2 first strand kit (SA biosciences) according to the manufacturer's instructions. 1 µl of the product then was used for qRT-PCR using the Real-time RT^2 qPCR primer assay (SYBR green) in the presence of gene-specific primers for ACTB and IFNB1 (SA Biosciences). qRT-PCR was performed using ABI StepOnePlus real-time PCR system (Applied Biosciences).

Proximity ligation assays

PLA detection between hRSV N or hRSV P protein and MAVS, RIG-I or MDA5 was performed using the Duolink II kit (Olink Bioscience) with anti-rabbit or anti-goat plus and anti-mouse minus probes according to the manufacturer's protocol. Cells were fixed with 4% paraformaldehyde, permeabilized and blocked using 0.5% Tween 20 (CalBioChem), 0.1% Triton-X 100, 0.1% gelatin (Aurion), 2% donkey serum (VWR), 1% bovine serum albumin in nuclease-free phosphate buffered saline (PBS). Cells then were incubated with primary mouse anti-hRSV N or Mouse anti-hRSV P antibody (1:500) followed by either rabbit anti-MAVS rabbit anti-MDA5 antibody, or goat anti-RIG-I (1:250). Subsequently, cells were incubated with the oligonucleotide-labeled secondary antibodies diluted in 0.05% Tween-20 in nuclease-free PBS.

Spin Capture of RSV filaments on glass

In order capture single hRSV filamentous virions on glass, hRSV A2 was propagated in HEp-2 cells at an MOI of 0.1. At four days PI, the cell-associated and supernatant fractions were scraped, freeze-thawed, and spun through 5µm and 0.45µm centrifugal filters (Millipore) at 5,000 x g and 4°C for 4 minutes and 1 minute, respectively. The fraction between 0.45µm and 5µm was collected and spun down onto poly-L lysine (Sigma) coated coverglass for at 3007 x g and 4°C for 30 minutes. The immobilized virions were fixed using 4% paraformaldehyde and immunostained according to the aforementioned protocol. In addition to the host protein and viral antibodies previously mentioned, virions were also stained with palivizumab, which binds to the hRSV F protein (MedImmune).

Immunoprecipitation and Western Blotting

HeLa cell were transfected with GFP-MAVS and RSV N or GFP-MDA5 and RSV N using lipofectamine 2000 as above. Cells were lysed in RIPA buffer (Thermo) supplemented with complete protease inhibitor (Roche). Lysates were stored at -80ºC until use. For immunoprecipitation, Dynalbeads coated with Sheep anti-Rabbit antibodies (Invitrogen) were incubated overnight at 4ºC with Rabbit anti-GFP antisera (Thermo). The beads were washed and lysates were added to the beads. Lysates were tumbled overnight at 4ºC. The beads were washed to remove unbound proteins. To release the precipitate, SDS buffer (LI-COR Biosciences) was added to the beads and the solution was incubated at 70ºC for 10 min. The eluted proteins were loaded into 10% Bis-Tris gels (Invitrogen) and run using MOPS buffer (Invitrogen). Western transfer was performed in a XCell II blot Module (Invitrogen) onto nitrocellulose paper (Invitrogen) according to the manufacturer's protocol. Blotting was performed using a Snap i.d. (Millipore). Blots were blocked using Odyssey blocking buffer (LI-COR Biosciences), primary antibodies, mouse anti-GFP and mouse anti-RSV N, were diluted in Odyssey blocking buffer with 0.1% Tween-20 (CalBioChem) and incubated on the blots for 10 min. Blots were washed in PBS with 0.1% Tween-20. Secondary goat anti-mouse antibody labeled with DyLight 680B (Thermo) diluted as above, was incubated for 10 min. Blots were washed as above. Blots were imaged on an Odyssey (LI-COR Biosciences) at 42 μm $pixel^{-1}$ using the "high" quality setting. Blots were linearly contrast enhanced in ImageJ for clarity. Bands corresponding to RSV N and the GFP-MAVS and GFP-MDA5 were differentially enhanced due to the sensitivity differences of the primary antibodies against the respective proteins.

Localization and structure of granules associated with hRSV N protein and vRNA during infection

We first analyzed the structures and distribution of viral proteins and genomic RNA at 6, 12, or 24 hours post-infection (hpi). HEp-2 cell monolayers were inoculated with hRSV strain A2 at an MOI of 1 and incubated in growth medium for the indicated times. Multiply-labeled tetravalent imaging probes (MTRIPs) were delivered into the live cells as described and they were subsequently fixed and immunostained for hRSV N **(Figure 6.1**). At 6 hpi, both the viral genomic RNA and inclusion bodies (IBs) positive for hRSV N protein were punctate and colocalized (**Figure 6.1**, Row 1). Morphologically the IBs were round, and no filaments were present. The average volume of the IBs at this time point was 0.9 μm^3. At 12 hpi, hRSV N staining was seen as both a diffuse population that filled the cytoplasm and as inclusion bodies, which were larger than those detected at 6 hpi (**Figure 6.1**, Row 2). These larger inclusion bodies (>8 μm^3 with an average of 37 μm^3) did not contain genomic RNA detectable with probes, unlike those at 6 hpi. The genomic RNA was located predominantly at the plasma membrane and in smaller granules within the cytoplasm. At 24 hpi, N protein could also be detected in viral filaments on the plasma membrane of the cells in addition to the diffuse hRSV N staining and the staining of IBs (**Figure 6.1**, Rows 3-5). These filaments contained viral genomic RNA, as previously described (Santangelo and Bao 2007; Utley, Ducharme et al. 2008; Lindquist, Lifland et al. 2010). Notably the larger IBs contained little to no genomic RNA despite containing high levels of the N protein, which binds to the genomic RNA in the virion.

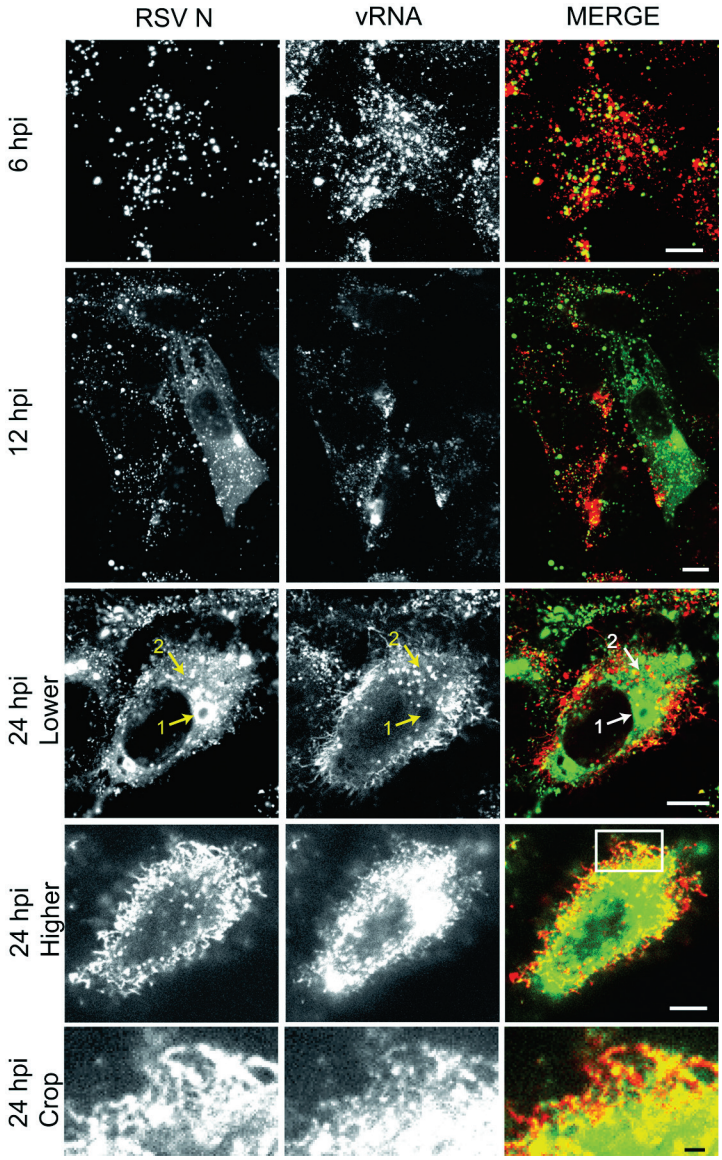

Figure 6.1: hRSV genomic RNA colocalized with small but not large inclusion bodies (IBs). HEp-2 cells we infected with hRSV strain A2 at an MOI=1.0 for 6, 12 or 24 hours, and subsequently hRSV N was detected using immunostaining and genomic RNA detected with a live cell hybridization probe. Column 1 shows hRSV N localization. Column 2 shows the localization of viral genomic RNA. Column 3 shows the merge of the first two columns with hRSV N staining in green and genomic RNA in red. Arrow 1 shows a large IB containing hRSV N but not genomic RNA. Arrow 2 shows a region containing small IBs, hRSV N colocalized with genomic RNA. A higher and lower optical plane of the cell at the 24 hpi time point is shown. A crop of the higher plane is shown to emphasize detail of the viral filaments. Scale bars are 10 µm in the top 4 rows. Scale bar is 5 µm in row 5.

Viral inclusion bodies colocalize with proteins of the innate immune response

To test whether the hRSV IBs contained proteins of the RLR antiviral response pathway, we infected A549 cells and fixed them at 6, 12 or 24 hpi, or fixed prior to infection (mock), and stained for hRSV N, MAVS, and RIG-I. In the mock-infected cells no RSV N or RIG-I staining was present and MAVS staining appeared to be mitochondrial (**Figure 6.2**, Row 1). At 6 hpi, hRSV N was in a punctate pattern and MAVS staining continued to appear filamentous throughout the cytoplasm, indicative of mitochondria, as would be expected (**Figure 6.2**, Row 2)(Seth, Sun et al. 2005). RIG-I staining was similar to hRSV N and was punctate. All three proteins were present inside of the hRSV N IBs, with a strong correlation between the hRSV N staining and the RIG-I staining. At 12 hpi, hRSV N was again in larger IBs that appeared to be hollow (**Figure 6.2**, Row 3). MAVS staining at 12 hpi was altered dramatically with some of the protein localizing to large IBs that were not observed at earlier time points and appeared to be surrounded by a "ring" of hRSV N staining. Cytoplasmic MAVS staining was still present, however, this staining was no longer filamentous and did not resemble mitochondria. RIG-I staining also was increased inside the larger IBs as well as throughout the cytoplasm. At 24 hpi, both MAVS and RIG-I were localized to large IBs and to viral filaments at the plasma membrane (**Figure 6.2**, Row 4,5).

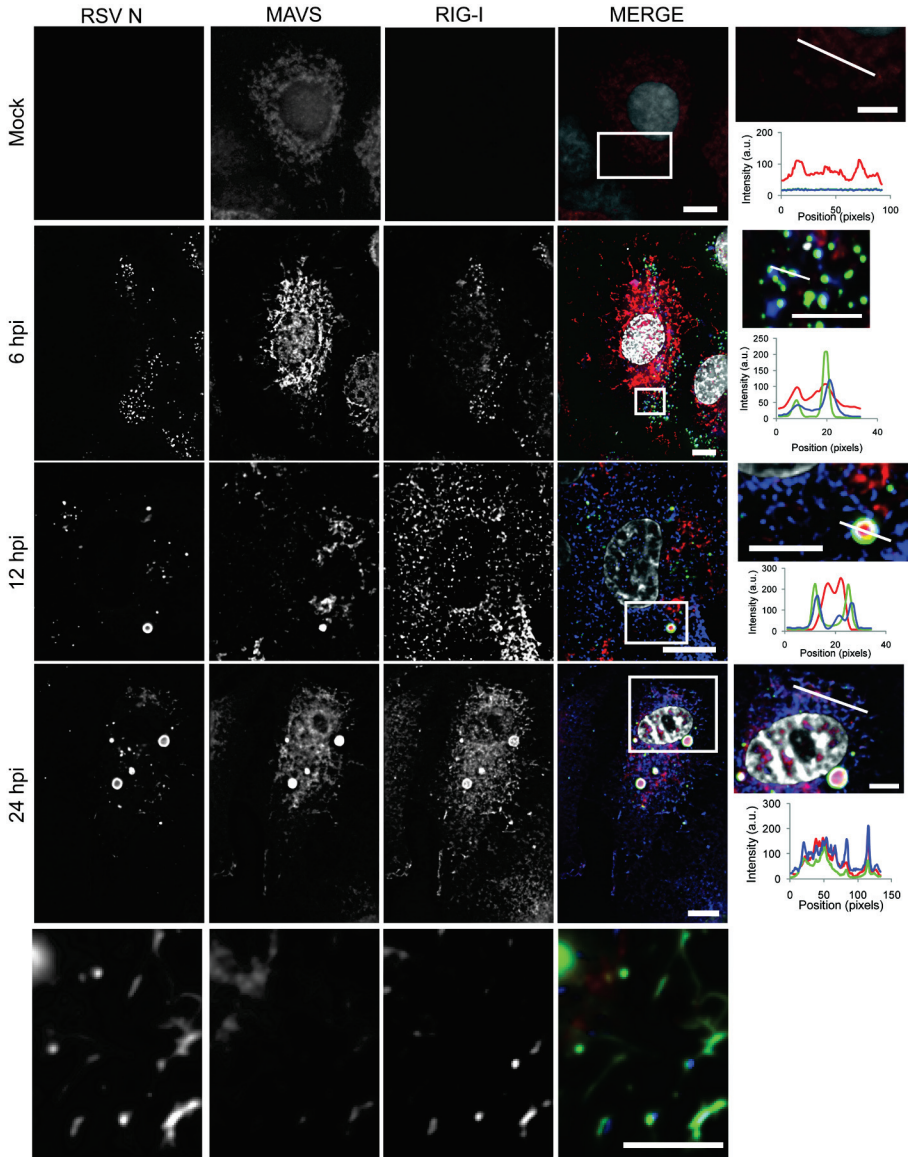

Figure 6.2: hRSV IBs colocalize with MAVS and RIG-I. A549 cells were infected with RSV strain A2 at an MOI=1.0 and incubated for 6, 12, or 24 hours, or mock infected**.** hRSV N, MAVS and RIG-I were detected by immunofluorescence. Column 1 shows RSV N staining, column 2 shows MAVS staining, and column 3 shows RIG-I staining. Column 4 is a merge with hRSV N colored green, MAVS colored red and RIG-I colored blue. The nucleus, stained by DAPI is colored white. Column 5 is an increased magnification view of the boxes in the merged images. Below each panel is an intensity line graph showing the intensity of each channel along the line in the cropped image. Detail filaments in a higher optical plane of the cell in the 24 hpi time point is shown in row 5. Scale bars in column 4, rows 1-4, are 10 µm and in column 5 and row 5 they are 5 µm. Images for the mock infections are widefield only due to computational artifact of deconvolving background without positive signal.

In order to see if this change in protein localization was specific to RIG-I/MAVS, or was a more general phenomena of the RLR pathway, we next co-stained for hRSV N, RIG-I and MDA-5. In the mock-infected cells no RSV N, MDA5 or RIG-I staining was present (**Figure 6.3**, Row 1). At 6 hpi, MDA5 was predominately coincident with IBs containing hRSV N, with little cytoplasmic staining apparent outside of these regions (**Figure 6.3**, Row 2). At 12 hpi, MDA5 colocalized with IBs of all sizes, and there was little to no staining detected outside of these regions (**Figure 6.3**, Row 3). At 24 hpi, MDA5, like RIG-I, was present at viral filaments at the plasma membrane (**Figure 6.3**, Rows 4,5).

Owing to the dense nature of viral and host proteins near the plasma membrane, it was difficult to separate bright signal from IBs from the lighter signal inside filaments. To circumvent this problem, viral filaments were isolated from infected cells, deposited and fixed on glass coverslips, and immunostained for hRSV F, hRSV N and RIG-I, MDA5 or MAVS (**Figure 6.4**). While MDA5 stained strongly in the isolated filaments, neither RIG-I nor MAVS were observed to colocalize with them.

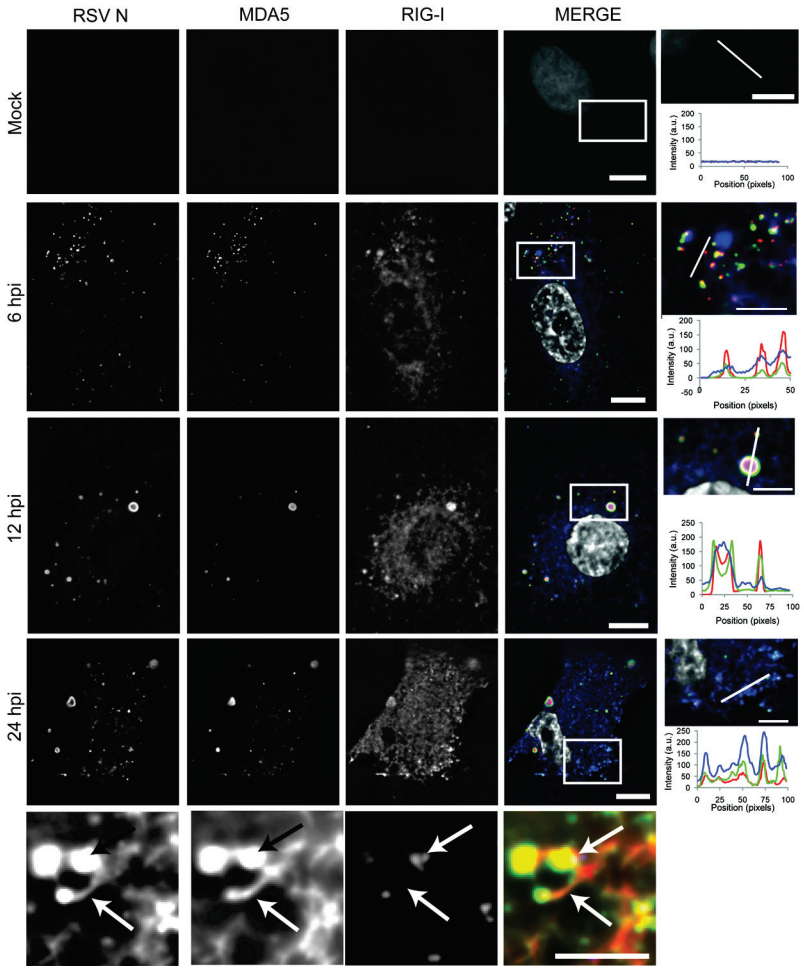

Figure 6.3: hRSV IBs colocalize with MDA5 and RIG-I. A549 cells were infected with hRSV strain A2 at an MOI=1.0 and incubated for 6, 12, or 24 hours, or mock infected. hRSV N, MDA5 and RIG-I were detected by immunofluorescence. Column 1 shows hRSV staining, column 2 shows MDA5 staining and column 3 shows RIG-I staining. Column 4 is a merge with hRSV N colored green, MDA5 colored red and RIG-I colored blue. The nucleus, stained by DAPI is colored white. Column 5 is an increased magnification view of the boxes in the merge image. Below each panel is an intensity line graph showing the intensity of each channel along the line in the cropped image. Detail filaments in a higher optical plane of the cell in the 24 hpi time point is shown in row 5. The arrows in row 5 point to an inclusion body (upper) and a viral filament (lower). Scale bars in column 4, rows 1-4, are 10 µm and in column 5 and row 5 they are 5 µm. Images for the mock infections are widefield only due to computational artifact of deconvolving background without positive signal.

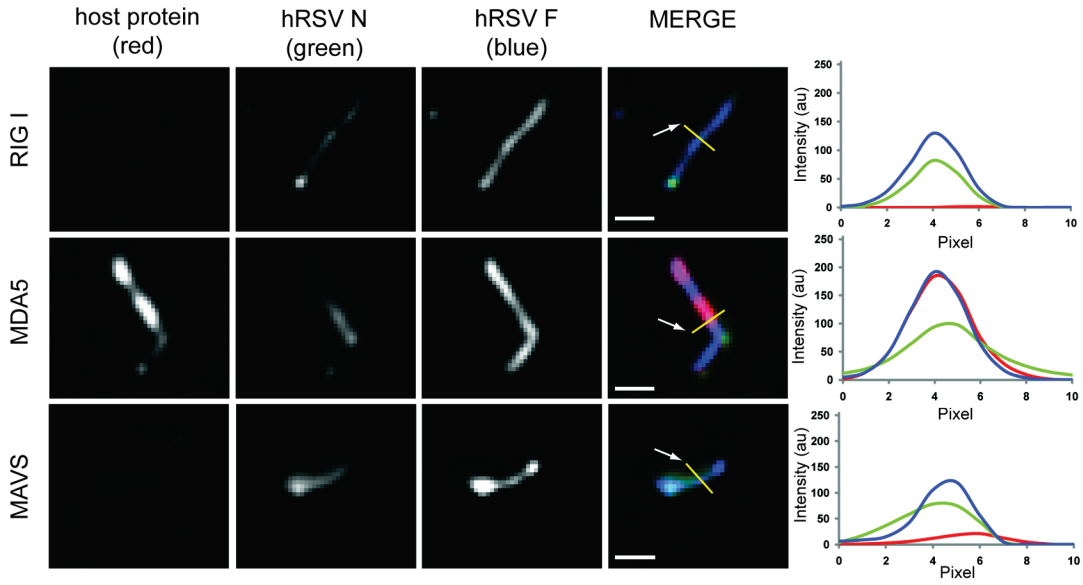

Figure 6.4: MDA5 colocalized with isolated viral filaments. HEp-2 cells we infected with hRSV strain A2 at an MOI=0.1 and viral filaments were isolated 4 dpi. Viral filaments were isolated by filtration and adsorbed onto coverglass for immunostaining. Column 1 shows the host protein RIG-I, MDA5, or MAVS, red in the merge. Column 2 shows hRSV N staining, green in the merge. Column 3 shows hRSV F staining, blue in the merge. Column 4 shows the merge. Column 5 shows an intensity profile through the lines in the merged images, arrow denotes pixel number 1. Scale bar is 1 µm.

Expression of hRSV N and P proteins was sufficient to localize proteins of the innate immune response.

In order to test whether the presence of IBs alone was sufficient to localize RIG-I, MDA5, and MAVS, hRSV N and P were expressed in Vero cells that subsequently were fixed and immunostained. As seen in the left column of **Figure 6.5**, the expression of hRSV N and P resulted in the formation of both small and large IB-like structures similar to those seen in the infection model. In these cells, RIG-I staining was increased in and around the IBs, however, RIG-I was not localized exclusively to the IBs. In contrast, both MDA5 and MAVS were localized almost exclusively to the IBs, and little staining was detected outside of these regions. In order to quantify these results, colocalization data was obtained from over 100 cells from five fields, and summarized in the graph in **Figure 6.5**. A colocalization analysis between N and RIG-I yielded a Pearson's coefficient of 0.5, and a Manders overlap of 0.4, suggesting the colocalization was strong but not complete. When the Manders overlap was broken into its constitutive parts, Mx and My, it was seen that three quarters of the N staining colocalized with RIG-I (My~0.75), while RIG-I staining colocalized with N approximately 25 percent of the time (Mx~0.25). In contrast, the Person's coefficient and Manders overlap for N with MDA5 or MAVS were both >0.75, and the Mx and My colocalization coefficients in these two cases were both >0.5, indicating near complete colocalization between the expressed inclusion bodies and MDA5 and MAVS.

To verify that neither the antibodies were cross-reacting, nor the fluorophores bleeding through to adjacent channels, cells infected with RSV for 24 hr were stained with a single primary antibody and all three secondary antibodies, anti-mouse Alexafluor

488, donkey anti-rabbit Cy3, and donkey anti-goat Cy5 (**Figure 6.6**). Signal was only present in the correct channel for the primary-secondary antibody combination indicating that bleed through of signal from particularly intense staining, such as RSV N, was not occurring at the exposure times used, nor was the cross-reaction of the secondary antibodies leading to detectable signal. There was more background in the Cy5 channel, however, the background was not due to bleed through, nor cross-reaction, as both of those would lead to the appearance of IBs in the Cy5 channel coincident with those in the Cy3 or 488 channels, which was not observed.

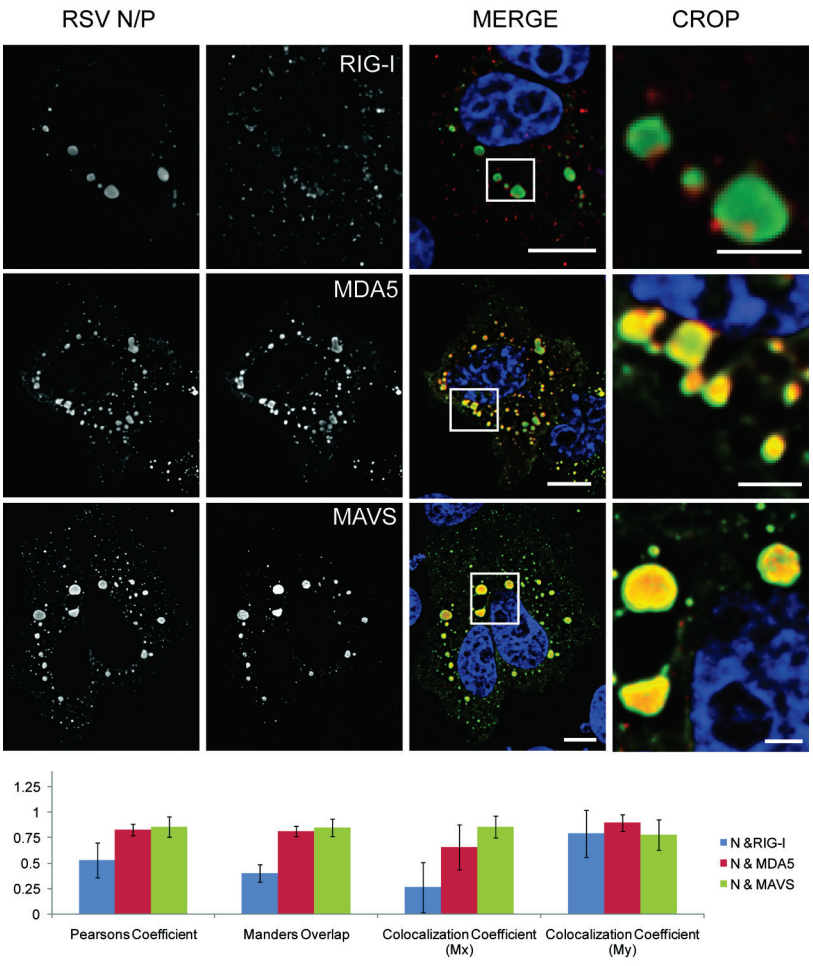

Figure 6.5: IBs formed by cDNA-based expression of hRSV N and P proteins colocalize with RIG-I, MDA5 and MAVS. Vero cells were transfected with plasmids encoding hRSV N-GFP fusion and hRSV P proteins. Cells were immunostained for N and either RIG-I, MDA5 or MAVS. Column 1 shows IBs marked by hRSV N-GFP and immunostaining against the N protein. Column 2 shows immunostaining against RIG-I (row 1), MDA5 (row 2), or MAVS (row 3). Column 3 shows the merge of column 1 (green) with column 2 (red). Nuclei are stained with DAPI and colored blue. Column 4 shows a higher magnification view of the boxed region of the panels in column 3. The bar graphs show Pearson's Coefficient, Manders overlap and individual components of Manders overlap (Mx and My). Data are from 5 independent fields. Error bars show standard deviation. Scale bars in column 3 are 10 µm and in column 4 are 2.5 µm.

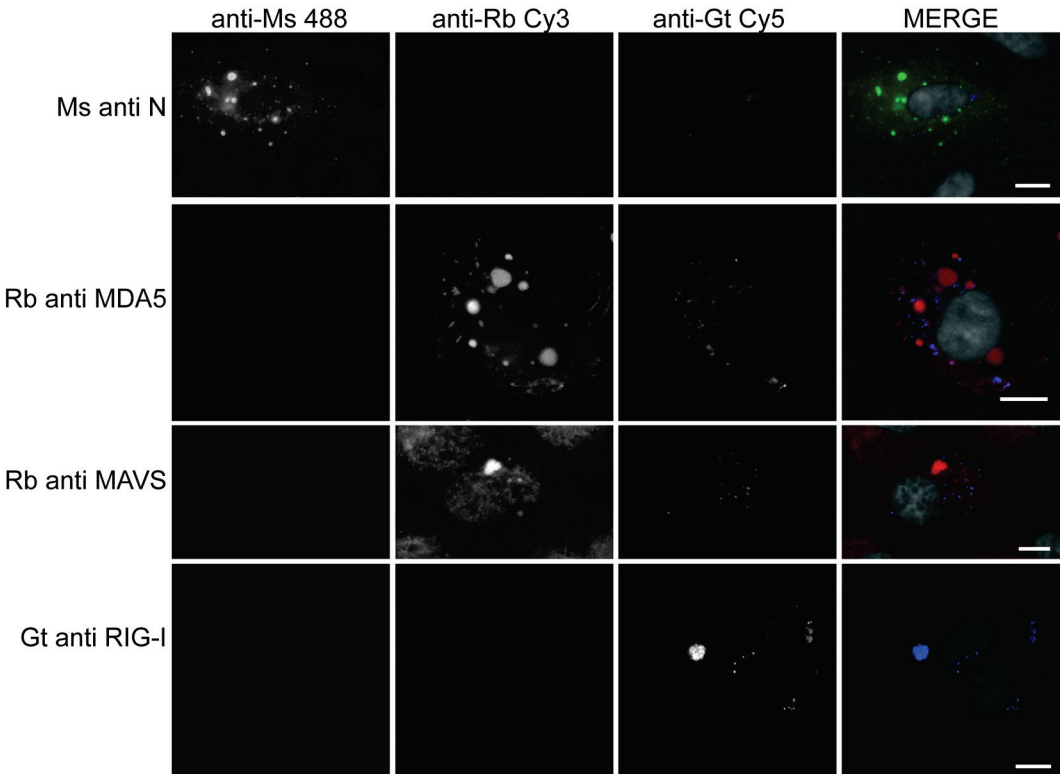

Figure 6.6: Secondary antibodies do not cross react with the primary antibodies, nor do the fluorophors bleed through to adjacent fluorescent channels. A549 cells we infected with hRSV strain A2 at an MOI=1.0 for 24 hours, and subject to immunostaining using a single primary antibody against hRSV N, MDA5, MAVS, or RIG-I. All three secondary antibodies against mouse (Ms), Rabbit (Rb), and goat (Gt) were applied. The columns show the individual channels correspinding to the 488, Cy3 and Cy5 labeled antibodies and the merge. Scale bars are 10 μm.

hRSV N is in close proximity to MDA5 and MAVS *in situ*.

The colocalization analysis discussed above suggested an interaction between the proteins of the innate immune response and the viral inclusion bodies. However, owing to the limited spatial resolution of the light microscope (~250nm), a separate assay was needed to demonstrate that the proteins were in close proximity (<30nm) and likely interacting in the cell. Immunoprecipitation is commonly used to demonstrate that two or more proteins interact, however, it is fundamentally an *in vitro* assay. The localization of interactions *in situ* is lost and rearrangements of proteins post-lysis may interfere with the interpretation of the results. In order to avoid these complications, we employed a proximity ligation assay (PLA) to demonstrate the close proximity of N with MAVS and MDA5 *in situ* during viral infection. **Figure 6.7** shows Vero cells stained for hRSV P (to identify hRSV IBs), and PLA between N and MAVS or MDA5 at 6 and 24 hpi. PLA control experiments can be seen in **Figure 6.8**. At 6 hpi, hRSV P staining resembled the IB granules marked by hRSV N, and the PLA signal between N and MDA5 had a nearly one-to-one correspondence with the signal from the hRSV P. At 24 hpi, hRSV P staining showed both IB and filamentous structures. The PLA signal between hRSV N and MDA5 at this time point was significantly stronger and, while it is much more heterogeneous than at 6 hpi, there was still a strong correlation between the IBs and filaments with the PLA signal. When PLA was performed between hRSV N and MAVS, there were fewer PLA granules observed. At 24 hpi, this increased; however, it never reached the levels of that of hRSV N/MDA5, and the colocalization between the PLA and hRSV P staining was lower.

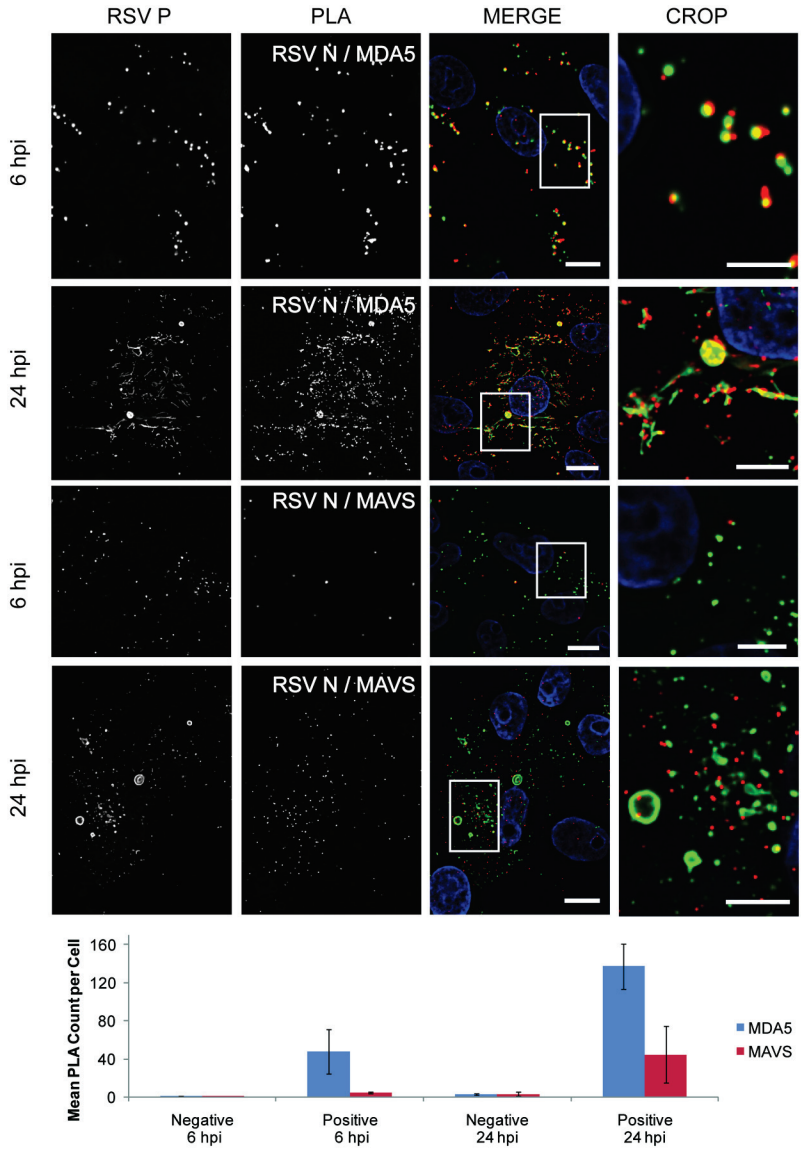

Figure 6.7: hRSV N interacts with MDA5 and MAVS. Vero cells were infected with hRSV strain A2 at an MOI=1.0 and incubated for 6 or 24 hours. Cells were stained for hRSV P and were assayed for the interaction between hRSV N and either MDA5 or MAVS by PLA. Column 1 shows the immunostaining for hRSV P. Column 2 shows the PLA signal from either hRSV N - MDA5 assays (rows 1 and 2) or hRSV N MAVS assays (rows 3 and 4). Column 3 shows the merge of column 1 (green) and column 2 (red) with the nucleus stained with DAPI in blue. Column 4 is a magnification of the boxed region in the panels in column 3. The bar graph shows the mean number of PLA spots per cell detected for each experimental condition along with those for the negative controls (see Figure 8). Error bars are standard deviation. Scale bars in column 3 are 10 µm and in column 4 are 5 µm.

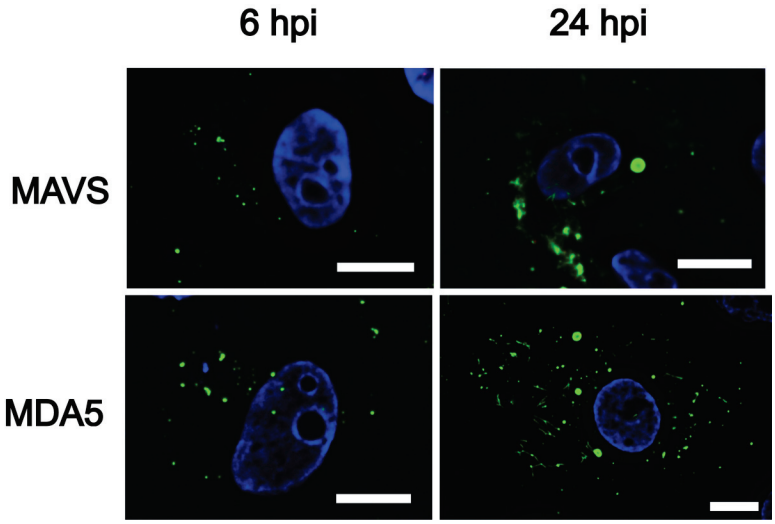

Figure 6.8: PLA gave no signal in primary antibody control cells infected with RSV. Vero cells were infected with hRSV strain A2 at an MOI=1.0 and incubated for 6 or 24 hours. Cells were stained for RSV P (green) and were assayed for the interaction between RSV N and either MDA5 or MAVS by PLA (red) without the primary antibody for hRSV N. The nucleus, stained by DAPI is colored blue. Scale bars are 10 µm.

hRSV N is in close proximity to MAVS and MDA5 but not RIG-I in the absence of viral infection.

To test whether viral replication was required for the interaction between hRSV N and the proteins of the RLR response, PLA was performed between hRSV N and MAVS or MDA5 or RIG-I in Vero cells expressing hRSV N-GFP and hRSV P or only hRSV N-GFP (**Figure 6.9** and controls in **Figure 6.10**). When hRSV N-GFP was expressed alone, it PLA signal was observed with MDA5 and MAVS, indicating that neither an active viral infection nor any other components of the virus were necessary for this reaction. (**Figure 6.9**, Row 2 & 3). In contrast, when PLA was performed between hRSV N and RIG-I, no PLA signal was observed indicating that the two were not in close proximity (**Figure 6.9**, Row 1). When hRSV N-GFP and hRSV P were co-expressed, the PLA signal was still observed between N and MAVS or MDA5; however, its localization had changed. Instead of being diffuse and cytoplasmic as in the case when hRSV N-GFP was expressed alone, the signal was predominantly around IBs when hRSV N-GFP and hRSV P were co-expressed (**Figure 6.9**, Row 5 & 6). Interestingly, even though RIG-I was present in inclusion bodies when RSV N and P were co-expressed (**Figure 6.4**), it was not in close enough proximity to give a signal from the PLA (**Figure 6.9**, Row 4). While MDA5 is soluble and available to bind to targets throughout the cytoplasm, MAVS is localized predominantly to the mitochondria. How MAVS translocated from the mitochondrial surface to IBs is unknown. However, when hRSV N-GFP was co-expressed with the hRSV P and the mitochondria were labeled with MitoTracker, we observed that the mitochondria often surrounded the IBs (**Figure 6.11**). **Figure 6.11A** shows a living cell in which the IBs formed from N and P expression were surrounded by

mitochondria. To better observe this phenomenon, a 3D isosurface view was generated (**Figure 6.11C**) from the field in **Figure 6.11B**.

To confirm that RSV N either directly or indirectly interacted as part of a larger complex with MDA5 and MAVS, both GFP-MAVS and GFP-MDA5 were co-expressed with RSV N and were immunoprecipitated using an anti-GFP antibody (**Figure 6.12**). When the precipitates were subjected to western blotting it was found that N was present in the GFP-MDA5 precipitate but not the GFP-MAVS fraction (**Figure 6.12**, Lanes 1 and 2). No primary antibody controls, were negative for the GFP-MDA5, GFP-MAVS, and RSV N proteins (**Figure 6.12**, Lanes 3 and 4).

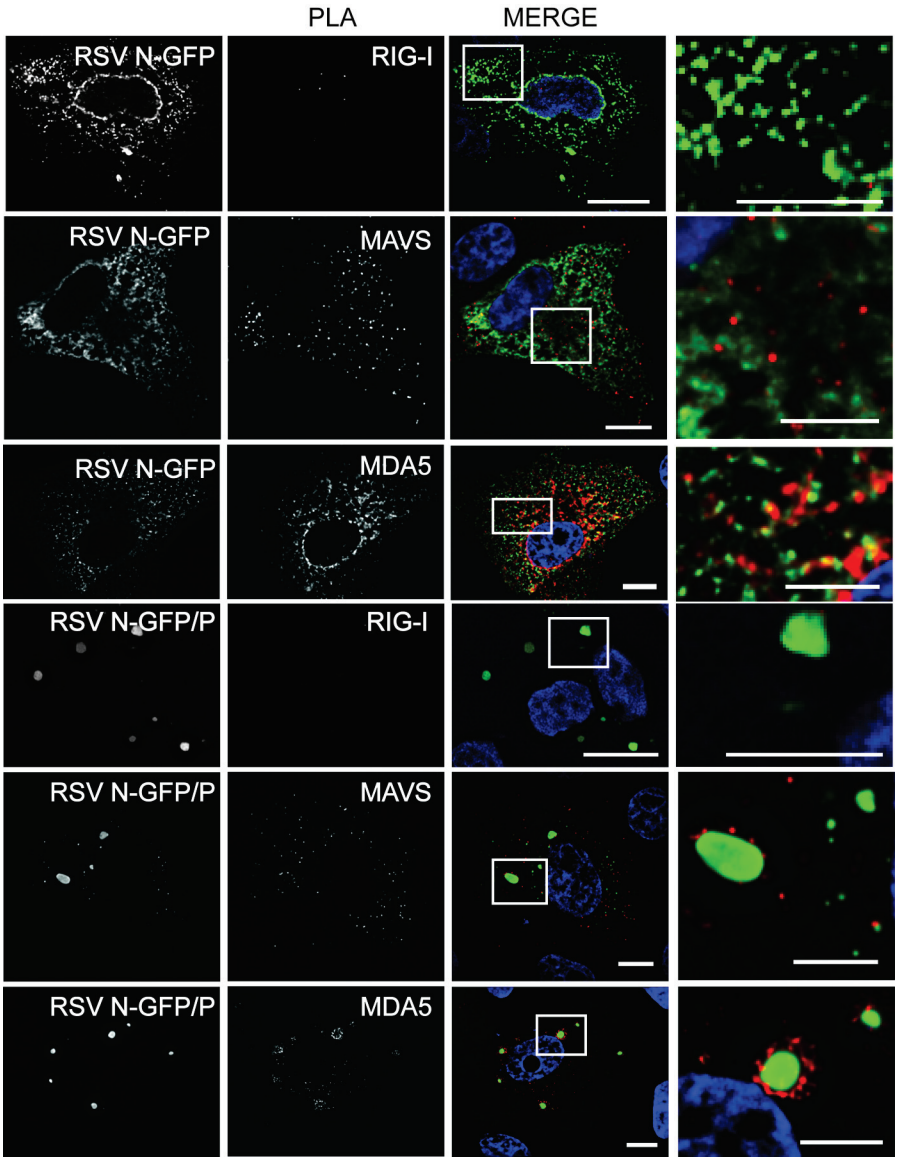

Figure 6.9: hRSV N is in proximity to MDA5 and MAVS but not RIG-I in the absence of viral infection. Vero cells were transfected with plasmids encoding either hRSV N-GFP or hRSV N-GFP and hRSV P and assayed for the interaction between hRSV N and RIG-I, MDA5 or MAVS. Column 1 shows the GFP signal from the hRSV N-GFP. Column 2 shows the PLA signal for hRSV N with RIG-I (rows 1 and 4), MAVS (rows 2 and 5) or hRSV N with MDA5 (rows 3 and 6). Column 3 shows the merge of column 1 (green) with column 2 (red) with the nucleus stained with DAPI in blue. Column 4 is a magnification of the boxed region in the panels in column 3. Scale bars in column 3 are 10 µm and in column 4 are 5 µm.

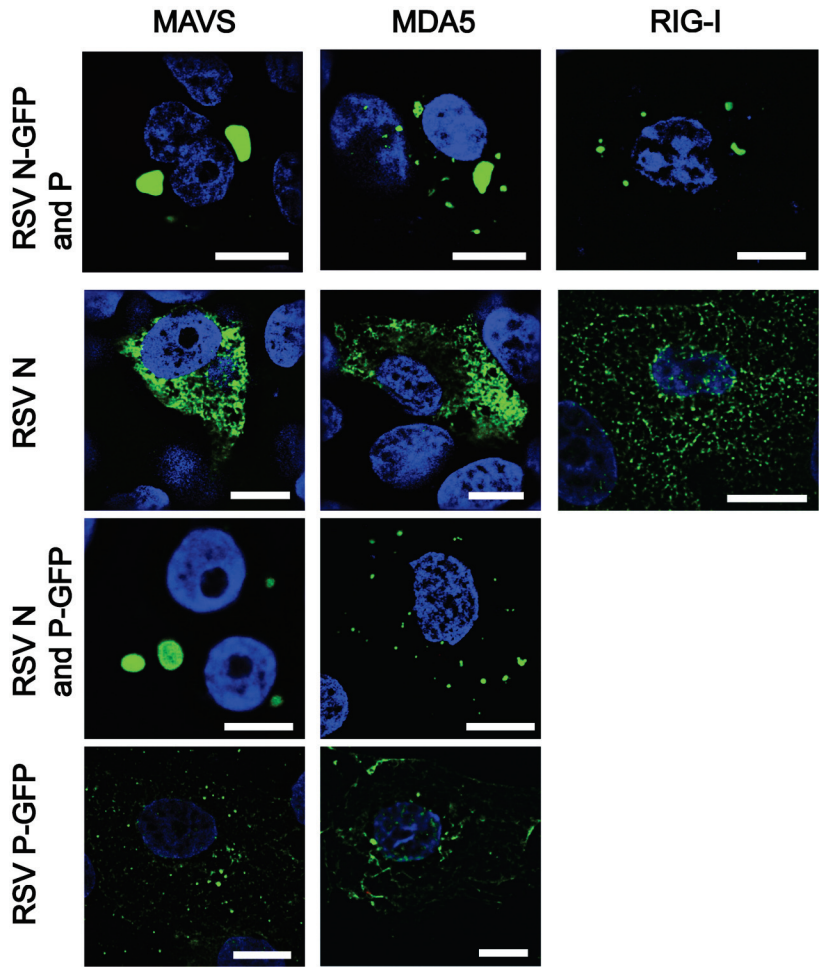

Figure 6.10. PLA gave no signal in primary antibody control cells transfected with plasmids encoding RSV N-GFP and RSV P, RSV N-GFP alone, RSV P-GFP and RSV N, or RSV P-GFP alone. Vero cells were transfected with plasmids encoding hRSV N-GFP, hRSV N-GFP and hRSV P, hRSV P-GFP, or hRSV P-GFP and hRSV N and assayed for the interaction between hRSV N and MAVS (column 1), MDA5 (column 2), or RIG-I (column 3) without the primary antibody for hRSV N. Row 1 shows cells transfected with plasmids encoding hRSV N-GFP and hRSV P. Row 2 shows cells transfected with a plasmid encoding hRSV N-GFP only. Row 3 shows cells transfected with plasmids encoding hRSV P-GFP and hRSV N. Row 4 shows cells transfected with a plasmid encoding hRSV P-GFP only. The nucleus, stained by DAPI is colored blue. Scale bars are 10 μm. Images are single planes of widefield, undeconvolved z-stacks.

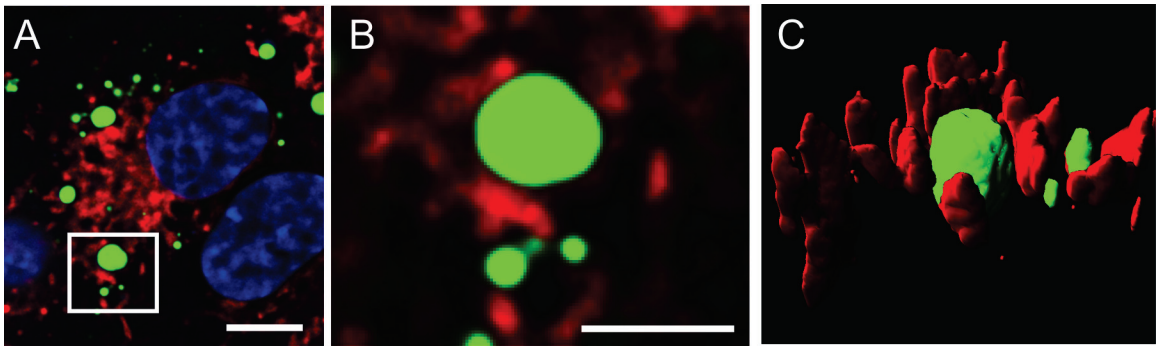

Figure 6.11. Mitochondria are found adjacent to hRSV IBs. Vero cells were transfected with plasmids encoding hRSV N-GFP and RSV P. At 24 hours post-transfection mitochondria were labeled with Mitotracker deep red 633 and imaged live. Panel A shows a single cell. Panel B is a magnification of the boxed region in panel A. Panel C is a three-dimensional, isosurface view of a large IB from panel B surrounded by mitochondira. hRSV N-GFP is colored green, Mitotracker is colored in red and nuclei, stained for with DAPI, are in blue. Scale bar in A is 10 μm and in B is 5 μm.

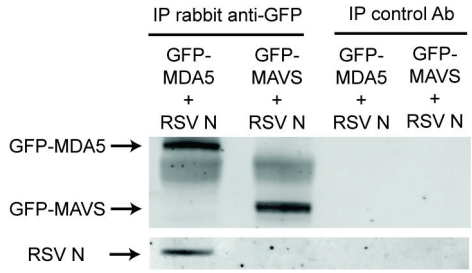

Figure 6.12: hRSV N coprecitates with GFP-MDA5. HeLa cells were transfected with plasmids encoding GFP-MDA5 and hRSV N or GFP-MAVS and hRSV N. 24 h post transfection cells were lysed and subjected to IP using an anti-GFP antibody or control antibody. Precipitates were subjected to electrophoresis and western blotting using an anti-GFP to detect the GFP-MDA5 and GFP-MAVS and an anti hRSV N antibody to detect the hRSV N. Bots were linearly contrasted enhanced.

RSV P is only in proximity to MDA5 when co-expressed with RSV N.

To test if the proximity of RSV N-GFP and MDA5 and MAVS is unique to RSV N, RSV P-GFP was expressed alone or in combination with RSV N and a PLA was performed between RSV P and MAVS or MDA5. When expressed alone, no PLA signal was observed with either MAVS or MDA5 indicating that over expression of the viral protein is not sufficient to bring the two in close proximity. When co-expressed with RSV N, PLA signal was observed between RSV P-GFP and MDA5 but not MAVS indicating that RSV P forms a complex with RSV N that brings it sufficiently close (<30 nm) to MDA5 but not MAVS. Notably, PLA between RSV P-GFP and MDA5 was exclusively observed around the periphery of IBs. This is in contrast to the PLA between RSV N-GFP and MDA5 or MAVS, which was predominantly but not exclusively localized to IBs (**Figure 6.13**).

To further test if the PLA between RSV N and cellular proteins is an artifact of overexpression of the viral protein, a PLA was performed between RSV N, without the GFP fusion) and a co-expressed GFP control plasmid, which expresses a cytoplasmic, diffusely localized GFP. No PLA signal was observed indicating that even over-expression of both proteins is insufficient to give a PLA signal if they do not interact. A positive control, RSV N-GFP expression and intramolecular PLA between the RSV N and GFP domains, demonstrated a high level of PLA signal (**Figure 6.14**).

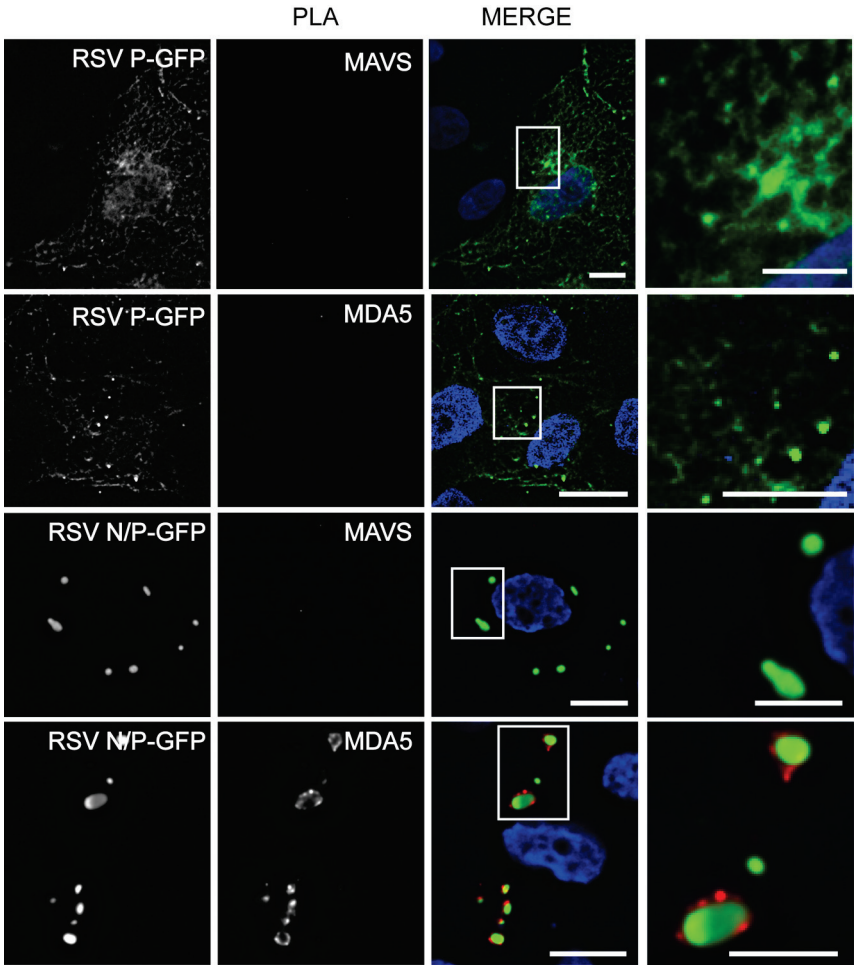

Figure 6.13: hRSV P is in proximity to MDA5 and MAVS in the absence of viral infection. Vero cells were transfected with plasmids encoding either hRSV P-GFP or hRSV P-GFP and hRSV N and assayed for the interaction between hRSV P and MDA5 or MAVS. Column 1 shows the GFP signal from the hRSV P-GFP. Column 2 shows the PLA signal for hRSV P with MAVS (rows 1 and 3) or hRSV N with MDA5 (rows 2 and 4). Column 3 shows the merge of column 1 (green) with column 2 (red) with the nucleus stained with DAPI in blue. Column 4 is a magnification of the boxed region in the panels in column 3. Scale bars in column 3 are 10 µm and in column 4 are 5 µm.

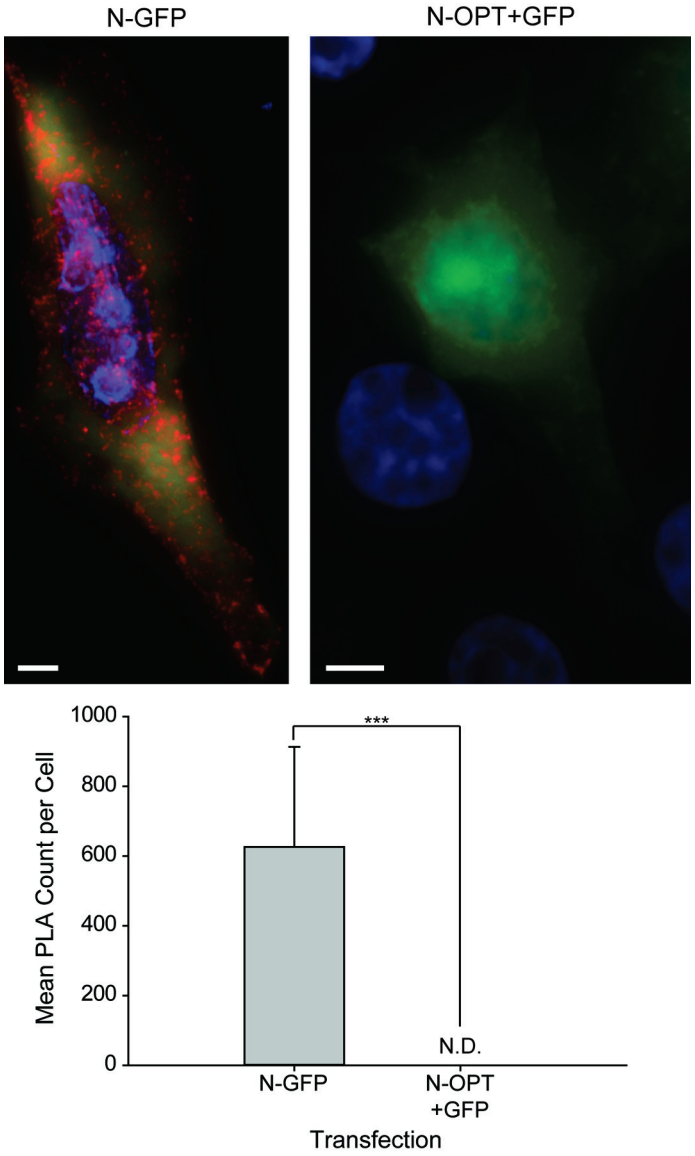

Figure 6.14: PLA produces a signal in the presence of interacting antigens but not in diffusely localized, noninteracting antigens. Vero cells were transfected with plasmids encoding either hRSV N and free GFP (N-OPT + GFP) or hRSV N-GFP alone (N-GFP). A PLA was performed against the GFP and hRSV N domains in both cases. PLA signal was quantified on a per cell basis and summarized. Nuclei were stained with DAPI.. ***=P≤0.001. N.D. = not detected. GFP signal is shown in green, PLA signal is shown in red, and DAPI signal is shown in blue. Scale bars are 10 μm. Error bars are s.d.

Expression of hRSV N and co-expression of hRSV N and P resulted in the attenuation of interferon response.

Given the data presented above, we hypothesized that the interaction of hRSV N with MAVS and MDA5 and the sequestration of these proteins into IBs during infection may cause a decrease in the expression of type 1 interferons, and specifically interferon β. To test this hypothesis, we transfected HeLa cells with either, a GFP control expression plasmid, hRSV N-GFP alone, hRSV P-GFP alone, or co-transfected with hRSV N-GFP and P. The cells were subsequently inoculated with the LaSota strain of Newcastle disease virus (NDV), a pathogen known to induce an interferon response through the RLR pathway in HeLa cells (Yoneyama, Kikuchi et al. 2004). At 24 hours after NDV inoculation, total RNA was isolated from the cells, and interferon β (IFNB1) mRNA was quantified relative to β-actin (ACTB) mRNA using reverse transcriptase real-time PCR (**Figure 6.15**). Cells transfected with either hRSV N-GFP or hRSV N-GFP and P and infected with NDV expressed IFNB1 at a level 27 times lower than in cells transfected with GFP control plasmid and infected with NDV (**Figure 6.15B**). When lower amounts of hRSV N-GFP DNA were transfected into the cells, the effect of hRSV N on interferon expression was diminished, in a dose dependent fashion. In addition, the expression of the P alone, had no effect on IFNB1 expression, as suggested by the PLA data (**Figure 6.15B**). These data indicated that the effect of hRSV N on the innate immune response lowers the production of IFNB1 when hRSV N is present as both a diffuse population throughout the cytoplasm and when it is localized to cytoplasmic IBs.

In untransfected HeLa cells, NDV infection caused IFNB1 expression to increase 150,000-fold at 24 hpi relative to uninfected, untransfected HeLa cells. In cells that had

been transfected with a GFP control plasmid, NDV infection caused IFNB1 expression to increase 5,000-fold when infected with NDV, relative to uninfected HeLa cells transfected with GFP. The difference in IFNB1 expression may be due to the transfection process via Lipofectamine 2000. To test if this was the case, cells were treated with the transfection agent alone and infected with NDV. As can be seen in **Figure 6.15A**, the transfection agent, without DNA, reduced the susceptibility of the cells to IFN induction when infected with NDV. While this reduces the overall effect of the sequestration of RLR components on the induction of IFNB1 by NDV in cells expressing hRSV N, there is still a sizable difference (~27-fold) when compared to cells expressing GFP alone. In cells transfected with GFP alone, NDV infection caused IFNB1 expression to increase 27,000-fold relative to the amount in control HeLa cells (no transfection, no infection) and 5,000-fold relative to cells that were transfected with GFP and infected with NDV.

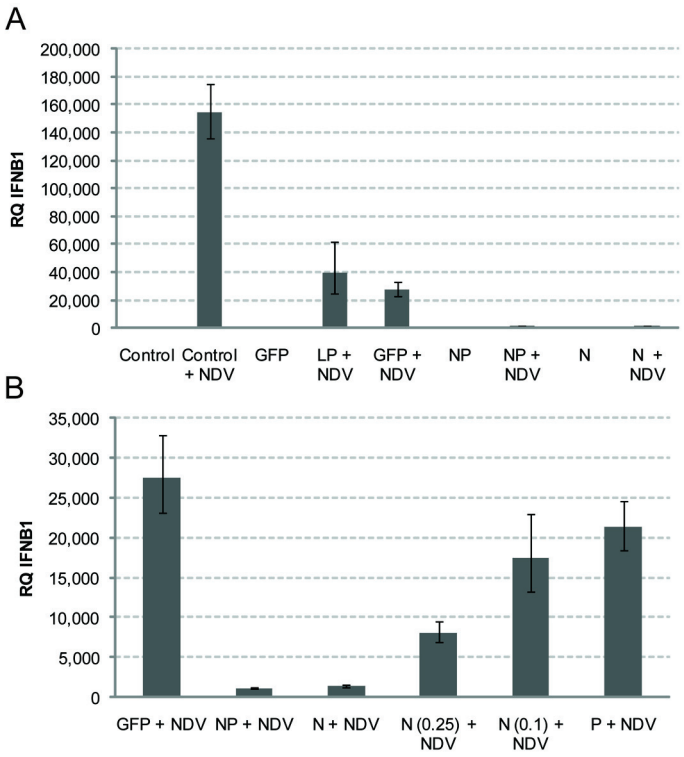

Figure 6.15: hRSV N expressed alone or with hRSV P functions to diminish interferon expression in response to infection. HeLa cells were either untransfected (control), mock transfected with Lipofectamine 2000 (LP), transfected with 2 µg of a GFP expressing plasmid (GFP), hRSV N expressing plasmid (N), hRSV P expressing plasmid (P), or both a hRSV P expressing plasmid and a hRSV N expressing plasmid (NP). After 24 hours, cells were left uninfected or were infected with NDV LaSota strain (+ NDV). At 24 hours post-infection cells were harvested for RNA and qRT-PCR was performed for IFNB1 using ACTB as a loading control. Panel A shows experimental and control cases. Panel B shows selected data from A rescaled along with hRSV P and a titration of the hRSV N plasmid of one quarter the amount of DNA (0.25) and one tenth the amount of DNA (0.1). Error bars are min and max relative quantification (RQ).

Discussion

The experiments presented here demonstrate that one function of the large hRSV inclusion bodies might be to modulate the innate immune response to infection. Although previous experiments have implicated the nonstructural hRSV proteins NS1 and NS2 as modulators of the innate immune response, we demonstrated here that the N protein itself may be involved in that process (Bossert and Conzelmann 2002; Bossert, Marozin et al. 2003; Ling, Tran et al. 2009). We studied the role of hRSV N and IBs in modulating the RLR induced interferon response by colocalization analysis, proximity ligation assay, immunoprecipitation, and by a bioassay using an infection with Newcastle disease virus. We determined that RIG-I, MDA5, and MAVS colocalized with small and large hRSV IBs and that MDA5 and MAVS localized with hRSV N both inside IBs and when expressed diffusely within the cytoplasm. Furthermore, we demonstrated that hRSV N, both expressed diffusely and in IBs, significantly attenuated the interferon response induced by Newcastle disease virus infection in a dose dependent fashion.

Cytoplasmic IBs, first observed by transmission electron microscopy (TEM), are likely aggregates of N proteins (Norrby, Marusyk et al. 1970; Norrby, Marusyk et al. 1970). Despite the considerable body of knowledge in the molecular biology of hRSV, little is known about the composition, structure, and function of IBs. Previous studies have examined the viral content of IBs and the viral proteins necessary for their formation. It was found that expression of hRSV proteins N and P is sufficient and necessary for the formation of IB-like structures (Garcia, Garcia-Barreno et al. 1993). hRSV proteins M, M2-1, and L, when expressed with N and P, also are localized to IBs, while hRSV G and F, which are translated in the ER, do not appear to be present in large

inclusion bodies, but instead have been shown to interact with viral filaments and small IBs or granules close to the plasma membrane (Ghildyal, Mills et al. 2002).

Current and past studies on the localization of hRSV proteins and genomic RNA have shown the important role of imaging methods in the analysis of viral localization and structure. Even so, there is still little known about the heterogeneity of granules and IBs with respect to time, size or function. Here we showed that hRSV genomic RNA is predominantly localized to small IBs or granules (<1.0 μm^3) throughout the course of infection and to viral filaments during their formation later in the infection ~24 hpi. Contrastingly, even though larger IBs (>8 μm^3), contain large quantities of N protein, which is known to complex with viral RNA to form nucleocapsids, they contain little if any genomic RNA, suggesting that this class of IB is likely not the site of viral replication.

By immunofluorescence microscopy, large IBs often are shown to have an open or hollow structure with stronger staining around the periphery of the IB (Garcia, Garcia-Barreno et al. 1993; Carromeu, Simabuco et al. 2007; Lindquist, Lifland et al. 2010). The reason for this structure is unknown, but it is likely an artifact of immunofluorescence, since expressed IBs generated by hRSV N-GFP and hRSV P appear solid by examination of the GFP signal (**Figure 6.16**); when imaged by TEM, IBs appear solid and uniform (Norrby, Marusyk et al. 1970; Norrby, Marusyk et al. 1970; Roberts, Compans et al. 1995; Jeffree, Brown et al. 2007). Given we have successfully immunostained for proteins within the larger IBs, it is unlikely that the hollow staining pattern is due solely to limited antibody diffusion in fixed IBs. Instead, we propose that this pattern is caused by epitope inaccessibility due to interactions with host proteins. The structure of the N

protein-RNA complex of hRSV has been solved, however, the structure of IBs generated by the expression of hRSV N and P has not (Tawar, Duquerroy et al. 2009). The structure of IBs, examined in the future at the nanoscale, may yield clues to the overall functionality of IBs.

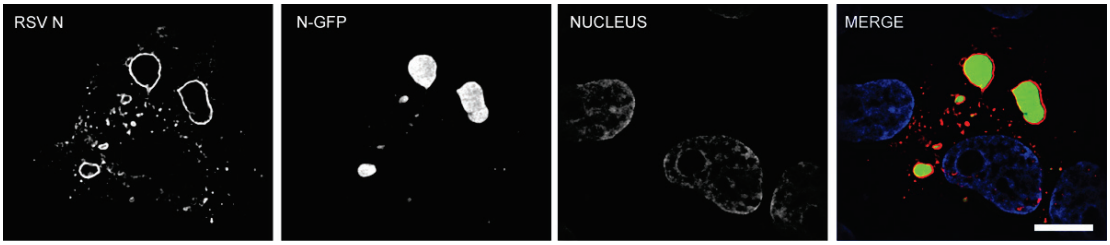

Figure 6.16: Immunofluorescence staining of expressed IBs yields an open ring-shaped structure. Vero cells were transfected with plasmids expressing hRSV N-GFP fusion and hRSV P proteins and immunostained for hRSV N. The nucleus was stained by DAPI. The merge panel shows the overlay of RSV N immunostaining (red), N-GFP (green) and the nucleus (blue). The image is a XY plane through the center of the largest inclusion bodies. Scale bars are 10 μm.

Here we suggest that IBs localize proteins of the innate immune response in order to decrease downstream interferon signaling. We demonstrated in a model of hRSV infection that early in the infection, MAVS and MDA5 are localized to small IBs or granules that contain hRSV N and genomic RNA. At later time points, these innate immune molecules are localized to larger IBs that contain little if any genomic RNA and to viral filaments that also contain genomic viral RNA. In both of these cases, the colocalization between the cellular proteins and hRSV N was confirmed by proximity ligation assay (PLA). We further showed that both the colocalization in large IBs and the PLA results were independent of viral infection by expressing hRSV N and P *in trans,* and therefore these findings were not a result of MDA5 interaction with the viral RNA. Finally, we demonstrated, by immunoprecipitation, that hRSV N either directly or indirectly interacted with MDA5. Overall, the picture generated by our data suggests that N interacts with both MDA5 and P within a macromolecular complex. It also suggests that MAVS is a part of this complex, in close proximity to N, but not within 30-40 nm of P.

The innate immune response to RNA virus infections proceeds through two pathways, via RIG-I like helicases, including RIG-I and MDA5, and the TLR pathway. Both of these pathways result in the induction of interferon production. The RIG-I like proteins require an intermediary protein MAVS (also known as IPS-1, VISA, and Cardif), which binds to RIG-I like helicases through a CARD domain. MAVS initiates a signaling cascade by activating cytosolic kinases IKK and TBK1, which then activates transcription factors NF-κB and IRF3. These transcription factors translocate to the nucleus where they promote the expression of type I interferons. In hRSV, the interferon

response has been shown to play an important role in the nature and severity of the disease (Johnson, Mertz et al. 2005). MDA5 and RIG-I have both been found to be upregulated in infants infected with hRSV compared to infants that have not been infected.

The finding that MDA5 is efficiently localized into IBs may explain why RIG-I has been shown to have a larger effect on the innate immune response to hRSV infection (Loo, Fornek et al. 2008). The data also suggest a mechanism by which cells can be potentiated toward subsequent infection or co-infection. We have shown that the expression of IBs by hRSV localizes pattern recognition receptors of the RLR pathway and additionally localized their downstream effector MAVS. We demonstrated that N and IBs alone, and not P alone, are enough to diminish the cell's ability to produce interferon in response to a viral infection. To our knowledge this is the first report of hRSV IBs having a functional role in the life cycle of the virus. It is important to note that while cytoplasmic, diffuse hRSV N expression can decrease the interferon response without the formation of the inclusion bodes, *in vivo* hRSV N is highly localized to IBs (Li, Jans et al. 2008).

In summary, there is little previous data describing the host cell protein content inside IBs or their precise function. The study presented here suggests an interaction of hRSV N protein with important host proteins of the innate immune response and a specific function for inclusion bodies. The findings also clearly point to the need for further studies regarding IB formation, structure and function in terms of time and space during hRSV infections.

References

Barbalat, R., S. E. Ewald, et al. (2011). "Nucleic acid recognition by the innate immune system." Annual review of immunology **29**: 185-214.

Bitko, V., O. Shulyayeva, et al. (2007). "Nonstructural proteins of respiratory syncytial virus suppress premature apoptosis by an NF-kappaB-dependent, interferon-independent mechanism and facilitate virus growth." Journal of virology **81**(4): 1786-1795.

Bossert, B. and K. K. Conzelmann (2002). "Respiratory syncytial virus (RSV) nonstructural (NS) proteins as host range determinants: a chimeric bovine RSV with NS genes from human RSV is attenuated in interferon-competent bovine cells." Journal of virology **76**(9): 4287-4293.

Bossert, B., S. Marozin, et al. (2003). "Nonstructural proteins NS1 and NS2 of bovine respiratory syncytial virus block activation of interferon regulatory factor 3." Journal of virology **77**(16): 8661-8668.

Carromeu, C., F. M. Simabuco, et al. (2007). "Intracellular localization of human respiratory syncytial virus L protein." Archives of virology **152**(12): 2259-2263.

Garcia-Barreno, B., T. Delgado, et al. (1996). "Identification of protein regions involved in the interaction of human respiratory syncytial virus phosphoprotein and nucleoprotein: significance for nucleocapsid assembly and formation of cytoplasmic inclusions." J Virol **70**(2): 801-808.

Garcia, J., B. Garcia-Barreno, et al. (1993). "Cytoplasmic inclusions of respiratory syncytial virus-infected cells: formation of inclusion bodies in transfected cells that coexpress the nucleoprotein, the phosphoprotein, and the 22K protein." Virology **195**(1): 243-247.

Ghildyal, R., D. Li, et al. (2005). "Interaction between the respiratory syncytial virus G glycoprotein cytoplasmic domain and the matrix protein." The Journal of general virology **86**(Pt 7): 1879-1884.

Ghildyal, R., J. Mills, et al. (2002). "Respiratory syncytial virus matrix protein associates with nucleocapsids in infected cells." J Gen Virol **83**(Pt 4): 753-757.

Jeffree, C. E., G. Brown, et al. (2007). "Ultrastructural analysis of the interaction between F-actin and respiratory syncytial virus during virus assembly." Virology **369**(2): 309-323.

Johnson, T. R., S. E. Mertz, et al. (2005). "Role for innate IFNs in determining respiratory syncytial virus immunopathology." Journal of immunology **174**(11): 7234-7241.

Kurt-Jones, E. A., L. Popova, et al. (2000). "Pattern recognition receptors TLR4 and CD14 mediate response to respiratory syncytial virus." Nat Immunol **1**(5): 398-401.

Li, D., D. A. Jans, et al. (2008). "Association of respiratory syncytial virus M protein with viral nucleocapsids is mediated by the M2-1 protein." Journal of virology **82**(17): 8863-8870.

Lindquist, M. E., A. W. Lifland, et al. (2010). "Respiratory syncytial virus induces host RNA stress granules to facilitate viral replication." J Virol **84**(23): 12274-12284.

Ling, Z., K. C. Tran, et al. (2009). "Human respiratory syncytial virus nonstructural protein NS2 antagonizes the activation of beta interferon transcription by interacting with RIG-I." Journal of virology **83**(8): 3734-3742.
Liu, P., M. Jamaluddin, et al. (2007). "Retinoic acid-inducible gene I mediates early antiviral response and Toll-like receptor 3 expression in respiratory syncytial virus-infected airway epithelial cells." Journal of virology **81**(3): 1401-1411.
Loo, Y. M., J. Fornek, et al. (2008). "Distinct RIG-I and MDA5 signaling by RNA viruses in innate immunity." Journal of virology **82**(1): 335-345.
Mogensen, T. H. (2009). "Pathogen recognition and inflammatory signaling in innate immune defenses." Clinical microbiology reviews **22**(2): 240-273.
Norrby, E., H. Marusyk, et al. (1970). "Morphogenesis of respiratory syncytial virus in a green monkey kidney cell line (Vero)." J Virol **6**(2): 237-242.
Norrby, E., H. Marusyk, et al. (1970). "Ultrastructural studies of the multiplication of RS (respiratory syncytial) virus." Acta Pathol Microbiol Scand [B] Microbiol Immunol **78**(2): 268.
Roberts, S. R., R. W. Compans, et al. (1995). "Respiratory syncytial virus matures at the apical surfaces of polarized epithelial cells." J Virol **69**(4): 2667-2673.
Santangelo, P. J. and G. Bao (2007). "Dynamics of filamentous viral RNPs prior to egress." Nucleic Acids Res **35**(11): 3602-3611.
Santangelo, P. J., A. W. Lifland, et al. (2009). "Single molecule-sensitive probes for imaging RNA in live cells." Nat Methods **6**(5): 347-349.
Seth, R. B., L. Sun, et al. (2005). "Identification and characterization of MAVS, a mitochondrial antiviral signaling protein that activates NF-kappaB and IRF 3." Cell **122**(5): 669-682.
Soderberg, O., M. Gullberg, et al. (2006). "Direct observation of individual endogenous protein complexes in situ by proximity ligation." Nat Methods **3**(12): 995-1000.
Soderberg, O., K. J. Leuchowius, et al. (2008). "Characterizing proteins and their interactions in cells and tissues using the in situ proximity ligation assay." Methods **45**(3): 227-232.
Swedan, S., J. Andrews, et al. (2011). "Multiple functional domains and complexes of the two nonstructural proteins of human respiratory syncytial virus contribute to interferon suppression and cellular location." Journal of virology **85**(19): 10090-10100.
Tawar, R. G., S. Duquerroy, et al. (2009). "Crystal structure of a nucleocapsid-like nucleoprotein-RNA complex of respiratory syncytial virus." Science **326**(5957): 1279-1283.
Utley, T. J., N. A. Ducharme, et al. (2008). "Respiratory syncytial virus uses a Vps4-independent budding mechanism controlled by Rab11-FIP2." Proc Natl Acad Sci U S A **105**(29): 10209-10214.
Yoboua, F., A. Martel, et al. (2010). "Respiratory syncytial virus-mediated NF-kappa B p65 phosphorylation at serine 536 is dependent on RIG-I, TRAF6, and IKK beta." Journal of virology **84**(14): 7267-7277.
Yoneyama, M., M. Kikuchi, et al. (2004). "The RNA helicase RIG-I has an essential function in double-stranded RNA-induced innate antiviral responses." Nature immunology **5**(7): 730-737.

CHAPTER 7

POLYETHYLENE GLYCOL CORE PROBES

Background

In recent years, the imaging of RNAs in live cells has garnered growing attention with a variety of interesting methods developed for this purpose. This research has been driven by the increased appreciation for the role of post-transcriptional regulation on the function of RNA molecules (Anderson and Kedersha 2009), for the role of genomic RNA in viral assembly, and for the stress response of cells in pathogenesis (Beckham and Parker 2008). From previous research on RNA imaging methods, several design criteria have emerged. Imaging methods must be sensitive enough to detect RNA molecules, which are generally present in low copy numbers, and to enable the tracking of single RNA granules over time in live cells. For probe-based methods, delivery into the correct cellular compartment is critical in order for the probes to bind rapidly to their target. Delivery methods that result in accumulation of probe in the nucleus of cells or utilize endocytic vesicles can lead to nonspecific signal and degradation of the probe.

Single molecule imaging of native and nonengineered RNAs in live cells has recently been achieved by the use of multiply labeled tetravalent RNA imaging probes (MTRIPs) (Santangelo, Lifland et al. 2009). These probes consist of four fluorescently labeled linear oligonucleotides bound together by a biotin−streptavidin linkage and recognize their intracellular target RNA through Watson−Crick base pairing. Signal is raised above background by the binding of 2−3 probes per target RNA and through the natural localization of the target RNA. Prior to the introduction of MTRIPs, single

molecule studies of specific RNA localization and transport in live cells were limited to plasmid derived RNAs either containing binding site repeats for the MS2-GFP fusion protein (Fusco, Accornero et al. 2003) or containing binding site repeats for a molecular beacon (Vargas, Raj et al. 2005). Plasmid derived RNAs offer tremendous methodological flexibility, but they preclude the study of native RNA or nonengineered viral RNA and do not allow for imaging native RNAs in vivo.

While MTRIPs have proven to be capable of targeting a number of RNAs in various cell types with single RNA sensitivity, the use of a streptavidin core imparts some limitations. Probes with a streptavidin core have a maximum of four noncovalently bound ligands, which limits the number of fluorophores that can be added to a single probe. Streptavidin also contributes significantly to the molecular weight of the probe (53 kDa) and might affect the delivery pathway during cell penetrating peptide-mediated delivery (Rinne, Albarran et al. 2007).

Here, we report the synthesis and application of a multivalent RNA imaging probe that utilizes an eight-armed poly(ethylene glycol) (PEG) core. These probes overcome the main limitations imposed by streptavidin by increasing the number of bound ligands while reducing the molecular weight of the core (20 kDa). Moreover, the probes are stabilized by employing a covalent bond between the ligand and the core. PEG was chosen, since it has been shown to reduce toxicity, reduce nonspecific binding, and improve internalization when conjugated to macromolecules and utilized in vivo (Suzuki, Kanbara et al. 1984; Rapozzi, Cogoi et al. 2002; Healy, Lewis et al. 2004).

In order to demonstrate the efficiency of probe delivery and targeting, we utilized the genomic viral RNA (vRNA) of human respiratory syncytial virus (hRSV) as a model system. The localization of the vRNA of hRSV has been previously characterized by both molecular beacons and MTRIPs and showed high concentrations of viral RNA in cytoplasmic foci termed inclusion bodies (Santangelo, Nitin et al. 2006; Santangelo and Bao 2007; Santangelo, Lifland et al. 2009). Delivery of probe into live cells was achieved using reversible membrane permeabilization with streptolysin O (SLO), which has been shown to allow for efficient and homogeneous delivery of macromolecules into the cytoplasm (Santangelo, Lifland et al. 2009).The use of SLO results in probe delivery efficiency and results in minimal cytotoxicity (Santangelo, Lifland et al. 2009). Alternatively, as a delivery strategy, we also used the cell penetrating peptide (CCP) TAT, which, when conjugated to macromolecules, has been shown to transduce them across the plasma membrane (Nitin, Santangelo et al. 2004). Indeed, the use of the PEG core permits an increase in the number of bound ligands and allows for the conjugation of delivery and targeting peptides along with RNA targeting oligonucleotides, while maintaining single molecule sensitivity. CPP-conjugated probes are currently of great interest in molecular imaging, since they have the advantage of being suitable for use in vivo when labeled with near-infrared fluorophores. As with SLO, CPP based delivery allows for 100% delivery efficiency and low cytotoxicity at low concentrations and eliminates the need for permeabilization of the membrane, reducing the complexity of the experimental procedure (Tunnemann, Ter-Avetisyan et al. 2008).

Materials and Methods

Multivalent PEG Probes

2′-O-Me RNA/DNA chimeric oligonucleotides were synthesized by Biosearch Technologies, Inc. (Novato, CA) with the following sequence, 5′-**U**XTXTTX**<u>AAAAAXGGGGCAAAXAA</u>**-3′, where the boldface type is 2′-*O*-Methyl RNA, the X is a dT-C6-NH2 (**Figure 7.1**), the 5′-**U** contains a free thiol group (**Figure 7.2**), and all others are DNA. The binding region is underlined. Probes were synthesized by first labeling the individual ligands with amine reactive NHS-ester fluorophores Atto 488 (ATTO-TEC GmbH), Cy3B (GE Healthcare), or Atto 647N (ATTO-TEC GmbH) using the manufacturer's protocols. Ligands were subsequently linked to 20 kDa eight-armed maleimide poly(ethylene glycol) (8-Arm PEG) cores (**Figure 7.3**) (NOF America) by incubation in a 64:1 molar ratio in PBS (Ambion) and 1 mM EDTA (Ambion) for 12 h at room temperature. 8-Armed PEG probes with TAT were synthesized by adding ligand, Cys-TAT (Anaspec, Cys-TAT 47−57), and 8-Arm-PEG cores in a 64:8:1 molar ratio in 10× PBS, and 1 mM EDTA for 12 h at room temperature. All probes were filtered to remove free ligand and reaction buffer using 30 kDa molecular weight cutoff Nanosep centrifugal devices (Pall Corp.). Purified probes were resuspended in nuclease free PBS and stored at 4 °C.

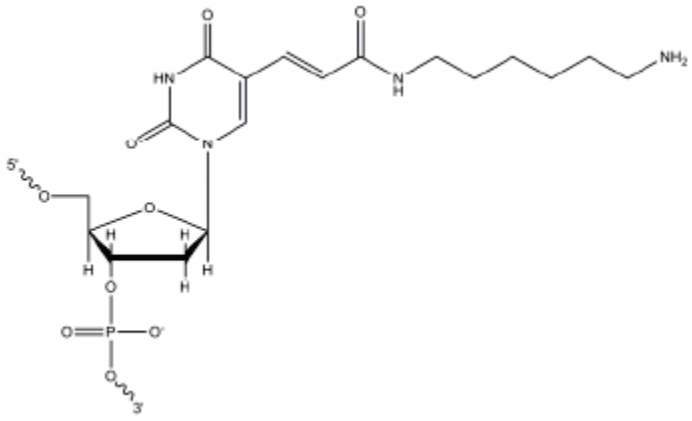

Figure 7.1: Structure of the internal amine modified thymidines.

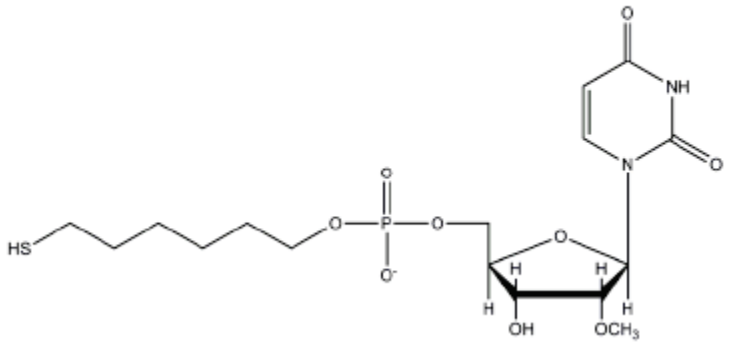

Figure 7.2 Structure of the 5′ thiol modified 2′-O-Methyl Uridine

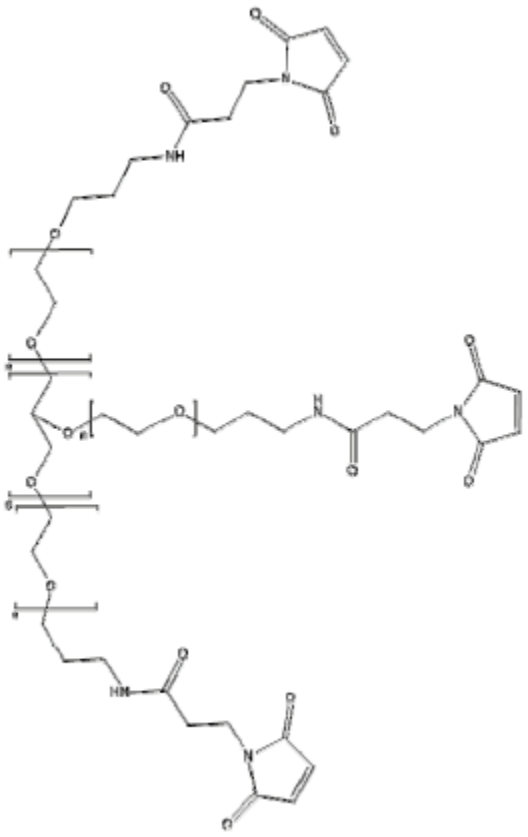

Figure 7.3: Structure of the 8-Arm maleimide activated PEG

Cells and Virus

A549 human lung carcinoma cells (ATCC CCL-185) were cultured in DMEM (Lonza) with 10% FBS (Hyclone), 100 U/mL penicillin, and 100 U/mL streptomycin (Invitrogen). Cells were plated on glass coverslips one day prior to experiments. The A2 strain of human respiratory syncytial virus (hRSV) (Crowe laboratory, Vanderbilt University) was used at a MOI = 1 and a titer of $1 \times 10^6 TCID_{50}$ mL^{-1}.

Probe Delivery

Probes were delivered into A549 cells using reversible membrane permeabilization and peptide mediated delivery. For reversible membrane permeabilization, 2 U/mL Streptolysin O (SLO) (Sigma) were first reduced using 7.5 mM Tris(2-carboxyethyl)phosphine (TCEP) (Peirce) for 1 h at 37 °C. Infected and noninfected cells were rinsed using PBS ($-Ca^{2+}$ $-Mg^{2+}$) (Thermo) and then incubated with delivery medium containing 0.2 U/mL SLO and 5 nM probe in PBS ($-Ca^{2+}$ $-Mg^{2+}$) for 10 min at 37 °C. The delivery medium was then removed and replaced with complete growth media for 15 min. For TAT mediated delivery of probes, infected and noninfected cells were incubated in complete medium containing 5 nM TAT conjugated probe for 10 min at 37 °C, after which it was replaced with complete medium for 15 min. For live cell imaging experiments, growth media was replaced with Leibovitz's L15 medium (Invitrogen) immediately prior to image acquisition.

Immunostaining

After probe delivery, cells were rinsed in PBS (Ambion), fixed with 4% paraformaldehyde (Electron Microscopy Science) in PBS, permeabilized using 0.2% Triton-X 100 (Sigma), and blocked with 5% bovine serum albumin (Ambion). Cells were

then incubated with a mouse monoclonal primary antibody against the hRSV N Viral Protein (Abcam), CD63 (Developmental Studies Hybridoma Bank), or LAMP-1 (Developmental Studies Hybridoma Bank) for 30 min at 37 °C and with a goat antimouse secondary antibody labeled with Alexa 488 (Invitrogen) for 30 min at 37 °C. After DAPI staining (Invitrogen), cells were mounted on slides using PVA with DABCO (Sigma).

Fluorescence Imaging

Samples were imaged using a Zeiss Axiovert 200 M epifluorescent microscope with a 63×/1.4 NA Plan-Apochromat objective, using Chroma 49002 ET-GFP (FITC/Cy2), 49004 ET Cy3, 49006 ET Cy5 filter sets, an EXFO excite 120 for fluorescence excitation, a Polytek PI objective piezo for taking stacks of images, and a Hamamatsu ORCA-ER AG for capturing digital images. Image *z*-stacks were acquired in 200 nm steps using Volocity (Improvision). Exposure times for probes on glass (**Figure 7.5**) were approximately 500 ms. Exposure times for probes in endosomal and lysosomal marker colocalization studies were 400 ms for noninfected cells (Figure 3c,d) and 30 ms for infected cells (**Figure 7.6 e,f**). Exposure times for RSV vRNA in infected cells and controls, both fixed and live, were approximately 100 ms (**Figure 7.7−7.8**). Identical exposure times in Figure 7.7 and 7.8 were used for comparison of intensities.

Image Analysis

All images were deconvolved using the iterative restoration algorithm in *Volocity*. Histograms of mean fluorescence intensity were generated by identifying objects with minimum and maximum intensities set to 4 SD and 100 SD, respectively. Objects smaller than 1 point spread function were removed. Intensity Profiles were generated using *ImageJ* (NIH) Color Profiler plug-in and data tables were imported into *Sigma Plot*

11 (Systat Software Inc.) for plotting. Manders overlap coefficient was calculated using *Volocity* software.

Determination of the Degree of Labeling

The degree of labeling (DOL) of the oligonucleotides, i.e. the average number of dyes per oligonucleotide, was determined by measuring the UV-VIS spectrum of the conjugate solution in a quartz cuvette in order to obtain the absorbance at the absorption maximum of the dye and at 260 nm. The concentrations of the oligonucleotides and the dyes were calculated using the Lambert-Beer law and the extinction coefficients provided by the manufacturers (**Figure 7.9a**). The average number of labeled oligonucleotides per activated PEG was estimated by measuring the conjugate absorbance at the absorption maximum of the dye and dividing it by the previously determined DOL (**Figure 7.9b**). The same procedure was used to determine the average number of labeled oligonucleotides conjugated to the PEG-TAT probes (**Figure 7.9c**). The average number of TAT peptides per PEG molecule was determined by absorption spectroscopy after conjugation to PEG of unlabeled oligonucleotides and fluorescein-labeled Cys-TAT (Cys-TAT-FAM, Anaspec) (**Figure 7.9d**).

In order to validate our estimation of probe concentrations and ensure that unconjugated oligonucleotides were adequately removed upon filtration, gel electrophoresis was performed (**Figure 7.10**) using 15% TBE-UREA gels according to manufacturer's protocols (Invitrogen). Analysis showed that less than 10% of the unbound oligonucleotides contribute to the absorption spectroscopy measurements after filtration. Unfortunately, gel electrophoresis did not prove to be useful to investigate the

homogeneity of the conjugates, due to the lack of clear bands. However, analysis of the microscopy data in Figure 2 showed that the mean fluorescence intensity of single probes had a measured standard deviation of about 5% of themean.

Probe synthesis

hRSV specific ligands were composed of 2′-O-Methyl-RNA and DNA chimeric oligonucleotides with five amine-modified thymidines and a 5′ thiol modification (**Figure 7.1 and 7.2**). The oligonucleotide sequence was designed to be complementary to a gene-end-intergenic-gene-start sequence of hRSV which has three exact repeats in the hRSV genome and is not present in the human genome. The sequence used has previously been shown to be accessible by antisense knockdown experiments, molecular beacon imaging, and MTRIP imaging (Player, Barnard et al. 1998; Santangelo and Bao 2007; Santangelo, Lifland et al. 2009). The targeting of three repeats per RNA raises signal significantly above background for even a single RNA per point spread function.

The amine-modified thymidines of the ligands were used to conjugate NHS-ester fluorophores, and the thiol group was used to link the individual ligands to the PEG cores, which were functionalized with eight maleimide active groups (**Figure 7.4 and Figure 7.3**). Absorption spectroscopy showed that, on average, 3 dyes were conjugated to each ligand and 6.5 ligands were conjugated to each PEG core **Figure 7.9**. Probes utilizing the TAT CPP contained an average of 4 oligonucleotides ligands and 1 TAT peptide **Figure 7.9**. By increasing the brightness of the probes through the use of multiple ligands, rather than increasing the number of fluorophores per ligand, self-quenching was minimized and ligand size was kept to approximately 20 bases. The fluorophores (Atto

488, Cy3B, and Atto 647N) were chosen for their strong absorption in visible wavelengths commonly used for imaging, high quantum efficiency, and low triplet state excitation. The use of ligands with a 2′-O-Methyl backbone conferred increased affinity for the target mRNA, increased signal-to-noise ratio, and nuclease resistance (Sproat, Lamond et al. 1989; Majlessi, Nelson et al. 1998; Molenaar, Marras et al. 2001).

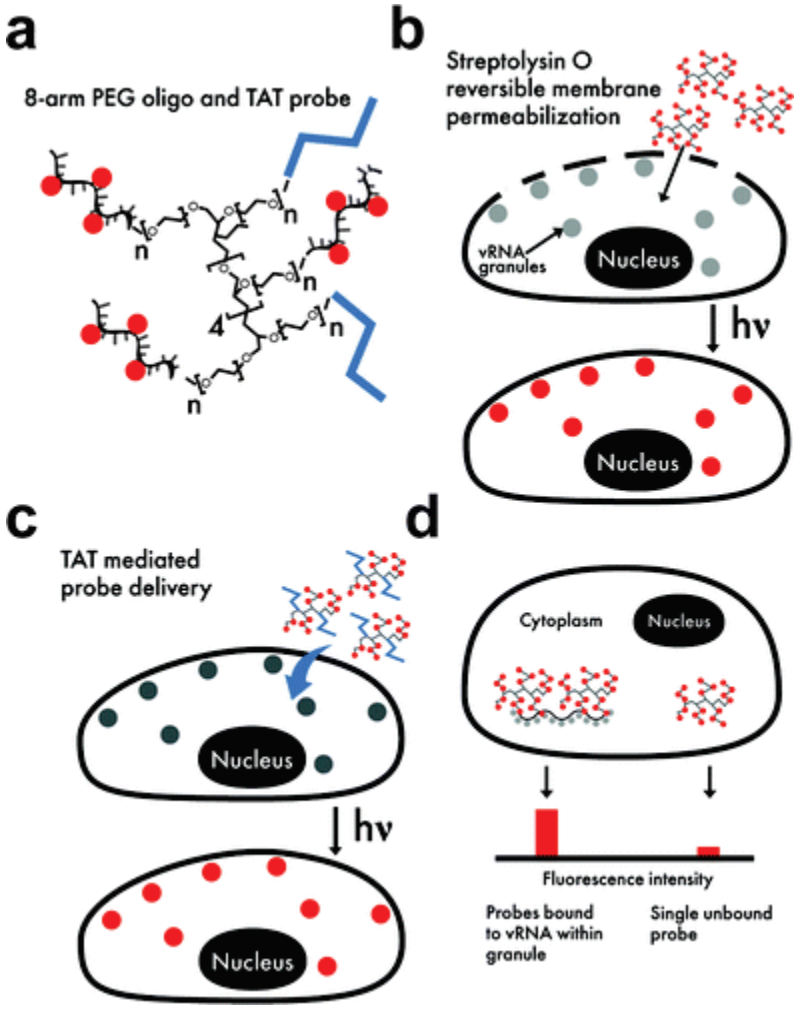

Figure 7.4: Design, delivery, and imaging of probes. (a) Schematic of the 8-arm PEG conjugated to fluorescently labeled oligonucleotides and TAT peptide (blue). (b) Cells, reversibly permeabilized with streptolysin O, allow for diffusion of probes into the cytoplasm. Probes bound to target RNA are visualized under a fluorescence microscope. (c) Transduction of TAT-PEG probe without streptolysin O permeabilization. (d) Detection of RNA is achieved through the increased signal intensity when multiple probes are bound to a single RNA.

In vitro testing

In order to test the ligands for nonspecific aggregation, the probes were labeled with Atto 488, Cy3B, or Atto 647N fluorophores and were adsorbed onto a cover glass at 1 nM concentration. Using wide-field fluorescence microscopy, the probes were visible as distinct spots on the glass without apparent aggregation (**Figure 7.5a**). Lack of aggregation was confirmed both by fluorescence intensity histograms (**Figure 7.5 b−d**) and by the lack of colocalization of probes labeled with different fluorophores. When the probes were delivered at 5 nM concentration in A549 cells either by SLO permeabilization (**Figure 7.6a**) or by TAT conjugation (**Figure 7.6b**), similar spots were visible as seen in the extended focus images. Extended focus images are a projection of all the *z*-planes into a two-dimensional image. The images were presented in this format to include all the relevant signal within the three-dimensional cell. The uniformity of the signal within the cytoplasm indicated that probe was not aggregating due to nonspecific interaction with cellular components.

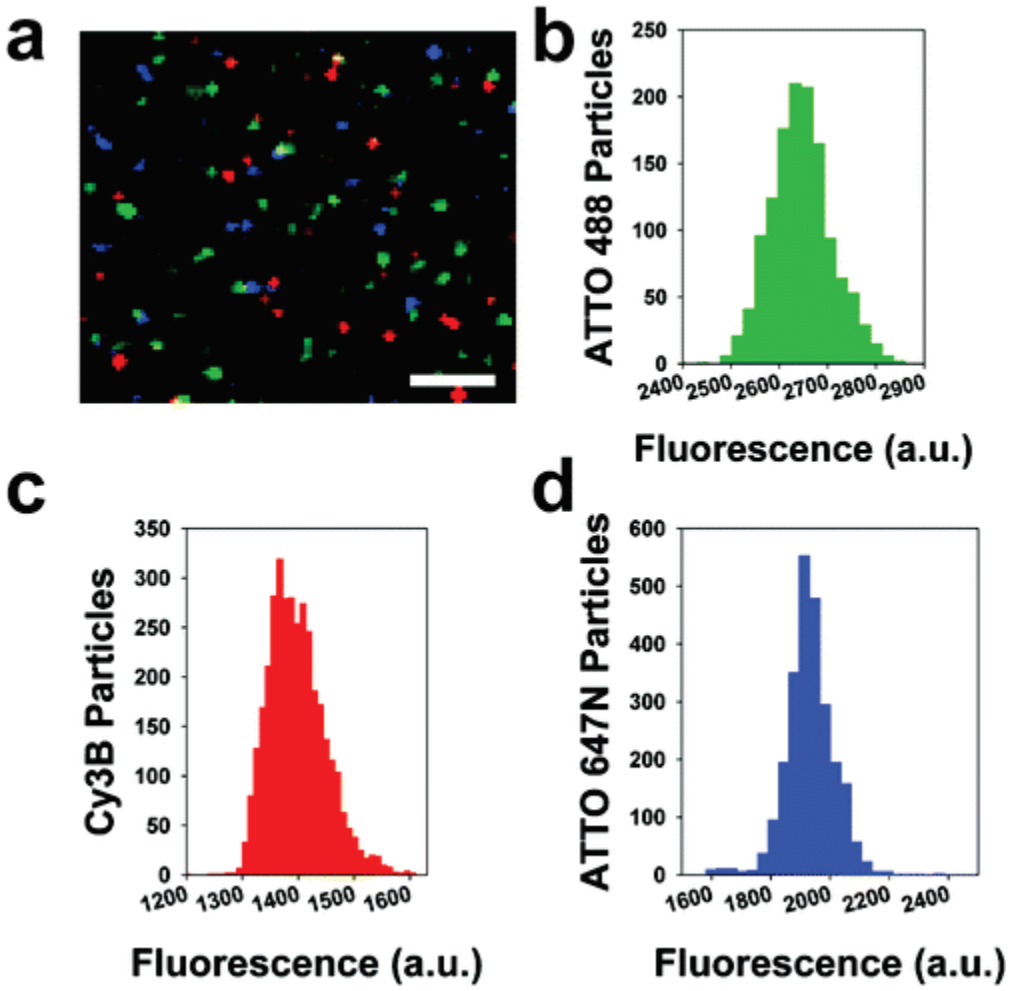

Figure 7.5: Characterization of single probes on glass. (a) Atto 488 (green), Cy3B (red), and Atto 647N (blue) labeled probes were adsorbed onto glass and analyzed for the colocalization and aggregation. Corresponding intensity histograms (b, c, and d) show a unimodal distribution consistent with single probes. Scale bar is 2 μm.

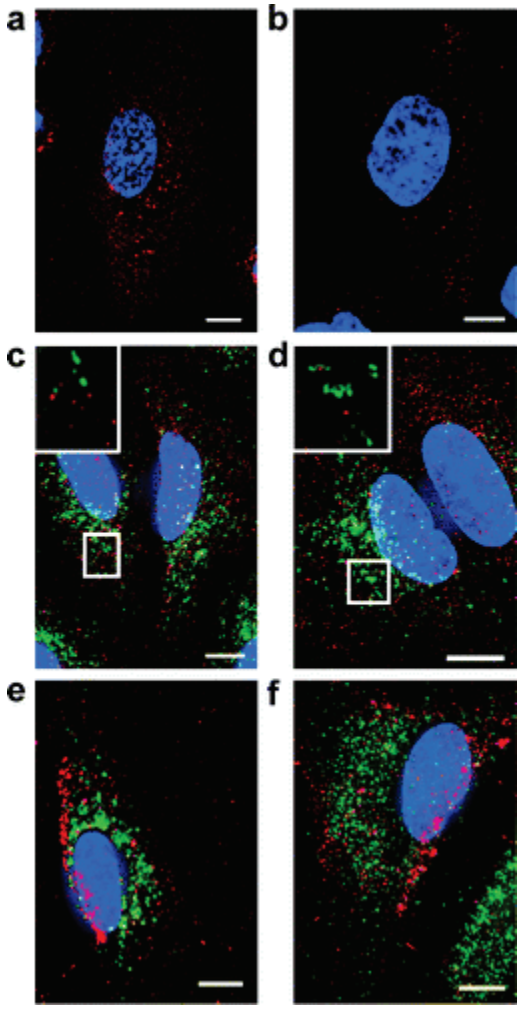

Figure 7.6: PEG probes and colocalization with endosomes. Distribution of PEG probes targeted against hRSV in A549 cells and colocalization with endosomal marker CD63 and lysosomal marker LAMP1. Extended focus of noninfected cells with probe (red) delivered (a) by SLO permeabilization and (b) by TAT conjugation. Extended focus of noninfected cells with probe (red) delivered by TAT conjugation and (c) stained for CD63 (green) and (d) LAMP1 (green). Insets in c and d show single plane from boxed region. Extended focus of hRSV infected cells with probe (red) delivered by TAT conjugation and stained for (e) CD63 (green) and (f) LAMP1 (green). Scale bars are 10 μm.

Delivery testing

Recent reports have shown that macromolecule uptake by TAT can proceed through an endocytic pathway, even if this has been suggested to be dependent upon the conjugated macromolecule (Fischer, Waizenegger et al. 2002; Ter-Avetisyan, Tunnemann et al. 2009). Nonendosomal transduction of the probes is recommended, since it reduces the exposure of the probe to nucleases and eliminates the need for endosomal releasing agents such as poly(propylacrylic acid) to be added to the delivery medium. In order to determine whether or not TAT conjugated probes entered cells through the endosomal pathway, TAT-probes were delivered at 5 nM into uninfected and hRSV infected cells that were subsequently fixed and immunostained for endosomal and lysosomal markers. Cells were immunostained for cluster of differentiation 63 (CD63) (**Figure 7.6c,e**) and lysosomal associated membrane protein 1 (LAMP1) (**Figure 7.6d,f**). Multicolor images were obtained by wide-field fluorescence microscopy and deconvolution, and revealed little colocalized signal between the TAT-conjugated probe and protein markers. In these figures, extended views were shown to illustrate the signal within the cell. Some apparent colocalization may be perceived using this presentation due to the merging of signal from different *z*-planes. Inset images from one *z*-plane were included to show the lack of colocalization qualitatively. This was confirmed quantitatively by low Manders overlap coefficients ($R < 0.1$) for the colocalization of the probe with CD63 and with LAMP1 using three-dimensional reconstructions of the images.

In cell testing

In order to demonstrate the applicability of these probes for live cell imaging, the viral genomic RNA of hRSV was imaged in A549 cells both live and after fixation and immunostaining of the hRSV N protein. The hRSV N protein has been shown to reside within inclusion bodies, to colocalize with the hRSV genome in imaging experiments, and to bind to hRSV vRNA (Murphy, Loney et al. 2003; Santangelo, Lifland et al. 2009). Co-localization with the N protein served to demonstrate the accurate targeting of the probe to the vRNA. A549 cells were infected with the A2 strain of hRSV and incubated for 24 h. Probes were then delivered at 5 nM via SLO membrane permeabilization and allowed to recover. Subsequently, cells were either fixed with 4% paraformaldehyde for immunostaining or stained with Hoechst 33342 for live cell imaging. Cells fixed and immunostained for the hRSV N protein showed vRNA localization near the plasma membrane and exhibited colocalization with hRSV N protein similar to previously reported data (**Figure 7.7a**)(Santangelo, Lifland et al. 2009). In order to quantify the degree of colocalization between the vRNA and N protein, Manders overlap coefficients were generated using voxel intensities. Overlap coefficients were generally high, typically $R > 0.8$. **Figure 7.7a** shows a representative cell with an overlap coefficient of 0.843. In addition to whole cell automatic colocalization, intensity profiles showed correlation between the hRSV genomic and N protein signal (**Figure 7.7c,d**). In the live cell images, similar localization of the vRNA was observed with vRNA predominantly residing in inclusion bodies close to the cell membrane (**Figure 7.7**e). Delivery of probe into noninfected cells served as a negative control and resulted in little to no signal when imaged under the same conditions as the infected cells (**Figure 7.7b,f**). Interestingly, probes delivered into noninfected cells demonstrated no significant nuclear background.

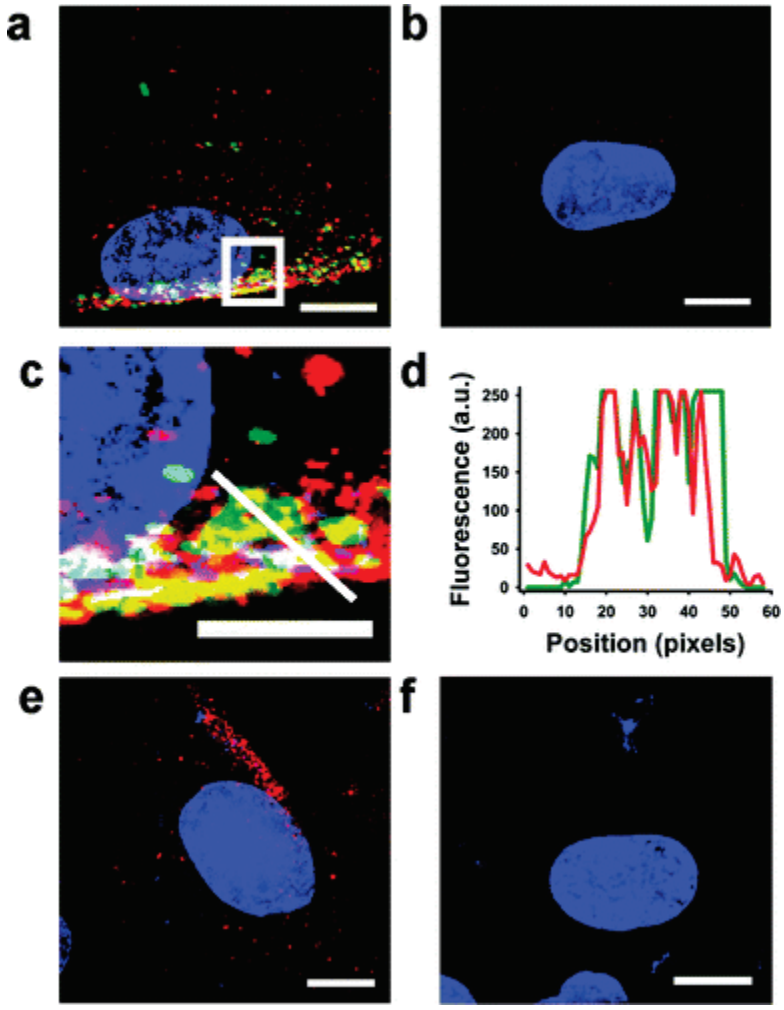

Figure 7.7 SLO-mediated delivery of PEG probes targeted against hRSV. Distribution of probes (red) into fixed hRSV (a) infected and (b) noninfected cells and staining for the viral protein N (green) and DAPI (blue). (c) Magnification of boxed region in Figure 7.7a. (d) Intensity profile along line in Figure 7.7c. Distribution of probes (red) into live hRSV (e) infected and (f) noninfected cells. Nuclei were stained using Hoechst 33342. Scale bars in a,b,e,f are 10 μm. Scale bar in c is 5 μm.

We subsequently delivered the TAT conjugated probes at 5 nM concentration into hRSV infected and noninfected A549 cells. These probes revealed a similar pattern of RNA localization as the SLO-delivered ones in infected cells both live and upon fixation. In the latter case, colocalization with the viral N protein at the plasma membrane confirmed efficient vRNA targeting (**Figure 7.8a,c,d**). In noninfected cells, TAT-conjugated probes exhibited little to no signal (**Figure 7.8 b**) and appeared to be homogeneously distributed in the cytoplasm (**Figure 7.6 b**). While the mechanism for TAT-mediated probe delivery is not yet fully understood, our data strongly suggest that it does not involve an endosomal pathway and are consistent with previous reports (Vives, Brodin et al. 1997; Ter-Avetisyan, Tunnemann et al. 2009). In particular, Vives et al. reported that fluorescently labeled TAT peptides were efficiently taken up by cells within 5 min at concentrations as low as 100nM, and the internalization process was shown not to involve an endocytic pathway. The sensitivity of the fluorescein reporter precluded measurements using TAT concentrations below 100nM (Vives, Brodin et al. 1997). In our case, uptake of probes occurred in less than 10 min at a concentration of 5 nM. Moreover, our probes showed no colocalization with endosomal and lysosomal markers, and colocalized well with the N protein, yielding a distribution similar to the one observed in SLO membrane permeabilization-based delivery. Additionally, live cell imaging experiments confirmed the results and indicated that cell fixation does not alter probe localization (**Figure 7.8 e,f**).

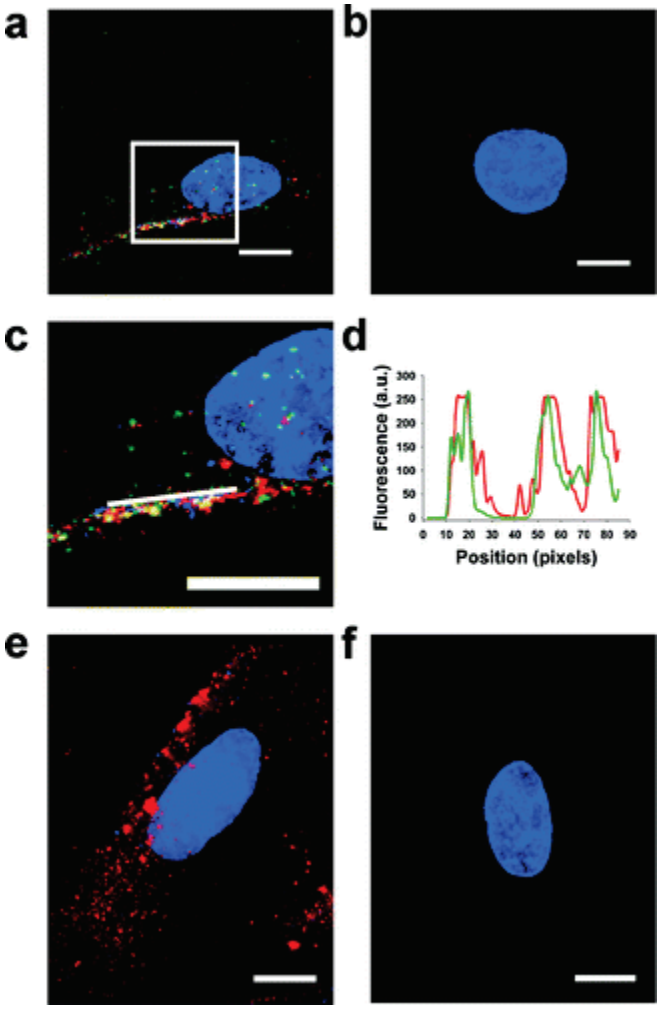

Figure 7.8: TAT-mediated delivery of PEG probes targeted against hRSV. Distribution of probes (red) into fixed hRSV (a) infected and (b) noninfected cells and staining for the viral protein N (green) and DAPI (blue). (c) Magnification of boxed region in Figure 7.8a. (d) Intensity profile along line in Figure 7.8c. Distribution of probes (red) into live hRSV (e) infected and (f) noninfected cells. Nuclei were stained using Hoechst 33342. Scale bars in a,b,e,f are 10 μm. Scale bar in c is 5 μm.

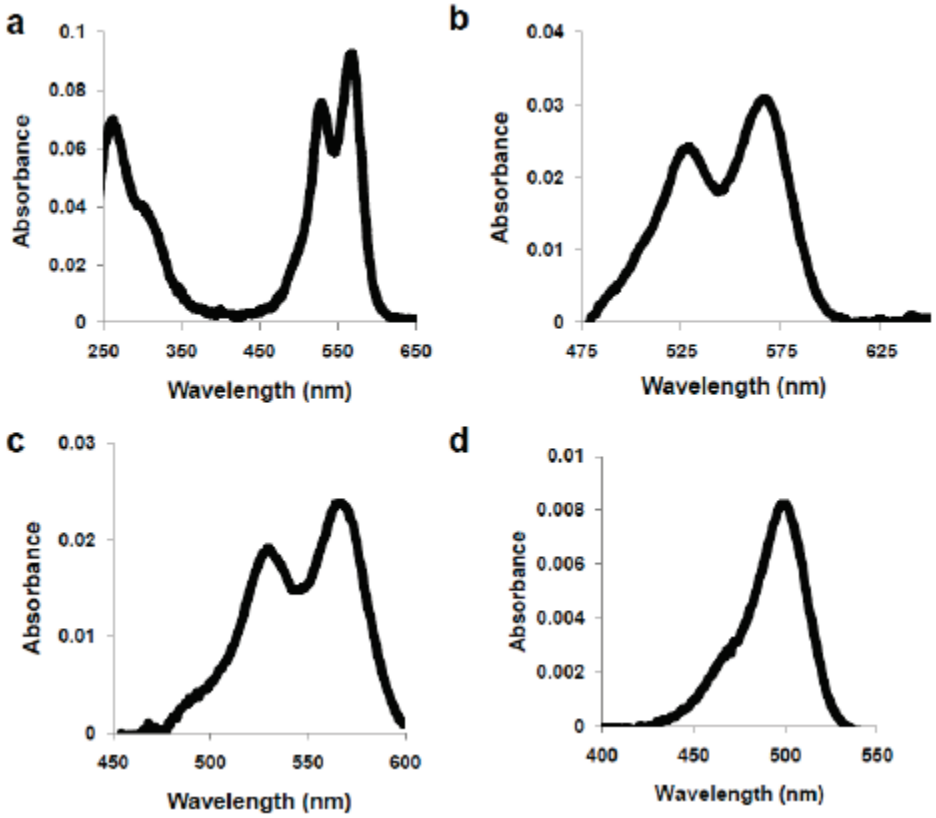

Figure 7.9: Absorbance spectra of labeled probes. (a) Cy3b-labelled oligonucleotides, (b) Cy3b-labelled oligonucleotides in the PEG probes (c) Cy3b-labelled oligonucleotides in the PEG-TAT probes and (d) unlabelled oligonucleotides in the PEG-TAT-FAM probes.

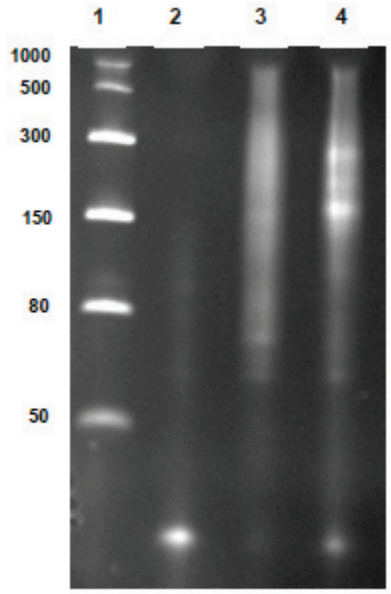

Figure 7.10: Ethidium bromide stained 15% TBE-UREA gel of the probes. (1) low range ssRNA ladder (New England Biolabs), (2) unconjugated oligonucleotides, (3) PEG probes and (4) PEG-TAT probes.

The importance of trans-acting factors, such as RNA binding proteins and noncoding RNAs, in the regulation of mRNA and viral RNAs has recently garnered increased attention (Keene 2007). These factors are responsible for the post-translational regulation of mRNAs and for the late stages of the viral life cycle such as replication and packaging of viral genomic RNA (Emara and Brinton 2007). The RNA molecule, along with trans-acting factors, ultimately determines the function of the RNA. In vitro methods for studying these ribonucleoprotein complexes (RNPs) give only an averaged view of the function of these complexes. However, within the cellular context, these RNPs are often heterogeneous, and as such, methods are needed that enable the study of the spatial and temporal dynamics of RNA and interaction with RNA binding proteins within the cell (Martin and Ephrussi 2009). These methods must be sensitive because of the low concentration of specific RNAs inside the cell, and must be able to provide accurate subcellular localization of RNA.

Conclusion

Using an eight-arm activated PEG core as a multifunctional platform, we have developed a single molecule sensitive RNA imaging probe. Fluorescently labeled oligonucleotides bound to the PEG core were delivered into live cells using two delivery methods, reversible membrane permeabilization and TAT-mediated transduction. Individual probes were visible both on glass and inside the cells using widefield fluorescence microscopy. TAT-mediated delivery did not result in accumulation of probes in endosomes, nor did it result in the nonspecific aggregation of probes inside the cell. To demonstrate the accurate targeting of RNA in the cell, probes targeted against RSV vRNA were delivered into infected cells and demonstrated subcellular localization

at the plasma membrane, colocalization with known vRNA binding proteins, and signal substantially higher than in mock infected controls. Signal was observed in less than 10 min regardless of the delivery method and in the presence of probe concentrations of 5 nM. The rapid binding of the probes to their target is an essential feature for the study of RNA dynamics, because it allows for the observation of phenomena that occur on short time scales. In addition to this, the low concentration of the probes contributes to reduce nonspecific binding. Our results suggest that TAT (or other CPPs) conjugated PEG probes may allow for the imaging of specific RNAs in vivo when combined with fluorophores that absorb in the near-infrared wavelengths (Mahmood, Tung et al. 1999).

References

Anderson, P. and N. Kedersha (2009). "RNA granules: post-transcriptional and epigenetic modulators of gene expression." Nat Rev Mol Cell Biol **10**(6): 430-436.

Beckham, C. J. and R. Parker (2008). "P bodies, stress granules, and viral life cycles." Cell Host Microbe **3**(4): 206-212.

Emara, M. M. and M. A. Brinton (2007). "Interaction of TIA-1/TIAR with West Nile and dengue virus products in infected cells interferes with stress granule formation and processing body assembly." Proc Natl Acad Sci U S A **104**(21): 9041-9046.

Fischer, R., T. Waizenegger, et al. (2002). "A quantitative validation of fluorophore-labelled cell-permeable peptide conjugates: fluorophore and cargo dependence of import." Biochim Biophys Acta **1564**(2): 365-374.

Fusco, D., N. Accornero, et al. (2003). "Single mRNA molecules demonstrate probabilistic movement in living mammalian cells." Curr Biol **13**(2): 161-167.

Healy, J. M., S. D. Lewis, et al. (2004). "Pharmacokinetics and biodistribution of novel aptamer compositions." Pharm Res **21**(12): 2234-2246.

Keene, J. D. (2007). "RNA regulons: coordination of post-transcriptional events." Nat Rev Genet **8**(7): 533-543.

Mahmood, U., C. H. Tung, et al. (1999). "Near-infrared optical imaging of protease activity for tumor detection." Radiology **213**(3): 866-870.

Majlessi, M., N. C. Nelson, et al. (1998). "Advantages of 2'-O-methyl oligoribonucleotide probes for detecting RNA targets." Nucleic Acids Res **26**(9): 2224-2229.

Martin, K. C. and A. Ephrussi (2009). "mRNA localization: gene expression in the spatial dimension." Cell **136**(4): 719-730.

Molenaar, C., S. A. Marras, et al. (2001). "Linear 2' O-Methyl RNA probes for the visualization of RNA in living cells." Nucleic Acids Res **29**(17): E89-89.

Murphy, L. B., C. Loney, et al. (2003). "Investigations into the amino-terminal domain of the respiratory syncytial virus nucleocapsid protein reveal elements important for nucleocapsid formation and interaction with the phosphoprotein." Virology **307**(1): 143-153.

Nitin, N., P. J. Santangelo, et al. (2004). "Peptide-linked molecular beacons for efficient delivery and rapid mRNA detection in living cells." Nucleic Acids Res **32**(6): e58.

Player, M. R., D. L. Barnard, et al. (1998). "Potent inhibition of respiratory syncytial virus replication using a 2-5A-antisense chimera targeted to signals within the virus genomic RNA." Proc Natl Acad Sci U S A **95**(15): 8874-8879.

Rapozzi, V., S. Cogoi, et al. (2002). "Antigene effect in K562 cells of a PEG-conjugated triplex-forming oligonucleotide targeted to the bcr/abl oncogene." Biochemistry **41**(2): 502-510.

Rinne, J., B. Albarran, et al. (2007). "Internalization of novel non-viral vector TAT-streptavidin into human cells." BMC Biotechnol **7**: 1.

Santangelo, P., N. Nitin, et al. (2006). "Live-cell characterization and analysis of a clinical isolate of bovine respiratory syncytial virus, using molecular beacons." J Virol **80**(2): 682-688.

Santangelo, P. J. and G. Bao (2007). "Dynamics of filamentous viral RNPs prior to egress." Nucleic Acids Res **35**(11): 3602-3611.
Santangelo, P. J., A. W. Lifland, et al. (2009). "Single molecule-sensitive probes for imaging RNA in live cells." Nat Methods **6**(5): 347-349.
Sproat, B. S., A. I. Lamond, et al. (1989). "Highly efficient chemical synthesis of 2'-O-methyloligoribonucleotides and tetrabiotinylated derivatives; novel probes that are resistant to degradation by RNA or DNA specific nucleases." Nucleic Acids Res **17**(9): 3373-3386.
Suzuki, T., N. Kanbara, et al. (1984). "Physicochemical and biological properties of poly(ethylene glycol)-coupled immunoglobulin G." Biochim Biophys Acta **788**(2): 248-255.
Ter-Avetisyan, G., G. Tunnemann, et al. (2009). "Cell entry of arginine-rich peptides is independent of endocytosis." J Biol Chem **284**(6): 3370-3378.
Tunnemann, G., G. Ter-Avetisyan, et al. (2008). "Live-cell analysis of cell penetration ability and toxicity of oligo-arginines." J Pept Sci **14**(4): 469-476.
Vargas, D. Y., A. Raj, et al. (2005). "Mechanism of mRNA transport in the nucleus." Proc Natl Acad Sci U S A **102**(47): 17008-17013.
Vives, E., P. Brodin, et al. (1997). "A truncated HIV-1 Tat protein basic domain rapidly translocates through the plasma membrane and accumulates in the cell nucleus." J Biol Chem **272**(25): 16010-16017.

CHAPTER 8

FUTURE DIRECTIONS

Introduction

To date MTRIPs have proven useful in localizing native RNAs and viral genomic RNA in both fixed and live cells. For both β-actin mRNA and viral genomic RNA of hRSV there is substantial evidence that the signal from MTRIPs represents an accurate protein of the RNA present. There is however, room for improvement in several aspects of the method including probe design and data analysis.

Probe design

The most pressing challenge in probe design is the design of targeting sequence for the MTRIP ligands. These sequences must be unique to the RNA of interest, contain an acceptable (five or more) number of thymidines, must not block RNA binding proteins, and must be accessible to binding (without local secondary structure). While many of these problems can be solved prior to synthesis and testing of the ligands, probe sequence design remains an art and some probe ligands fail to bind. Better structural information may help in this aspect, however, an *in vitro* method of determining binding of a panel of cheaper (possibly DNA based) ligands would prove to be very useful. A method combining cycles of binding and ligand amplification similar to SELEX or affinity purification of RNAs of interest are possible methods to satisfy this challenge.

While linear oligonucleotide probes and molecular beacons of different chemistries have been tested, to date there has been no systematic study of the effect of

nucleic acid chemistry has on imaging data. Higher affinity probe have been shown to bind with faster kinetics than lower affinity ligand; however, no design rules are in place to describe the number and type of modified bases needed. In the example above, while DNA is not ideal for labeling RNAs in live cells, it could be used as to test the relative fitness of different sequences for using in imaging experiments. The main rational for obtaining this structure function relationship is that oligonucleotides with fewer modified bases can be purchased substantially cheaper than the current MTRIP probes (~$700 for 50 pmol of MTRIP ligands vs. $10 for ligands of DNA). This is almost insignificant for a single target; however, in order to test and use MTRIPs against multiple RNA targets, or indeed an entire transcriptome, a substantial reduction in the cost to test ligands is needed.

Additional targets

Another area where these probes may be useful is in the study of other viral targets such as the genomic RNA of positive sense RNA viruses and the cRNA of both positive and negative sense viruses. Several challenges may arise such as lower copy number of cRNA and the lack of encapsidation of positive sense RNA viruses. As for cellular targets, further research into the colocalization and co-transport of RNAs encoding proteins that function together could shed light on the RNA operon hypothesis.

In vivo RNA imaging

While the ability to target and image RNAs in live cell in vitro may prove useful in studying the pathogenesis of viruses and deregulation of host RNAs, the ability to image RNAs in vivo may be useful both from a diagnostic standpoint and for therapeutics. By

imaging RNAs in vivo, we may be able to follow the initial infection of a viral inoculum, if preloaded with an RNA imaging probe, we may be able to detect where a viral infection occurs, for example a respiratory viral infection in the upper or lower airways, and follow the spatial localization of the infection in real time, and finally we may be able to use these probes to specifically deliver therapeutics to the site of infection. Using the PEG probe alternative core design and either radio-labeled ligands or infrared fluorescent dyes and peptide mediated delivery, these probe may be extended for use *in vivo*.

Improvements in analysis

In addition to the changes in the overall methodologies of tagging RNA, improvements can be made in the area of data analysis. Using a more sensitive and higher frame rate image capture device it may be possible to probe phenomena not seen with a standard CCD camera. For instance at frame rates above 10 Hz, it may be possible to probe unhindered diffusion even of relatively large super-macromolecular structures such as RNPs. Using higher frame rates it may also be possible to further bifurcate active and passive trajectories using the asymmetry parameter and joint probability histograms to more accurately isolate transport phenomena occurring in each mode of transport, or even identify additional modes of transport and subsets of each, such as the cooperation of multiple motors. Along with improvements in image acquisition come the ability to use automated methods of particle tracking.

Functional analysis of RNA granules

Finally, in order to decipher the function of the RNA granules imaged, a better method of ascertaining the function of each granule must be developed. For example, a method that can determine the RNA binding proteins associated with each RNA could be used to determine whether a particular RNA was undergoing translation, silencing, destruction or, in the case of viral RNA, transcription. One such method using a proximity ligation assay and rolling circle amplification is already under development. Other methods using immunostaining and subdiffraction limit imaging may also prove useful.

VITA

AARON WILLIAM LIFLAND

Aaron Lifland was born and raised in Sharon Massachusetts where he attended public schools and graduated from Sharon High School. He received a B.S.E. in Engineering from The Cooper Union for the Advancement of Science and art in New York City, NY, where he worked for Melissa Micou in the Maurice Kanbar Center for Biomedical Engineering. He worked as a research student at the Cleveland Clinic under an NIH REU fellowship and as a research student in the lab of Vladimir Brezina at Mount Sinai School of Medicine before coming to the Georgia Institute of Technology and Emory University to pursue a doctorate in biomedical engineering.